The effect of ionization of spray on the wetting characteristics of an adiabatically cooled heat exchanger

by

Bernard De Waal Esterhuyse

Thesis presented in partial fulfillment of the requirements for the degree of Master of Mechanical Engineering at the University of Stellenbosch

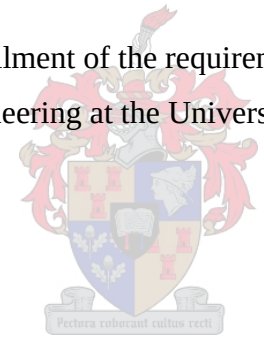

Thesis supervisor: Prof. D.G. Kröger

September 2004

Declaration

I, the undersigned, hereby declare that the work in this thesis is my own original work and has not previously in its entirety or in part been submitted at any university for a degree.

.....

B.D. Esterhuyse

1 September 2004

Abstract

An investigation was made into the use of pre-cooling of air with evaporative cooling as a means of improving the performance of air-cooled heat exchangers (finned tube) under conditions of ambient temperatures above maximum design values and during times of increased load. A review of previous research on this subject indicated that the concept is theoretically sound, but that practical application thereof is still limited. It was found that one of the major areas of concern is the wetting of the heat exchanger finned surface and subsequent corrosion.

Mathematical models were derived for the behavior of liquid droplets in free air stream conditions and droplets that have penetrated a laminar hydrodynamic boundary layer formed on a flat plate. These two models were combined to determine the behavior of a liquid droplet for its entire lifetime. It was found that evaporation of droplets in a boundary layer resulted in major improvements in heat transfer. In an attempt to prevent droplets from impacting and wetting the finned tube heat exchanger, the use of electrostatically charged water spray was investigated. Experiments were performed to determine the charging performance of a capacitive electrostatic nozzle. It was found that this type of nozzle successfully charged droplets in a spray. Experiments were then performed whereby electrostatic spray was sprayed on to a heat exchanger with a similar electric charge as the droplets. It was found that droplet deposition decreased significantly as the charge on the droplets was increased. However, total prevention of deposition could not be achieved, since the equipment used could not produce high enough voltages. This concept shows some promise, and it is recommended that further research be performed on it. At this stage, no reliable method of evaporative precooling of air has yet been found. The only viable option for cooling capacity shortages at present is the construction of large air-cooled heat exchangers or the addition of wet cooling towers.

Key words: Air-cooled heat exchangers, droplet evaporation, evaporative cooling, air pre-cooling, electrostatic spray.

Opsomming

Voorverkoeling van lug deur middel van verdampingsverkoeling vir die gebruik met droë lug-verkoelde vinbuis warmteruilers is ondersoek as ‘n manier om die verkoelingseffektiwiteit te verhoog gedurende tye van hoë omgewingstemperature en verhoogde las. ‘n Ondersoek van navorsing op die gebied het getoon dat die konsep in teorie moontlik is, maar dat daar nog geen praktiese implementering plaasgevind het nie. Dit blyk dat die benatting en korrosie van die vinbuise een van die hoof probleme is.

Wiskundige modelle is afgelei vir die gedrag van ‘n water druppel in ‘n vrye lug stroom en vir ‘n druppel in ‘n laminêre hidrodinamiese grenslaag op ‘n plat plaat. Die twee modelle is gekombineer om die gedrag van ‘n druppel gedurende sy totale leeftyd te bepaal. Die model het getoon dat verdamping van ‘n druppel in die grenslaag ‘n drastiese verhoging in die hitteoordrag koëffisiënt veroorsaak. Die gebruik van elektrostaties gelaaide sproei om te verseker dat die vinbuis warmteruiler droog bly is ondersoek. Eksperimente is uitgevoer om die elektriese laaivermoëns van ‘n kapasitiewe elektrostatiese mondstuk te bepaal. Daar is gevind dat die tipe mondstuk suksesvol is in die laai van druppels. Toetse is toe uitgevoer waartydens gelaaide druppels gespuit is op ‘n warmteruiler met dieselfde lading as die druppels. Daar is gevind dat die duppel neerslag op die warmteruiler merkwaardig afneem namate die lading op die druppels verhoog is. Die warmteruiler kon egter nie totaal droog gehou word nie, aangesien die toerusting gebruik vir die toetse nie ‘n hoë genoeg spanning kon gee nie. Hierdie konsep is belowend, en dit word aanbeveel dat verdere navorsing daarop gedoen word. Op hierdie stadium is daar nog geen betroubare metode gevind om die verkoelings effektiwiteit van lugverkoelde warmteruilers met verdampings verkoeling te bewerkstellig nie. Die enigste sinvolle opsie tans is die kostruksie van groter lugverkoelde warmteruilers of die konstruksie van nat koeltorings.

Sleutelwoorde: Lugverkoelde warmteruilers, druppelverdamping, verdampingsverkoeling, elektrostatiese sproei.

Acknowledgements

I would like to express my sincere gratitude to the following persons and institutions for their support and contributions towards the completion of this study:

Prof. D.G. Kröger for the privilege of working with him and his patience, humor and insight. The wisdom he shared extended beyond engineering to life itself.

Mr. Cobus Zietsman for all his advice and friendship.

SMD at Stellenbosch, whose quality work made this project possible.

The staff of the Engineering Library for finding obscure articles and for patience with books returned late.

Ms. SG van der Merwe, for all her patience and encouragement through the hard times.

Table of contents

Nomenclature

Symbols

a	area	$[m^2]$
b	width	[m]
B	magnetic field	$[Wb \cdot m^{-2}]$
B_M	mass transfer number	
B_T	thermal transfer number	
c	concentration	$[kg \cdot m^3]$
c_p	specific heat at constant pressure	$[J \cdot kg^{-1} \cdot K^{-1}]$
CMR	charge-to-mass ratio	
C	capacitance	[F]
d	diameter	[m]
D	binary vapor diffusivity	$[m^2 \cdot s^{-1}]$
DDPS	droplet deposition density per unit time	$[\mu g \cdot cm^{-2} \cdot s^{-1}]$
E	electric field	$[V \cdot m^{-1}]$
F	force	[N]
g	acceleration due to gravity	$[m \cdot s^{-2}]$
h	heat transfer coefficient	$[W \cdot m^{-2} \cdot K^{-1}]$
h_{fg}	latent heat of vaporization	$[J \cdot kg^{-1} \cdot K^{-1}]$
k	thermal conductivity	$[W \cdot m^{-1} \cdot K^{-1}]$
K	parameter defined by equation (5.25), vortex strength	$[m^2 \cdot s^{-1}]$
l	length	[m]
M	molecular weight	
$\overline{M}$	average molecular weight of boundary layer	
m	mass	[kg]
$\dot{m}$	mass flow rate	$[kg \cdot s^{-1}]$
$\dot{m}''$	mass flux	$[kg \cdot s^{-1} \cdot m^{-2}]$
N	mole number	
p	pressure, penetration	$[N \cdot m^{-2}]$, [m]
pr	pressure ratio	

P	power	[W]
q	charge	[C]
q_t	transverse velocity	[$m \cdot s^{-1}$]
$\dot{q}$	heat transfer rate	[W]
$\dot{q}''$	heat flux	[$W \cdot m^{-2}$]
R	resistance	[$K \cdot W^{-1}$]
R^2	coefficient of determination	
r	radius	[m]
s	spacing between flat surfaces	[m]
T	temperature	[K]
t	time	[s]
u	x-direction velocity	[$m \cdot s^{-1}$]
v	y-direction velocity	[$m \cdot s^{-1}$]
V	voltage	[V]
W	work	[W]
x	distance coordinate	[m]
y	distance coordinate	[m]
z	distance coordinate	[m]
Y	mass fraction	

Greek symbols

Δ	differential	
α	parameter defined by equation (5.9)	[$m^2 \cdot s^{-1}$]
β	parameter defined by equation (5.10)	[$m \cdot s^2$]
δ	boundary layer thickness	[m]
γ	specific ratio	
λ	parameter defined by equation (5.5), evaporation constant	[$m^2 \cdot s^{-1}$]
μ	dynamic viscosity	[$kg \cdot m^{-1} \cdot s^{-1}$]
ν	kinematic viscosity	[$m^2 \cdot s^{-1}$]
θ	angle	[deg]
ρ	density	[$kg \cdot m^{-3}$]
σ	surface tension	[$N \cdot m^{-1}$]
ω	humidity ratio	[kg H_2O·kg dry air^{-1}]

ξ	point of entry of the droplet in the boundary layer	[m]

Subscripts

a	dry air, air side, air gap
ap	applied pulsed
av	average
bl	boundary layer
c	compressor
d	drop
db	dry bulb
e	evaporation
f	fluid, final
he	heat exchanger
i	initial, interface
ir	induction ring
l	liquid
max	maximum
R	relative, resultant
s	surface
st	steady state
t	transverse, insulating layer
V	vertical
w	water
wb	wet-bulb
0	initial, surface
∞	free stream conditions

Dimensionless groups

Nu	Nusselt number
Pr	Prandtl number
Re	Reynolds number
We	Weber number

List of figures

List of tables

1 Introduction

This chapter gives an overview of the main issues of the project as well as the scope of the thesis.

1.1 Overview

In recent times much research has been focused on the improvement of performance of air-cooled heat exchangers as well as gas turbines with the use of evaporative cooling. Employing evaporative cooling to cool the inlet air of an air-cooled heat exchanger will result in a higher heat exchange rate, while using evaporative cooling to cool the inlet gas of a gas turbine, will result in higher gas densities, which in turn will result in increased power output.

Cooling air by means of evaporation remains one of the least expensive techniques to reduce dry-bulb temperatures. The principle of the process indicates that evaporative cooling can only remove sensible heat, thus, the evaporative cooling system works best in hot and dry climates where maximum evaporation will result.

Evaporative cooling is based on the principle that when air travels past a wet surface, water evaporates into the air. The latent heat required for this process is extracted from the air and the water, causing both the air and water temperatures to drop. The advantages of evaporative cooling lies in the relatively high amount of energy required to convert water from the liquid form into its gaseous form. While the energy required to raise the temperature of water by 1 ^{o}C is only 4.18 kJ/kg, the specific latent heat of vaporization is 2257 kJ/kg.

Air-cooled heat exchangers (ACHE) are used extensively in modern industry. Their sizes vary greatly, from heat sinks for electronic equipment to massive forced draft and induced draft heat exchangers used at power stations. Air-cooled heat exchangers play a major role in the chemical and energy industries. Modern design and analysis

of these installations focus on the continuous improvement of efficiency and a greater awareness of the environmental impacts of such systems.

From an environmental perspective ACHE systems have the advantage of using less water than similar heat exchangers using wet cooling. Because of this ACHE systems are well suited for the use in industrial facilities situated in dry regions with limited water supply. The fact that these systems use less water, however, causes them to become inefficient during times of high ambient temperatures. Data on seasonal temperature fluctuations are available for most regions, but because of the high capital investment required for such a system, the ACHE will be designed for statistically averaged yearly temperatures and not for maximum temperatures. When the ACHE operates at maximum load during times of ambient temperatures higher than design values, the cooling capacity is reduced, which in turn leads to decreased production of the associated facility.

Another factor to consider is economic pressure that could lead to attempts to increase plant production that in turn could lead to increased load on the ACHE system. This could lead to a situation where the ACHE system is constantly operated at loads above design conditions resulting in inadequate cooling and possible losses in production.

Perlman (1996) reports that in 1990 thermoelectric power generation consumed 39% (~886,47 Mℓ/day) of the total water consumption in the United States. In contrast to most user applications, water consumption by the thermoelectric industry grew by 5 % from 1985 levels. The demand for dry-cooling would become great after the year 2000, when water shortages were predicted for some states (Surface, 1977). In South Africa, three major drainage areas have been identified as regions where 95% of power generation would be situated (Woest, 1991). It is predicted that by the year 2010, water demand would be 180% of the utilizable run-off. Even if allowance were made for possible re-use and groundwater development, the demand would still exceed the supply by 17%.

1.2 Scope of the thesis

This research focuses on expanding previous theoretical droplet evaporation models and investigating the use of an electrostatically charged inlet spray as a method of reducing the sensitivity of an existing ACHE systems to ambient air temperatures above design values, as well as improving the performance of such a system during times of increased load.

The following goals were identified as guidelines for the project:

1. Review of previous research for information on possible applications of atomized water injection as a pre-cooling method for performance improvement, particularly with regards to air-cooled heat exchangers and gas turbines.
2. Review of previous research for information on methods of achieving the atomization required for evaporative pre-cooling of air.
3. A simplified analysis of heat, mass and momentum transfer of small water droplets in free stream air to establish droplet evaporation times under varying ambient conditions.
4. A simplified analysis of heat, mass and momentum transfer of small water droplets in a laminar boundary layer on a flat plate to determine the behavior of water droplets when very near to the heat exchanger surface.
5. Experimental work to establish a method of achieving the desired cooling cheaply, subject to the constraints mentioned in previous research - chiefly the prevention of droplets impacting the heat exchanger surface and causing corrosion and fouling. Following a thorough review of the literature on evaporative cooling techniques, it was decided to attempt to make use of electrostatically charged droplets sprayed at an electrically charged heat exchanger. The principle of the repulsion of similar charge is used to prevent droplets from impacting the heat exchanger surface.

2 Literature study

This chapter contains an overview of previous work on the improvement of performance of gas turbines as well as air-cooled heat exchangers with the use of inlet air-cooling. Limitations of previous work are discussed, and possible areas of refinement and expansion are identified.

2.1 Gas turbine performance improvement

Improving the efficiency of a gas turbine cycle will reduce the fuel cost to operate the turbine. Inlet air cooling and cooling of the compressor discharge boosts both efficiency and power of gas turbine cycles.

Inlet cooling reduces the workload of the compressors. The work done by the compressors can be approximated by

$$W_c = T_{ai} c_{p(av)} \left[(pr)^{\frac{\gamma_c - 1}{\gamma_c}} - 1 \right] \tag{2.1}$$

It is clear from equation (2.1) that compressor work is a function of inlet air temperature. As the inlet air temperature decreases, the compressor work decreases, and subsequently the cycle efficiency increases.

2.1.1 Review of literature

Evaporative inlet air cooling is done by injecting water into the inlet air stream of the air compressor, as shown at 1 in figure 2.1. De Lucia et al. (1995) showed that, depending on the weather, evaporative inlet cooling could enhance the power produced by a turbine by 2 – 4% per year. They concluded that evaporative inlet cooling is simple and economic, but suitable only for dry, hot climates. Bassily (1990) made use of indirect evaporative inlet cooling and showed that it could improve the efficiency of the intercooled reheat regenerative cycle by 3%, which is 1% higher that with regular evaporative inlet cooling. Bassily also showed that evaporative cooling

of the inlet air could boost efficiency of the cycle by up to 3.2%. The benefits of inlet air cooling and intercooling has been discussed extensively by other authors (Hufford, 1992; Giourof, 1995).

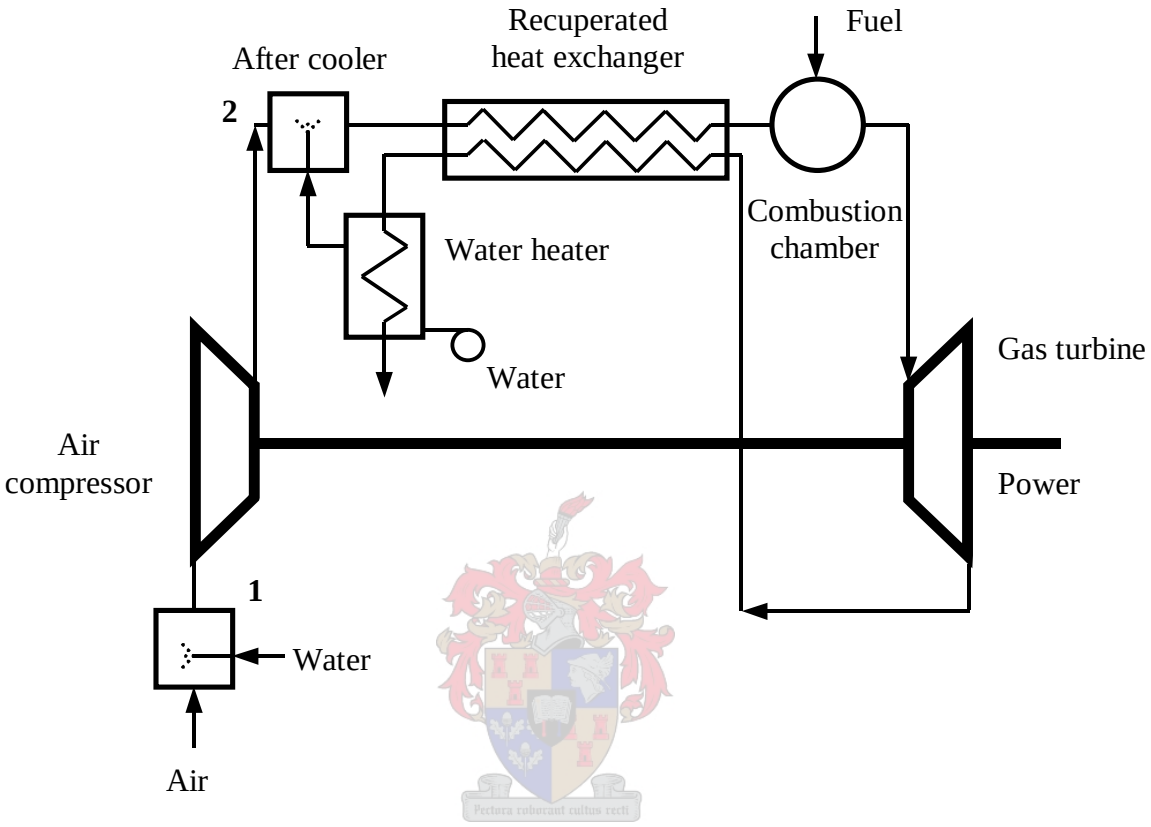

Figure 2.1 A schematic diagram of the recuperated cycle with evaporative inlet and after cooling

Evaporative aftercooling is the injection of water at the inlet of the recuperated heat exchanger, as shown at 2 in figure 2.1. The injected water is converted to steam and absorbed into the air stream. The energy gained by the injected water reduces the temperature of the air-water mixture. This increases the recovered heat, the capacity of the recuperated heat exchanger, and the cycle efficiency. The injected water also increases the mass flow rate through the gas turbine and so increases the system power output. Therefore, evaporative aftercooling is expected to increase both efficiency and power of gas turbine cycles. Gasparovic and Stapersma (1973) showed that aftercooling by water injection could increase the efficiency of the recuperated gas turbine cycle slightly and could increase its power by up to 55%. Najjar and

Zaamout (1996) reported an increase in the efficiency of the recuperated gas turbine cycle by about 13% with the use of evaporative aftercooling. Bassily (2001) showed that water injection at the compressor outlet (evaporative aftercooling) could increase the power by up to 110% as shown in figure 2.2. He also showed that efficiency could be increased by up to 16%.

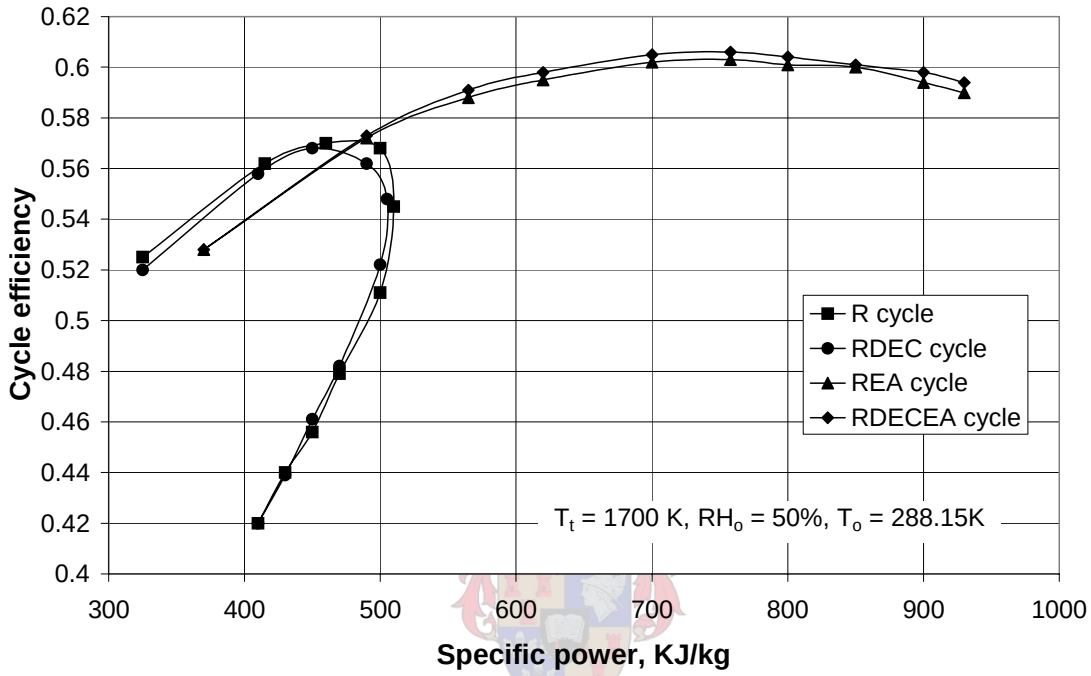

Figure 2.2 Characteristic curves of four gas turbine cycles

with R = the recuperated cycle

RDEC = the recuperated cycle with evaporative cooling of the inlet air

REA = the recuperated cycle with evaporative after cooling

RDECEA = the recuperated cycle with evaporative cooling of the inlet air and evaporative after cooling

The abovementioned research clearly indicates that finding methods of achieving effective evaporative cooling could be of major benefit to gas turbine applications.

2.2 Air-cooled heat exchanger performance improvement

In recent times much research has been focussed on the improvement of performance of air-cooled heat exchangers. A variety of methods have been proposed to improve the performance of an air-cooled heat exchanger. The concepts that have been believed to show most promise are those that make use of adiabatic cooling to cool the inlet air upstream of the heat exchanger. Oplatka (1981) proposed a theory of cooling only the air passing over the coolest part of the heat exchanger. He performed an economic analysis by comparing the cost of precooling to the cost of the production lost, such as loss of power generation capacity for power plants, during times of ambient temperatures higher than design values. This loss was presented graphically as in figure 2.3.

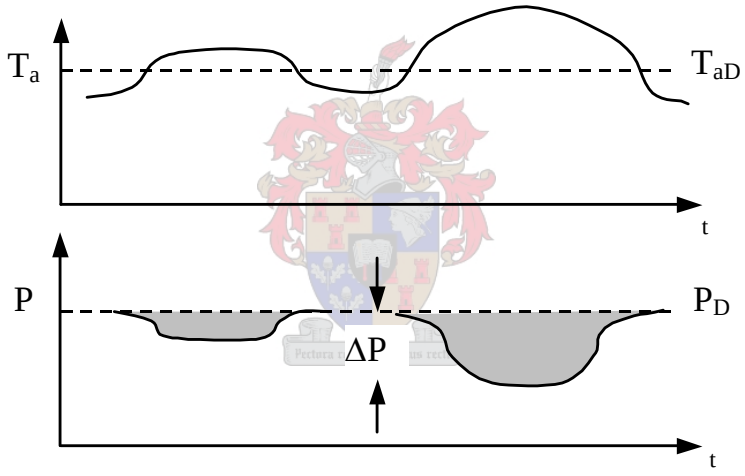

Figure 2.3 Output loss during high ambient temperatures

The shaded area represents the power lost and:

t - time
T_a - air drybulb temperature
T_{aD} - design air drybulb temperature
P - power output
P_D - design power output
ΔP - difference between design and actual power output ($P_D - P$)

While the ambient temperature, $T_{a,}$ is below the design drybulb temperature, T_{aD}, the design power output, P_D, can be achieved. When the ambient temperature rises above the design temperature, the power output drops by ΔP. The total resulting loss can then be calculated by integrating over the total time period

$$P' = \int_0^t (P_D - P) \cdot dt \tag{2.2}$$

Oplatka found that for his particular test case the cost of installation and operation of the cooling system was 50% of the financial impact of the production loss during times of high ambient temperatures. Oplatka remarked that these advantages should encourage the adoption of the proposed method in practice at the earliest opportunity.

Much research has been performed to investigate the performance improvement mentioned by Oplatka by means of evaporative cooling of the inlet air. This has mainly been achieved by either forcing the inlet air over wetted media evaporative pads or with the injection of water droplets into the inlet air stream.

When wetted media evaporative pads are used for cooling, ambient (unsaturated) air is blown across a wetted surface. Energy is extracted from the air for the evaporation process causing the drybulb temperature of the air to drop and its humidity to increase. This concept is used extensively in the air-conditioning industry to provide energy efficient cooling (Mathur, 1991; Esterhuyse, 2002). However, this concept requires relatively clean water and air, which in many cases makes it unpractical for the use in industrial environments. This method is also only effective when the air is dry and the aim is saturation of the air. It is not possible to reach super-saturation using this method. Additional concerns regarding the use of these systems are the high pressure drop through the system and the difficulty of installing these systems in existing cooling installations.

The second method entails the introduction of water droplets into the air stream upstream of the heat exchanger. The droplets are carried with the air stream, creating a two-phase fluid. Energy transferred from the air to the droplets by means of

convection causes a phase change as the droplets evaporate. This extraction of energy from the air causes the drybulb temperature of the air to drop.

The focus of this study will be the second alternative, namely atomized water injection. The history and development of the concept is presented in the next section.

2.2.1 Review of literature

The idea of improving the performance of an air-cooled heat exchanger by injection of liquid droplets into the gas stream and obtaining a liquid film, which displaces the gas boundary layer from the solid surface, was first suggested by Elperin (1961). This type of spray cooling, whereby the heat exchanger surface is wetted, can be termed deluge cooling. Favorable results by Elperin (1961) lead to other research on single cylinders and finned tubes (Nakayama et al., 1988; Lee et al., 1994). The general trend of all the results was a marked increase in overall heat transfer.

Wet surface cooling

Deluge cooling on radiator cores was tested by Yang and Clark (1975). They made use of plain-, louvered- and perforated-fin tubes. The overall heat transfer improvement varied. Results for laminar flow showed a 40-50% enhancement in overall heat transfer. In turbulent flow the best improvement was in the order of 12%. They concluded that the formation of the liquid film on the solid surface is the main reason for the heat transfer augmentation. The contribution of evaporation was considered negligible.

Experiments and simulations on deluge cooling by Leidenfrost and Korenic (1982) lead them to predict a 50% saving of energy consumption in air-cooled devices such as air conditioners and refrigeration systems when evaporative pre-cooling is applied. They extended this to predict 10-15% improvement in power production at typical fossil fuel power plants. They concluded that the difficulty in obtaining complete and uniform wetting of the heat exchanger surface was one of the reasons for the

reluctance to use this technology. Dry spots would decrease performance and increase fouling.

An analysis of the corrosion behavior of galvanized fin tubes under deluge conditions was conducted by Woest et al. (1991). Using both potable (municipal supply) and demineralized water the tubes were subjected to various deluging cycles. It was found that deluging with the demineralized water resulted in negligible deposits and corrosion when compared to potable water deluging. The use of demineralized water, however, can be expensive, resulting in high running costs of such an application.

Kriel (1991) analyzed and tested the performance of spray-cooled heat exchangers. He developed various mathematical models for the analysis of spray-cooled finned-tube heat exchangers. Based on these models, he developed a set of computer programs to predict the operation of the heat exchanger. Experiments were performed to verify the computer models and it was found that the performance of these heat exchangers could be predicted to within 20% of experimental values. Performance improvement of between 1.4 and 3.5 times that of dry operation was found by spraying relatively small amounts of water into the heat exchanger. Further experiments on the pressure drop over the bundle indicated that a maximum water flow rate existed for each configuration. Beyond this maximum the pressure drop across the bundle increased dramatically. This phenomenon was attributed to congestion of the fin gaps by excess water.

Dry surface cooling

Concerns over corrosion, solid deposition and increased pressure drop as a result of fin congestion prompted research into the use of a very fine water spray for pre-cooling, where the droplets have evaporated before they reach the heat exchanger surface. This prevents the surfaces from getting wet. This type of spray cooling can be termed “mist cooling” or “fogging”.

Wachtell (1974) investigated the manner in which the efficiency of a mist-cooled heat exchanger is affected by the size of the droplets in the spray. He determined that a maximum droplet size of 20 micron is required to ensure that the inlet air cools to

near-wetbulb temperatures and to prevent the heat exchanger surface from becoming wet. He found that it would be expensive to generate these extremely fine droplets, but suggested that rotating pneumatic sprayers might be a more affordable method of achieving the desired droplet size.

In tests conducted on the heat exchanger for a cooking oil refinery, Rubin (1975) found that while using droplets of 20 micron at low air speeds, the surface of the heat exchanger remained dry, even when the air was saturated with vapor. However, the colder parts of the heat exchanger showed some wetting. Rubin concluded that the pneumatic (air-driven) atomizers, used to generate the required drop sizes, were expensive to operate. The atomizing power required to generate the required size droplets was found to be the most expensive component in the study.

Conradie (1990) identified two control philosophies of pre-cooling the air for dry surface applications. The first would be to cool to a specified relative humidity while the second would be a constant rate of water injection. Cooling to a specified relative humidity would allow for a wider range of temperatures that could be achieved effectively, but more water would be used and a more complex control system would be required. Conradie (1990) adapted existing computer programs, developed for the analysis of a power plant with a natural draft dry-cooling tower, to include pre-cooling of the inlet air. The improvement in actual power output from the plant when air was cooled to a specified relative humidity was found to be only 0.1-2.95%. The power needed for the pneumatic atomizing was determined to be the main factor of the cost of operating an adiabatic cooling system.

Duvenhage (1993), using a model similar to Watchtell (1974) and Masters (1985), showed that, in dry air, all the droplets in a spray with a maximum allowable droplet diameter of 50 μm would have evaporated before the droplets reach the heat exchanger, thereby preventing wetting of the surface of the heat exchanger. He did not, however, consider what happens to droplets once they have entered the boundary layer formed around the surface of the heat exchanger.

Bhatti and Savery (1975) investigated the augmentation of heat transfer in a laminar external gas boundary layer by the vaporization of suspended droplets. Their research was prompted by the concept of utilizing fog or mist cooling to enhance dry cooling performance during temporary periods of high ambient dry bulb temperatures and power demand. They developed a theory for the two-phase flow regime where droplets suspended in a gas stream penetrate the boundary layer and evaporate without deposition. Their results indicated that droplets between 10 and 50 μm diameter would evaporate in the boundary layer. Droplets smaller than 10 μm diameter will not penetrate the boundary layer. They also showed that the heat transfer coefficient could be markedly enhanced when droplets are introduced into the boundary layer at sufficiently high mass fluxes. Their results are shown in figure 2.4. They found that for constant droplet flux, the larger diameter droplets caused greater enhancement in the heat transfer coefficient. This greater enhancement is due to greater vaporization rates, which result from increased exposure time and penetration of the larger-sized droplets. The figure also shows that as the droplet flux in the main stream increases, the performance enhancement for the same diameter droplet also increases. This is to be expected since the increase in droplet flux implies that a greater number of droplets are available for vaporization.

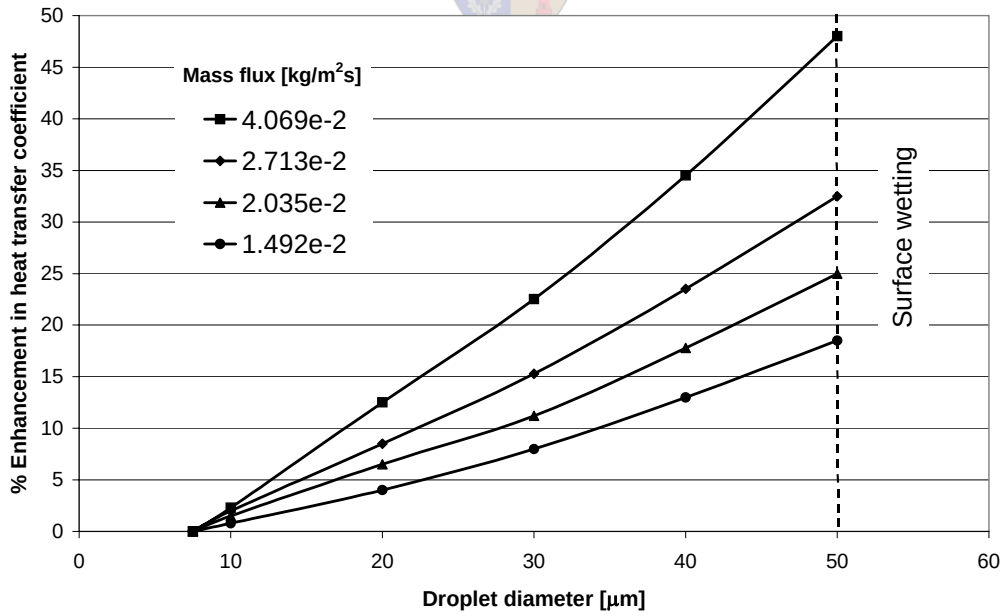

Figure 2.4 Dependence of heat transfer coefficient on droplet diameter and mass flux

Judging from the current literature, there are basically three distinct evaporative cooling technologies. They consist of deluge cooling, spray cooling and “mist cooling”. With deluge cooling the heat exchanger is entirely covered with water, and the heat transfer augmentation is mainly due to the formation of the liquid film on the solid surface. The contribution of evaporation is negligible (Yang and Clark, 1975). Spray cooling comprises of spraying the heat exchanger with fine droplets. The surface of the heat exchanger is wetted by the droplets and heat transfer augmentation is achieved mainly by the evaporation of the droplets. “Mist cooling” consists of spraying the heat exchanger with an ultra fine water spray, ensuring that the droplets have been completely evaporated before they reach the heat exchanger surface and thereby preventing wetting of the surface (Wachtell, 1974; Conradie, 1990). This research will focus on finding a method of achieving “mist cooling” in an effective manner.

2.3 Discussion

A lot of theoretical work has been done on adiabatic cooling. The results of both Oplatka (1981) and Conradie (1991) clearly indicate the benefits of adiabatic cooling when applied under adverse atmospheric conditions. Neither author, however, addresses the problem of achieving the required droplet size to ensure evaporation of the droplets before they reach the heat exchanger surface. Judging from previous research, the most challenging aspect is achieving droplets of sufficiently small size at relatively low cost. Duvenhage (1993) tested several hydraulic atomizing nozzles to attain the required droplet size of 50 μm. Results indicated that the pressure required to reach this degree of atomization was excessive. The additional capital outlay for high-pressure pumps and piping would negate the positive economic return from the enhanced cooling. In an effort to find a cheaper atomization method, attention was turned towards rotary atomizers and a few models were tested. Operating costs of these atomizers were found to be 16 times less than a comparable pneumatic device. These atomizers, however, are relatively expensive compared to pneumatic nozzles. Duvenhage (1993) concluded that, although rotary atomizers appeared to be effective, a cheaper model should be designed before actual implementation.

Botes (1995) designed and tested a rotary atomizer. He found that he could not achieve the required droplet sizes, and recommended that drift eliminators be used downstream of the atomizers to catch larger droplets and thereby preventing the heat exchanger surface from becoming wet. The drift eliminators, however, would result in an increased pressure drop through the system.

Botes (1995) also considered the option of installing new fan motors and gear sets to increase the airflow across the heat exchanger surfaces, thereby increasing the heat transfer. He performed an economic analysis for an existing petrochemical plant with both the adiabatic cooling and the installation of new fan motors and gear sets. He considered only the installation costs of the new fans and not the operational costs. The cost of installing adiabatic cooling was found to be 72% of that of installing new fan drives. This figure was reduced to 51% if the drift eliminators were not required. Kritzinger (1999) designed and tested a rotating sprayer, fitted on the same shaft as the cooling fan, as shown in figure 2.5. The rotating shaft acted as a pump delivering cooling water to high-pressure nozzles on the rotating sprayer. This concept eliminated the need for high-pressure pumps. Experimental work done to verify the concept proved that the design is effective in delivering the atomized water droplets, but the average drop size was too large for application in air-cooled heat exchangers. A considerable increase in fan power consumption was also measured. The source of the additional power requirement was traced to form drag exerted on the sprayer as it moves through the air.

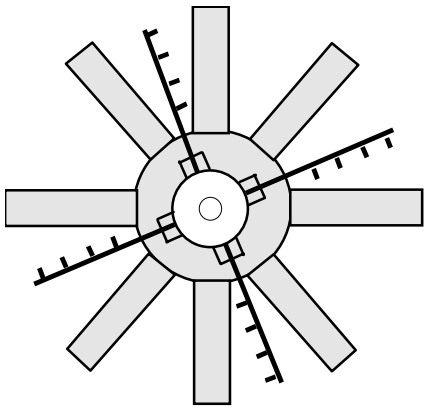

Figure 2.5 A rotating sprayer fitted onto a fan

In an effort to make use of the heat transfer benefits of introducing droplets into the boundary layer formed around the heat exchanger fins, as discussed by Bhatti and Savery (1975). Branfield (2003) performed tests and experiments using a humidifier to produce water droplets in the inlet air stream. It was believed that this humidifier produced droplets smaller than 10 micron. His tests indicated that even droplets of this size caused wetting of the leading edge of the heat exchanger fins. He predicted that no matter how small the droplets entering the heat exchanger, some of them would always impact the leading edge of the fins.

2.4 Conclusion

Judging from the review of literature, there is clearly major benefit to be gained from making use of evaporative inlet cooling. However, no reliable method has been found to ensure that this can be achieved in a sustainable manner. Throughout all the research, the problem of corrosion and fouling of the fins in the event of the droplets impacting the surface has been a major concern. Duvenhage (1993) and Botes (1995) showed that droplets of 50 micron and smaller, used in a standard ACHE facility, would evaporate before they have reached the heat exchanger surface. Following the work by Duvenhage (1993) and Botes (1995), much research had been devoted to finding methods of producing this desired droplet size cheaply and effectively (Botes, 1995; Kritzinger, 1999). The prediction that droplets of 50 micron would be sufficient to prevent wetting of the heat exchanger surface, however, rely heavily on many variable parameters, such as the height of the heat exchanger above the fans and the inlet temperature and humidity of the incoming air. Any change in these parameters would affect the allowable droplet size that will ensure evaporation before the heat exchanger surface is reached. This method of inlet air pre-cooling also does not make use of the major benefits of introducing the droplets into the boundary layer formed around the fins, as predicted by Bhatti and Savery (1975). In order to make use of these benefits, a method has to be found to ensure that the droplets enter the boundary layer around the heat exchanger fins, but do not impact the surface of the fins. Branfield (2003) attempted this by injection very small droplets, in the order of 10 microns, into the boundary layer around the fins. He found that the performance of the

heat exchanger greatly improved. However, he found that there was still wetting of the surface, but this was confined to the leading edge of the fin.

The work done by Branfield (2003) indicates that the biggest challenge is to ensure that the leading edge of the heat exchanger fin, where the boundary layer is extremely thin, remains dry. The focus of this study will be to achieve this by making use of electrostatic charging of the droplets and placing a charge of similar polarity on the heat exchanger to ensure that the droplets are repelled from the surface as they near it. A full description and literature study of this method is given in chapter 7.

3 Mechanisms of atomization

This chapter gives a short discussion on the atomization process, describing the forces causing the break-up of a liquid droplet. The Weber number is defined in this chapter.

3.1 Introduction

The atomization process is essentially a process whereby a bulk liquid is converted to individual droplets. This is achieved by the disruption of the consolidating influence of surface tension by the action of external and internal forces. Surface tension tends to pull the liquid into the form of a sphere, since this configuration has the minimum surface energy. Liquid viscosity exerts a stabilizing influence by opposing any change in system geometry. The aerodynamic forces acting on the liquid surface promotes the disrupting process by applying distorting forces to the bulk liquid. Breakup occurs when the disruptive force just exceeds the consolidation influence of surface tension. Some of the larger drops produced in the initial atomization process are unstable and disintegrate further, producing a wide distribution of droplet sizes in the spray. The final distribution of the spray thus depends greatly on the extent to which the initial drops are further disintegrated during secondary atomization.

3.2 Weber number

It is of interest to examine the mechanisms involved when atomization occurs as a result of interaction between a liquid and the aerodynamic forces of the surrounding air. An accurate mathematical solution for the breakup of a drop would require an exact knowledge of the distribution of the aerodynamic pressures on the drop. As the drop is deformed by the aerodynamic pressures, the pressure distribution around the drop changes, and either a state of equilibrium between the external forces (aerodynamic) and internal forces (surface tension and viscosity) is attained, or further deformation follows, leading to possible further breakup of the drop. The influence of

the variations in air pressure distribution around a drop was examined by Klüsener (1933). Consider the droplet shown in figure 3.1. For static equilibrium, the surface tension force balances the net pressure force.

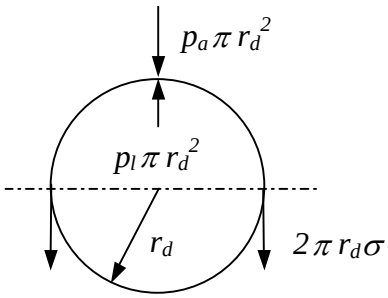

Figure 3.1 Force balance of forces acting on a spherical droplet

$$p_l \pi r_d^{\,2} - p_a \pi r_d^{\,2} = 2\pi r_d \sigma \tag{3.1}$$

$$\left(p_l - p_a\right) = \frac{2\sigma}{r_d} = constant \tag{3.2}$$

A drop can remain stable as long as a change in air pressure, p_a, at any point on its surface can be compensated for by a change in internal pressure, p_l, such that the term on the right-hand side of equation (3.2) remains constant. If p_a is large compared to p_l , then any appreciable change in p_a cannot be compensated for by a corresponding change in p_l to maintain $\frac{2\sigma}{r_d}$ constant. In this situation the external pressure may deform the drop to such an extent that leads to disruption of the drop into smaller drops. From equation 3.2 it can be seen that a smaller droplet radius results in an increase in the constant on the right-hand side of equation (3.2). This new value may be large enough to accommodate the variations in p_a. If not, further breakup will occur until the pressure differential, $\left(p_l - p_a\right)$ equals the constant surface tension force on the right-hand side of equation (3.2). At this stage equilibrium has been reached and no further breakup will occur.

In general, the breakup of a droplet in a moving air stream is controlled by dynamic pressure, surface tension and viscous forces. For liquids of low viscosity, the deformation is determined primarily by the ratio of the aerodynamic forces, represented by

$$0.5\rho_a u_R^{\ 2} \tag{3.3}$$

and the surface tension forces, which are related to

$$\frac{\sigma}{d} \tag{3.4}$$

Forming a dimensionless group from these two opposing forces yields the Weber number

$$We = \frac{\rho_a u_R^{\ 2} d}{\sigma} \tag{3.5}$$

The higher the Weber number, the larger are the deforming external pressure forces compared with the consolidation influence of surface tension.

4 Free stream droplet evaporation

This chapter investigates the evaporation times associated with water droplets evaporating in a free stream under a variety of ambient conditions. A mathematical model, based on the model proposed by Lefebvre (1989), is used to derive an equation for the evaporation time of a liquid droplet in moving air. The equation is verified by experimental and analytical results.

4.1 Introduction

The evaporation of drops in a spray involves a heat and mass transfer process whereby heat is transferred to the drop surface by means of conduction and convection from the surrounding air or gas and mass is transferred from the drop surface to the surrounding air or gas by means of diffusion and convection. The overall rate of evaporation depends on the pressure, temperature, relative humidity and transport properties of the gas, the temperature, volatility and diameter of the drops in the spray and the velocity of the drops relative to that of the surrounding gas.

The rates of heat and mass transfer are markedly affected by the drop Reynolds number, whose value varies throughout the lifetime of the drop, since neither the drop size or velocity remains constant. The history of the drop velocity is determined by the relative velocity between the drop and the surrounding gas and also by the drag coefficient. After a certain time has elapsed the drop will attain its steady state condition or wetbulb temperature corresponding to the prevailing conditions.

The development of drop evaporation theory has been largely motivated by the necessity of knowledge of fuel evaporation rates for the design of aero gas turbines and liquid propellant rocket engines. The approach generally followed is that proposed by Godsave (1953), Spalding (1953) and Lefebvre (1989). They assumed a spherically symmetrical model of a vaporizing drop in which the rate controlling process is molecular diffusion. The following assumptions are usually made:

- The drops are spherical.
- The droplets in the spray are assumed to be of uniform size.
- Radiation heat transfer is negligible.
- The evaporating liquid is a pure liquid having a well-defined boiling point.
- Complete internal mixing was assumed. The entire drop was assumed to be at the wetbulb temperature of the air (therefore steady-state conditions apply).

Except for conditions of very low pressure, these assumptions are considered valid.

4.2 Steady state analysis

Mass transfer number

An expression for the rate of evaporation of a liquid drop may be derived as follows. More rigorous and comprehensive treatments are provided in articles by Feath (1977), Spalding (1953) and Williams (1976).

Consider a spherical droplet with a control volume on the surface of the droplet, as shown in figure 4.1.

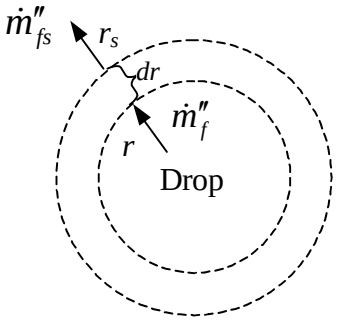

Figure 4.1 Liquid droplet with mass transfer

The diffusion rate is given by Fick's law of diffusion (Kröger, 2004), which states that the mass flux of a constituent per unit area is proportional to the concentration gradient:

$$\dot{m}'' = -D\frac{dc}{dr} \tag{4.1}$$

Making use of the perfect gas law equation (4.1) can be rewritten in terms of fuel mass fraction and air mass fraction as

$$\frac{dY_f}{dr} = -\frac{RT}{DP}\left(\dot{m}''_f Y_a\right) \tag{4.2}$$

with Y_f = fluid mass fraction

Y_a = air mass fraction

$\dot{m}''_f$ = mass flux, [kg·s^{-1}·m^{-2}]

D = diffusion coefficient, [m^2·s^{-1}]

P = pressure, [N·m^{-2}]

T = temperature, [K]

r = drop radius (r_0 at center of drop, r_s at surface of drop), [m]

From continuity

$$\dot{m}''_{fs} A_s = \dot{m}''_f A$$

$$\dot{m}''_{fs} \cdot 4\pi \cdot r_s^{\,2} = \dot{m}''_f \cdot 4\pi \cdot r^2 \tag{4.3}$$

Substitute equation (4.3) into equation (4.2)

$$\frac{dY_f}{dr} = -\frac{RT}{DP} Y_a \dot{m}''_{fs}\left(\frac{r_s^{\,2}}{r^2}\right) \tag{4.4}$$

Since $Y_a = 1 - Y_f$

$$\frac{dY_f}{dr} = -\frac{RT}{DP}(1-Y_f)\dot{m}''_{fs}\left(\frac{r_s^{\,2}}{r^2}\right) \tag{4.5}$$

Separate variables and integrate with the following boundary conditions:

At $\begin{matrix} r = r_s, T = T_s, Y_f = Y_{fs} \\ r = \infty, T = T_\infty, Y_f = Y_{f\infty} = 0 \end{matrix}$

The assumption first proposed by Spalding (1953) that mass flux is zero at the liquid surface will be used as an additional boundary condition. Integrating between r_s and ∞ yields:

$$\dot{m}''_{fs} = -\ln(1-Y_{fs})\frac{\rho_a D}{r_s} \tag{4.6}$$

Combining equations (4.3) and (4.6) yields:

$$\dot{m}_f = -4\pi \cdot r_s \ln(1-Y_{fs})\rho_a D \tag{4.7}$$

The Lewis number is an indication of the relative rates of heat and mass transfer in an evaporative process. A common simplifying assumption in evaporation analysis is to assume a Lewis number of unity. Under this assumption, the quantity $\rho_a D$ can be replaced with $(k/c_p)_a$

Now define $B_M = \dfrac{Y_{fs}}{1-Y_{fs}}$

then

$$\ln(1-Y_{fs}) = -\ln(1+B_M) \tag{4.8}$$

Therefore

$$\dot{m}_f = 2\pi \cdot d_s \left(\frac{k}{c_p} \right)_a \ln(1 + B_M) \tag{4.9}$$

By noting that $m = N \cdot M$, with the gas constant determined from the perfect gas law, Y_f can be calculated from

$$Y_{fs} = \left[1 + \left(\frac{P_t}{P_{fs}} - 1 \right) \frac{M_a}{M_f} \right]^{-1} \tag{4.10}$$

Heat transfer number

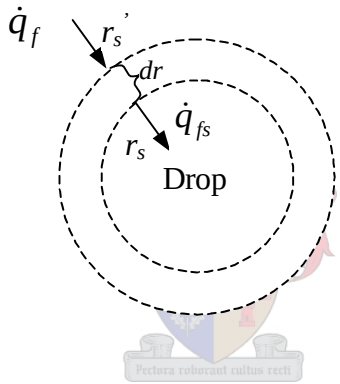

Figure 4.2 Liquid droplet with heat transfer

Consider a control volume of a thin shell surrounding an evaporating drop, as shown in figure 4.2.

Making use of Fourier's law of conduction (Kröger, 2004)

$$\dot{q} = -kA \frac{dT}{dr} \tag{4.11}$$

and an equation for the latent heat transferred due to evaporation

$$\dot{q} = -\dot{m} h_{fg} \tag{4.12}$$

and integrating across the control volume, in a similar manner as to the mass transfer number, leads to the following expression for the heat transfer number

$$B_T = \frac{c_{pa}\left(T_\infty - T_s\right)}{h_{fg}} \tag{4.13}$$

The number B_T denotes the ratio of available enthalpy in the surrounding air to the heat required to evaporate the liquid. It therefore represents the driving force for the evaporation process when heat transfer rates are controlling.

If it assumed that the droplet is surrounded by other evaporating droplets, adiabatic cooling will cause T_∞ to change, tending towards the wetbulb temperature of the air as evaporation increases.

Assume T_{dbi} and T_{dbf} are the initial and final drybulb temperatures of the air respectively. The change in temperature, (T_{dbi} - T_{dbf}), is directly proportional to the absorption of latent heat. The latent heat extracted from the surrounding air causes water from the surface of the droplet to evaporate, and as a result a decrease in droplet mass. T_∞ is therefore directly proportional to r_d^3, and can be written the following linear function of r_d^3

$$T_\infty = T_{dbf} + \left(T_{dbi} - T_{dbf}\right)\frac{r_d^{\,3}}{r_{d0}^{\,3}} \tag{4.14}$$

When heat transfer rates are controlling for evaporation, the rate of evaporation for a Lewis number of unity is obtained as

$$\dot{m}_f = 2\pi \cdot d_s \left(\frac{k}{c_p}\right)_a \ln\left(1 + B_T\right) \tag{4.15}$$

For steady state conditions, $B_M = B_T = B$, and equation (4.9) or (4.15) can be used to calculate the rate of evaporation.

Evaporation constant

Godsave (1953) defined an evaporation constant

$$\lambda = \frac{d\left(d^2\right)}{dt} \tag{4.16}$$

Assuming λ remains constant and integrating twice yields

$$t_e = \frac{d_s^{\,2}}{\lambda_{st}} \tag{4.17}$$

Godsave and his co-worker Probert (1946) showed that the evaporation equation for a drop could be given by

$$\dot{m}_f = \frac{\pi}{4} \cdot \rho_f \cdot \lambda \cdot d_s \tag{4.18}$$

Combining equations (4.18) and (4.15) for a steady state yields

$$\lambda_{st} = \frac{8 \cdot k_a \ln\left(1+B\right)}{c_{pa}\rho_f} \tag{4.19}$$

Combining equations (4.17) and (4.19) gives

$$t_e = \frac{\rho_f d_s^{\,2}}{8 \cdot \left(k_a / c_{pa}\right)\ln\left(1+B\right)} \tag{4.20}$$

Convective effects on evaporation

In a comprehensive theoretical and experimental study, Frossling (1938) showed that the effects of convection on heat and mass transfer rates could be accommodated by a

correction factor that is a function of the Reynolds number and Schmidt (or Prandtl) number.

Where diffusion rates are controlling, the correction factor is

$$1 + 0.276 \cdot \mathrm{Re}_d^{0.5}\, Sc_a^{0.33} \tag{4.21}$$

For the more usual case, where heat transfer rates are controlling, the expression is

$$1 + 0.276 \cdot \mathrm{Re}_d^{0.5}\, \mathrm{Pr}_a^{0.33} \tag{4.22}$$

where the velocity term in Re_d is the relative velocity between the drop and the moving air (or gas). Duvenhage (1993) derived the following equation in terms of droplet diameter for the relative velocity between a droplet and an air stream moving at 3 m/s:

$$u = 5.05e^{9} \cdot d_d^{\,3} + 2.86e^{7} \cdot d_d^{\,2} + 16.48 \cdot d_d \tag{4.23}$$

This equation will be used in the subsequent calculations to determine the relative velocity and drop Reynolds number.

Making use of the study by Frossling (1938), Ranz and Marshall (1952) correlated data from several experiments with evaporating liquid droplets. The experimental work was performed by suspending a liquid drop from a feed capillary in a laminar jet. The air temperature varied between 25 ^{o}C and 200 ^{o}C and the Reynolds number between 2 and 200. A fine thermocouple wire was placed through the drop to measure the temperature of the suspended drop. The data was correlated with the following equations:

$$Nu = 2 + 0.6 \cdot \mathrm{Re}_d^{0.5}\, \mathrm{Pr}_a^{0.33} \tag{4.24}$$

$$Sh = 2 + 0.6 \cdot \mathrm{Re}_d^{0.5}\, Sc_a^{0.33} \tag{4.25}$$

which corresponds to a correction factors of

$$1 + 0.3 \cdot \mathrm{Re}_d^{\,0.5}\, \mathrm{Pr}_a^{\,0.33} \tag{4.26}$$

$$1 + 0.3 \cdot \mathrm{Re}_d^{\,0.5}\, Sc_a^{\,0.33} \tag{4.27}$$

Combining equations (4.15) and (4.26) for a steady state gives an equation for the instantaneous rate of evaporation for a drop of diameter *d* with forced convection

$$\dot{m}_f = 2\pi \cdot d_s \left(\frac{k}{c_p}\right)_a \ln(1+B)\left(1 + 0.3 \cdot \mathrm{Re}_d^{\,0.5}\, \mathrm{Pr}_a^{\,0.33}\right) \tag{4.28}$$

To obtain the average rate of evaporation during the lifetime of the drop, the constant must be changed from 2 to 1.333. Substituting also $\bar{d} = 0.667 d_0$ and *Pr* = 0.7 yields

$$\dot{m}_f = 1.33\pi \cdot d_s \left(\frac{k}{c_p}\right)_a \ln(1+B)\left(1 + 0.22 \cdot \mathrm{Re}_d^{\,0.5}\right) \tag{4.29}$$

and

$$t_e = \frac{\rho_f d_s^{\,2}}{8 \cdot (k_a / c_{pa}) \ln(1+B)(1 + 0.22 \cdot \mathrm{Re}_d^{\,0.5})} \tag{4.30}$$

4.3 Results

Verification of model by experimental results

The equations derived in the previous section can be verified by comparing the theoretical model with experimentally determined values. Unfortunately, no experimental values for the present conditions could be found in literature. Hall and Diederichsen (1953) performed an experimental study of the burning of single drops of fuel in air. They obtained their droplets by feeding liquid onto a rotating disc. Droplets of uniform size were thrown off tangentially from the disc. The droplets then passed through a slot and into a rectangular chamber with heaters on the sides. The temperature in the chamber was kept constant at approximately 710 ^{o}C. The results they obtained for the evaporation of liquid paraffin are compared to the previously derived theoretical model in the double logarithmic graph in figure 4.3.

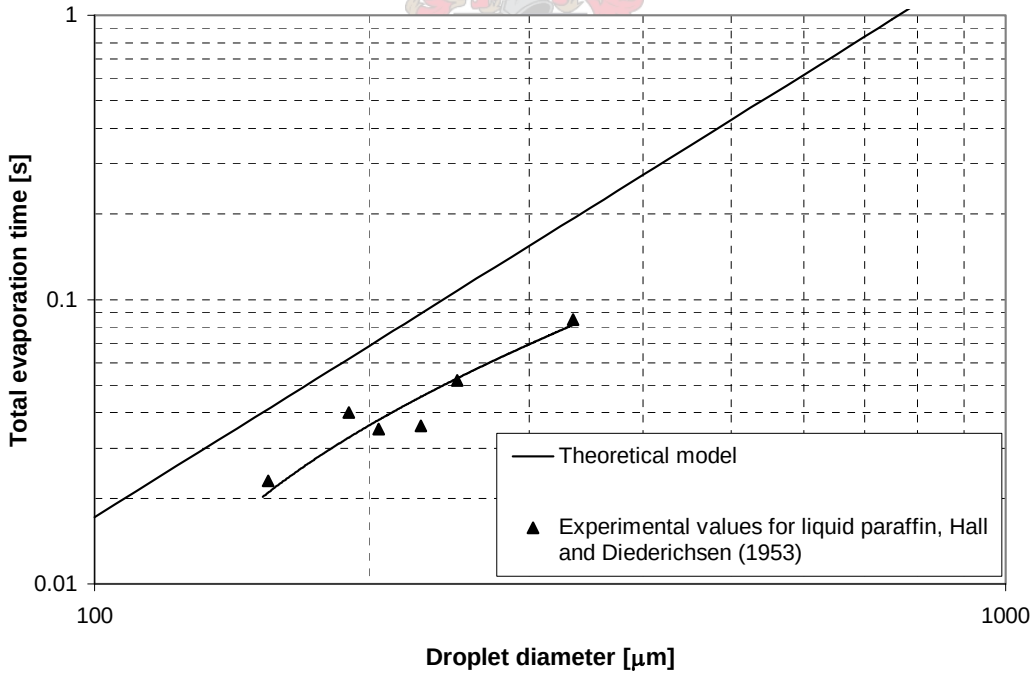

Figure 4.3 Graph of evaporation time of liquid paraffin: theoretical and experimental values

The evaporation times predicted by the theoretical model are somewhat higher than the experimental values found by Hall and Diederichsen (1953). However, one significant aspect of the graph shown in figure 4.3 is that the two lines have the same gradient. This indicates that the theoretically predicted values display the same trend as the experimentally determined values. The difference between the two lines can be accounted for by some additional factor incorporated into the theoretical model.

A possible explanation for the difference in the experimental and theoretical values is the effect of the relative velocity between the droplet and the surrounding air as it leaves the rotating disc and enters the heating chamber. Hall and Diederichsen (1953) make no mention of rotational speed of the disc or the velocity of the droplets in the heating chamber. The values found with the theoretical model are for a situation with no relative velocity between the droplet and the surrounding air, and therefore no heat transfer by convection. If the convection heat transfer is taken into account, the theoretically predicted values will tend towards the experimentally determined values. Figure 4.4 shows the theoretical values for a relative velocity of 10 m/s. These predicted theoretical values correspond very well with the experimentally determined values.

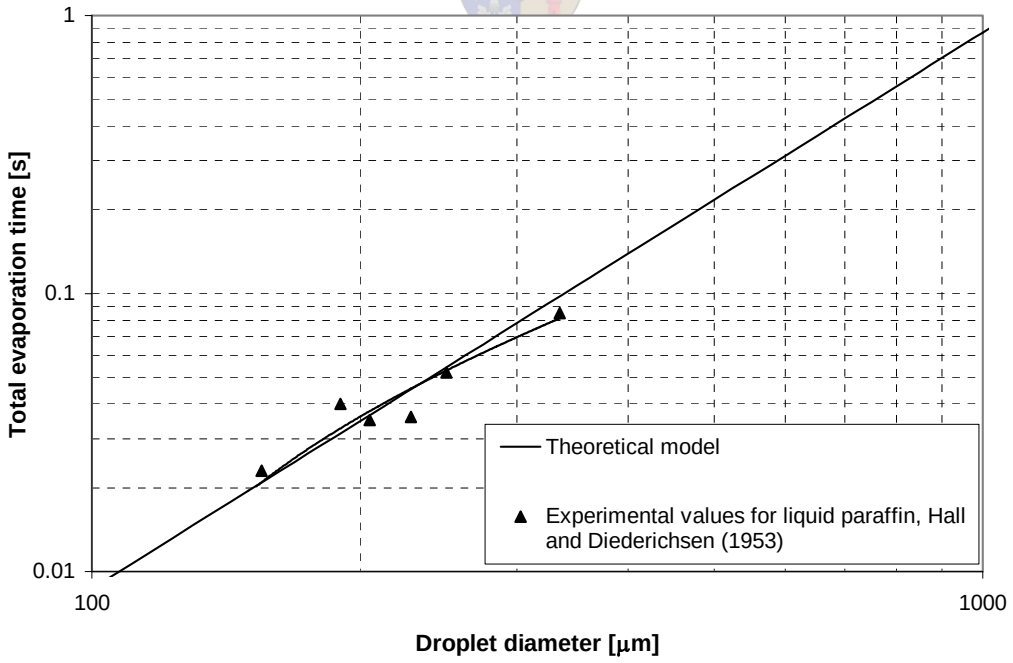

Figure 4.4 Graph of evaporation time of liquid paraffin:
theoretical and experimental values

Verification of model by analytical results

An alternative method to verify the theoretical model is to compare the results to previously derived analytical results. The theoretical model derived above is similar to the model derived by Lefebvre (1989), except that he examines a single droplet evaporating alone.

Duvenhage (1993) made use of a similarly simplified analytical model to derive the following equation for the change in drop diameter with time:

$$-\frac{dr_d}{dt} = \frac{Nu \cdot k_a}{2 \cdot \rho_w \cdot h_{fg} \cdot r_d}\left[(T_{dbf} - T_{wb}) + (T_{dbi} - T_{dbf})\frac{r_d^{\,3}}{r_{do}^{\,3}}\right] \tag{4.31}$$

By assuming negligible effects of relative velocity (Nu = 2, Ranz and Marshall, 1952) and integrating with the following boundary conditions

$t = 0, \quad r_d = r_{do}$

$t = t_f, \quad r_d = 0$,

he derived the following equation for the evaporation time for a liquid drop in a moving air stream

$$t_f = \frac{S}{r_{do}} \cdot \frac{r_{do}^3}{T_{dbi} - T_{dbf}} \cdot \frac{\rho_w \cdot h_{fg}}{k_a} \cdot F(S) \tag{4.32}$$

with

$$F(S) = 0.57735 \cdot \tan^{-1}(1.1547 \cdot S - 0.57735) + 0.302299 - \frac{1}{3} \cdot \ln(S+1) + \frac{1}{6} \cdot \ln(S^2 - S + 1) \tag{4.33}$$

and

$$S = \left[\frac{T_{dbi} - T_{dbf}}{T_{dbf} - T_{wb}} \right]^{1/3} \tag{4.34}$$

Kritzinger (1999) made use of some simplifying assumptions to derive an equation for the rate of change of drop diameter in terms of heat transfer as

$$\frac{d(d_d)}{dt} = -\left(\frac{2 \cdot Nu \cdot k_a}{\rho_w \cdot h_{fg} \cdot d_d} \right) \cdot (T_\infty - T_d) \tag{4.35}$$

or in terms of mass transfer as

$$\frac{d(d_d)}{dt} = Sh \cdot (\rho_w \cdot D_w) \cdot \pi \cdot d_d \cdot (\omega_\infty - \omega_d) \tag{4.36}$$

He made use of numerical methods to solve these equations. The major difference between the approach by Kritzinger (1999) and the approach by Duvenhage (1993) is that Kritzinger took the effect of relative velocity between the drop and the surrounding air into account.

Comparisons of the present theoretical model and the models of Lefebvre (1989), Duvenhage (1993) and Kritzinger (1999) for water droplets entrained in a 3 m/s air stream are shown in figures 4.5 to 4.7. The final dryblub temperature of the air is 28 ^{o}C and wetbulb temperature of the air is 18 ^{o}C. It is assumed that the droplets enter the system at the wetbulb temperature of the air. The total evaporation times for different sized droplets were plotted against the initial drybulb temperature.

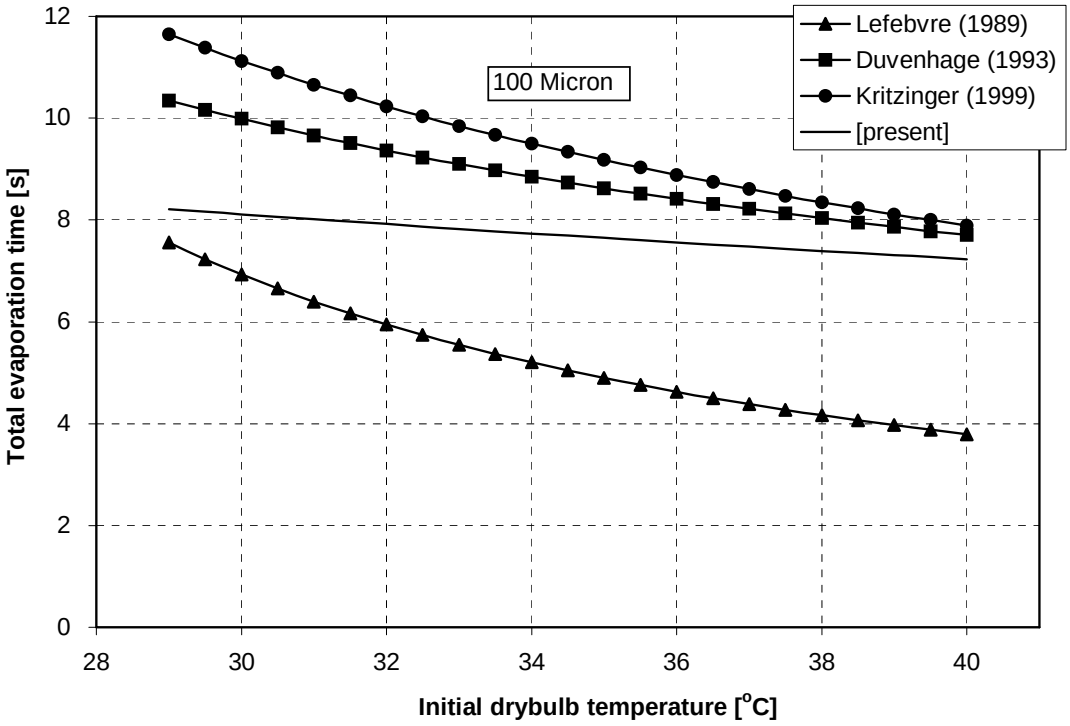

Figure 4.5 Graph of evaporation times for 100 micron diameter water droplets

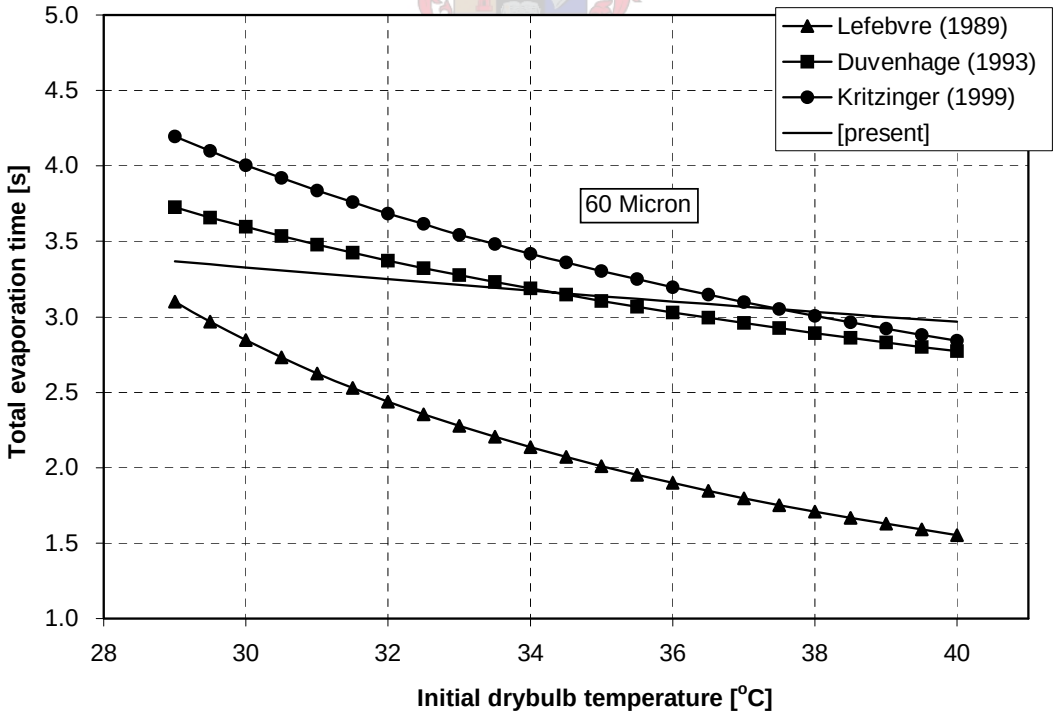

Figure 4.6 Graph of evaporation times for 60 micron diameter water droplets

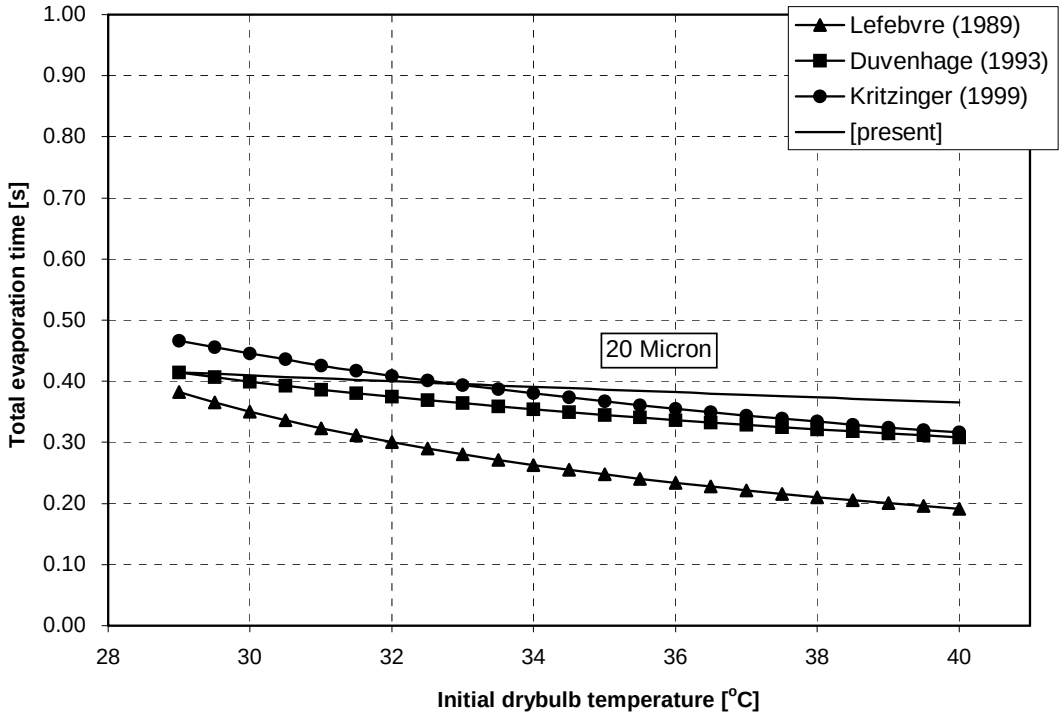

Figure 4.7 Graph of evaporation times for 20 micron diameter water droplets

Figure 4.5 shows the total evaporation times against initial drybulb temperature for a 100 μm droplet. The models of Duvenhage (1993) and Kritzinger (1999) predict similar evaporation times. The difference between them is as a result of Duvenhage (1993) assuming the effect of relative velocity to be negligible. The model of Lefebvre (1989) predicts the lowest evaporation times. The reason for this is that he assumes T_∞ to remain constant. The values predicted by the current model are somewhat higher because of the fact that the current model makes use of an average T_∞ in the calculation. Figures 4.6 and 4.7 show that the differences in the models become smaller as the droplet size decreases.

A further comparison of the model by Lefebvre (1989) and the current model is shown in figure 4.8. This figure shows the decrease in total evaporation time when the relative velocity between the droplet and the air is taken into account.

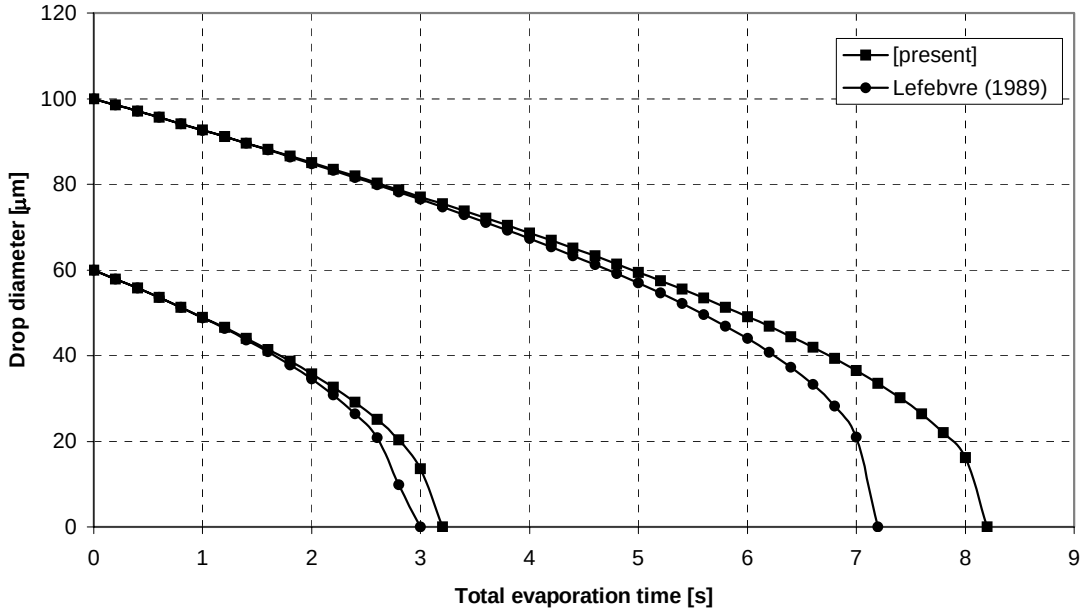

Figure 4.8 Graph of droplet diameter against time for evaporating water droplets

4.4 Discussion

Theoretical equations based on the work by Lefebvre (1989) were derived for the mass flow rate and drop lifetime of a liquid droplet evaporating in a gas stream. Results from the theoretical equations compare well with experimental results as well as previous analytical results. The behavior of a droplet can now be predicted from the moment it issues from the nozzle orifice to the moment it either impacts a surface or the moment it enters a hydrodynamic boundary layer. The behavior of a droplet once it has entered a hydrodynamic boundary layer will be investigated in the following chapter.

5 Droplet evaporation and heat transfer augmentation in a boundary layer – horizontal plate

This chapter describes the mathematical model derived, following a similar approach to the one proposed by Bhatti and Savery (1975), for predicting the behavior of a liquid droplet in a laminar gas boundary layer on a flat plate. At the end of the chapter the model derived is combined with the model derived in the previous chapter for the evaporation of droplets in the free stream to give a model for the evaporation of a droplet during its entire lifetime.

5.1 Introduction

The equations of motion are derived for liquid droplets penetrating the laminar hydrodynamic gas boundary layer on a flat surface and vaporizing therein. Stoke's drag, buoyancy, and gravitational forces are taken into account. For this particular plate configuration, the force on the droplet due to its rotation was found to have a negligible effect and was therefore omitted from the model. This force has an effect in the vertical plate model, and was added for that model (chapter 6). Free stream turbulence superimposed on the boundary layer is assumed to cause the initial transverse velocity component that propels the droplets towards the solid surface. By simultaneous solution of transverse and flow direction equations of motion, an expression for the exposure time of the droplets in the boundary layer can be found.

The following assumptions are made:

- The droplets obey Stoke's law and therefore the analysis is applicable to droplets with Reynolds number less than unity.
- The velocity and temperature of the droplets in the free stream are the same as those of the gas phase.
- The flow in the two-component, two-phase stream is laminar, steady, incompressible, and involves Newtonian fluids with constant properties.

- The transverse velocity component of the laminar gas boundary layer is ignored.
- The free stream turbulence is isotropic and the level of the turbulence is relatively small. The laminar boundary layer therefore remains unaffected.
- A linear velocity profile is assumed across the boundary layer. This assumption will be explained in more detail at the appropriate point in the analysis.

5.2 Transverse direction equation of motion

A water droplet entering a boundary layer on a horizontal flat plate is shown in figure 5.1. The forces acting on the droplet in the transverse direction are gravity (downwards) and the buoyancy force and drag force (upwards).

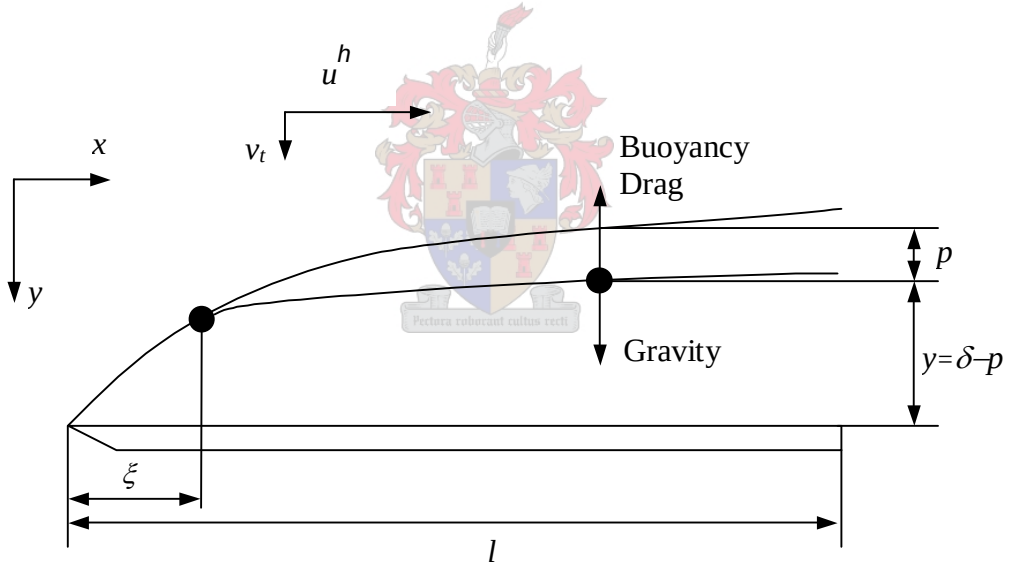

Figure 5.1 Schematic of a liquid droplet in a gas boundary layer

According to Newton's second law of motion

$$\frac{d}{dt}\left(m\frac{dp}{dt}\right) = mg - mg\left(\frac{\rho}{\rho_l}\right) - 6\pi\mu r\frac{dp}{dt} \tag{5.1}$$

Expressing *m* in terms of *r*, simplifying and rearranging yields

$$\frac{d^2p}{dt^2}+\left(\frac{3}{r}\frac{dr}{dt}+\frac{9\mu}{2\rho_l r^2}\right)\frac{dp}{dt}=\left(1-\frac{\rho}{\rho_l}\right)g \tag{5.2}$$

The vaporization rate is used to determine the variation of droplet size with time (Savery, 1971)

$$\frac{dm}{dt}=\frac{2\pi rM\rho DSh}{\overline{M}}\ln\left(\frac{1-Y_\infty}{1-Y_0}\right) \tag{5.3}$$

Expressing *m* in terms of *r* yields

$$\frac{dr}{dt}=\frac{1}{2r}\left[\frac{M\rho}{\overline{M}\rho_l}DSh\ln\left(\frac{1-Y_\infty}{1-Y_0}\right)\right] \tag{5.4}$$

The Sherwood number, *Sh*, is given by the Ranz-Marshall correlation (equation (4.25)). The Sherwood number and the mass fractions Y_∞ and Y_0 vary with time. However, if suitable average values are taken for *Sh*, Y_∞ and Y_0, the slightly varying bracketed quantity in equation (5.4) can be set equal to a constant. In this manner a simple expression can be obtained for the variation of droplet radius with time. Thus, defining a parameter, λ

$$\lambda=\frac{1}{2}\left[\frac{M\rho}{\overline{M}\rho_l}DSh\ln\left(\frac{1-Y_\infty}{1-Y_0}\right)\right] \tag{5.5}$$

Equation (5.4) now assumes the form

$$\frac{dr}{dt}=\frac{\lambda}{r} \tag{5.6}$$

Integrating this equation and using the boundary condition at $t=0,\quad r=r_0$ yields

$$r^2 = r_0^{\,2} + 2\lambda t \tag{5.7}$$

Substituting equation (5.7) into equation (5.2) yields

$$\frac{d^2 p}{dt^2} + \frac{1}{r^2}\left(3\lambda + \frac{9\mu}{2\rho_l}\right)\frac{dp}{dt} = \left(1 - \frac{\rho}{\rho_l}\right)g \tag{5.8}$$

In this equation the quantities in the parentheses are constants and can be defined by the parameters α and β as

$$\alpha = \left(3\lambda + \frac{9\mu}{2\rho_l}\right) \tag{5.9}$$

and

$$\beta = \left(1 - \frac{\rho}{\rho_l}\right)g \tag{5.10}$$

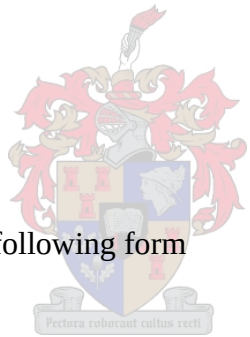

Equation (5.8) now assumes the following form

$$\frac{d^2 p}{dt^2} + \frac{\alpha}{r_0^{\,2} + 2\lambda t}\frac{dp}{dt} = \beta \tag{5.11}$$

This equation is a second order linear differential equation with variable coefficients. It has the following solution

$$p = A(r_0^{\,2} + 2\lambda t)^{(1-\alpha/2\lambda)} + B + \frac{\beta(r_0^{\,2} + 2\lambda t)^2}{4\lambda(\alpha + 2\lambda)} \tag{5.12}$$

Evaluating the integration constants A and B with the following two boundary conditions: at $t = 0,\ p = 0$ and $\frac{dp}{dt} = v_t$ yields

$$A = \left[\frac{\beta {r_0}^2}{\alpha + 2\lambda} - v_t \right] \frac{{r_0}^{\alpha/\lambda}}{(\alpha - 2\lambda)} \tag{5.13}$$

$$B = -{r_0}^2 \left[\frac{\beta {r_0}^2}{\left(\alpha^2 + 4\lambda^2\right)} - \frac{v_t}{\left(\alpha - 2\lambda\right)} + \frac{\beta {r_0}^2}{4\lambda\left(\alpha + 2\lambda\right)} \right] \tag{5.14}$$

Having evaluated the constants *A* and *B* it is now possible to determine the penetration of the water droplet into the boundary layer with equation (5.12). Bhatti and Savery (1975) suggested that the contribution of the first term on the right-hand side of equation (5.12), $A({r_0}^2 + 2\lambda t)^{(1-\alpha/2\lambda)}$, is negligible. They argued that because λ is numerically small and negative, it renders *A* vanishingly small. This is however not the case. Because λ is numerically small and negative, it results in A becoming extremely large (in the range of $1 \cdot 10^{251}$). The $({r_0}^2 + 2\lambda t)^{(1-\alpha/2\lambda)}$ part of the term, however, becomes extremely small (in the range of $1 \cdot 10^{-256}$). The resultant product has indeed an influence on the equation.

By substituting the constants *A* and *B* back into equation (5.12), we now have an equation for the penetration of the droplet into the boundary layer at any time. By recalling that $y = \delta - p$, an equation can now be found for the transverse location of the droplet at any time

$$y = \delta - A({r_0}^2 + 2\lambda t)^{(1-\alpha/2\lambda)} + C - \frac{\beta({r_0}^2 + 2\lambda t)^2}{4\lambda(\alpha + 2\lambda)} \tag{5.15}$$

where

$$C = {r_0}^2 \left[\frac{\beta {r_0}^2 - 4\lambda v_t}{4\lambda\left(\alpha - 2\lambda\right)} \right] \tag{5.16}$$

5.3 Flow direction equation of motion

In 1908 Blasius (White, 1994) found a solution for the velocity profile in the boundary layer for laminar flow. However, accurate solutions for the Blasius equation have only been obtained by numerical integration. For the sake of mathematical simplicity, it was decided that a linear velocity profile in the boundary layer would be an adequate approximation

$$\frac{dx}{dt} = u_\infty \left(\frac{y}{\delta} \right) \tag{5.17}$$

The boundary layer thickness at any point along a flat plate is given by the equation by Blasius (White, 1994)

$$\delta = 5\left(\frac{\nu x}{u_\infty} \right)^{1/2} \tag{5.18}$$

Substituting equations (5.15) and (5.18) into equation (5.17), rearranging and inverting, yields an equation for the change in droplet exposure time with changing longitudinal position

$$\frac{dt}{dx} = \frac{5\nu^{1/2} x^{1/2}}{u_\infty^{3/2}\left[5\left(\frac{\nu}{u_\infty} \right)^{1/2} x^{1/2} - A\left(r_0^{\,2} + 2\lambda t \right)^{\left(1-\frac{\alpha}{2\lambda}\right)} + C - \frac{\beta\left(r_0^{\,2} + 2\lambda t \right)^2}{4\lambda(\alpha + 2\lambda)} \right]} \tag{5.19}$$

This differential equation can be solved using Euler's method or a Runge-Kutta method (Turner, 2000).

5.4 Heat transfer coefficient enhancement

A simple two-region model is developed for determining the heat transfer coefficient in the presence of droplets that penetrate and vaporize within the boundary layer. In

the outer region, the heat transfer occurs by convection as well as by the vaporization of the droplets. In the inner region, where no droplets occur, the heat transfer occurs by convection only. The boundary between the two regions is determined by the depth of penetration of the droplets into the boundary layer. This depth of penetration is given by equation (5.12). The total resistance of the boundary layer can be divided into three resistances as shown in figure 5.2.

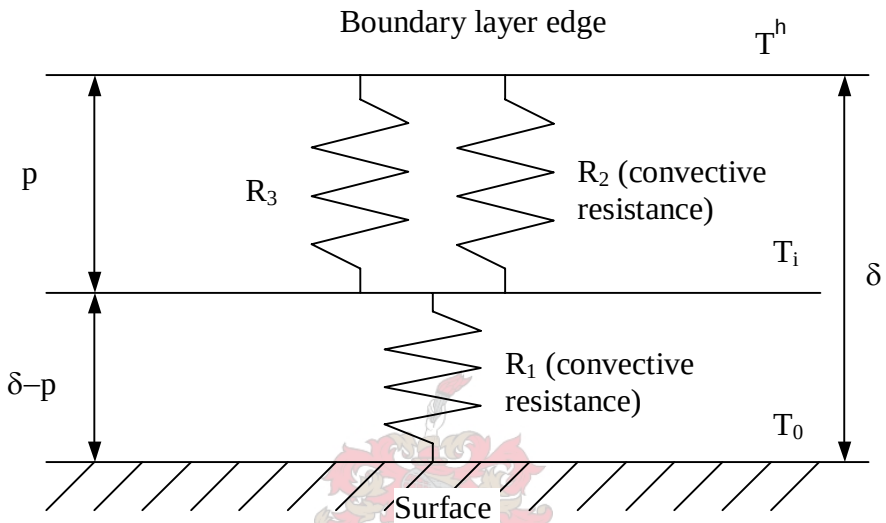

Figure 5.2 Schematic of the thermal resistance of a boundary layer

R_1 and R_2 are convective resistances and by analogy with Ohm's law, they can be written as

$$R_1 = \frac{1}{\bar{h}bl}\left(\frac{\delta - p}{\delta}\right) \tag{5.20}$$

$$R_2 = \frac{1}{\bar{h}bl}\left(\frac{p}{\delta}\right) \tag{5.21}$$

R_3 is a resistance caused by the vaporization of the droplets, and can be determined in the following manner. Assuming the free stream turbulence to be isotropic, if a cube in space is observed, equal masses of droplets will flow through each side of the cube. The cube has 6 sides; therefore 1/6 of the mass of the droplets in the air stream will

flow through the side of the cube directed at the flat surface. Following this reasoning, it is assumed that 1/6 of the mass of the droplets in the air stream is directed towards the surface of the plate. Taking into account that the decrease in the mass of the droplet due to vaporization is Δm, the heat flux generated by the evaporating droplets can be written as

$$\dot{q}_3 = \left(\frac{1}{6}\right)\left(\frac{\Delta m}{m}\right)\dot{m}''bsh_{fg} \tag{5.22}$$

However, if the analogy with Ohm's law is to be maintained, this heat flux has to be written in the following form

$$\dot{q}_3 = \frac{\left(T_i - T_\infty\right)}{R_3} \tag{5.23}$$

R_3 therefore has to be chosen to ensure that this equation is consistent with equation (5.22). Setting equation (5.23) equal to equation (5.22), R_3 can be found as

$$R_3 = K\left(T_i - T_\infty\right) \tag{5.24}$$

where

$$K = \frac{6m}{\Delta m \cdot \dot{m}''sbh_{fg}} \tag{5.25}$$

For the determination of R_3, the value of the interface temperature, T_i, must be known. This can be determined by considering heat flux for the steady-state condition in the boundary layer

$$\dot{q} = h_1\left(T_i - T_\infty\right) = h_2\left(T_0 - T_i\right) \tag{5.26}$$

The conductance h_1 of the outer region, and h_2 of the inner region of the boundary layer can be given by

$$h_1 = \frac{R_2 + R_3}{R_2 R_3 bl} \qquad \text{and} \qquad h_2 = \frac{1}{R_1 bl}$$

Introducing these into the steady state condition and solving for T_i yields

$$T_i = \frac{K\left(R_1 T_\infty + R_2 T_0\right) - R_1 R_2}{K\left(R_1 + R_2\right)} \tag{5.27}$$

Knowing the resistances R_1, R_2 and R_3 from equations (5.20), (5.21) and (5.24), the total equivalent resistance of the boundary layer, R_{eq}, can be determined

$$R_{eq} = \frac{R_1 R_2 + R_2 R_3 + R_1 R_3}{R_2 + R_3} \tag{5.28}$$

An expression for the heat flow from the boundary layer can now be found

$$\dot{q} = \frac{\left(T_0 - T_\infty\right)}{R_{eq}} \tag{5.29}$$

The total area of the flat surface being bl, the expression for the heat flux from the solid surface is

$$\dot{q}'' = \frac{\left(T_0 - T_\infty\right)}{R_{eq} bl} \tag{5.30}$$

Therefore the heat transfer coefficient with droplets present in the boundary layer is

$$h = \frac{\dot{q}''}{\left(T_0 - T_\infty\right)} = \frac{1}{R_{eq} bl} \tag{5.31}$$

The average heat transfer coefficient for laminar flow, in the absence of droplets, can be found with the Pohlhausen relation (Kays, 1966)

$$Nu = \frac{\bar{h}\,l}{k} = 0.664\,\mathrm{Re}^{1/2}\,\mathrm{Pr}^{1/3} \tag{5.32}$$

with Re based on u_∞ and l. The ratio $\frac{h}{\bar{h}}$ gives the enhancement in heat transfer coefficient due to the vaporization of the droplets.

5.5 Results of mathematical model

The use of the equations derived in the preceding section can be illustrated by applying them to the finned surface of an air-cooled heat exchanger. The typical test conditions existing in an experimental set-up at the Stellenbosch University were used to perform the calculations. These conditions together with a sample calculation showing the application of the equations derived above can be found in Appendix B. Is was desired that the entry point of the droplet should be as near as possible to the leading edge of the plate. The value for the entry point, $\xi = 0.0005$ m, was selected.

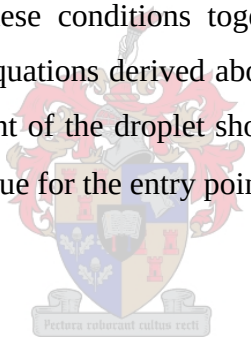

Droplet trajectory

In order to predict the trajectory of a droplet in a laminar boundary layer formed around a flat plat, the equations derived in the preceding section are solved in the following manner. The constants λ, α and β are solved using equations (5.5), (5.9) and (5.10) respectively, and making use of the given initial conditions. The boundary layer thickness at the point where the droplet enters the boundary layer, δ_i, is calculated using equation (5.18). The constants A and B can now be determined using (5.13) and (5.14) respectively.

At this point the Euler method is started. An initial value for x (distance along the plate) is chosen. An increment Δx is chosen and used to determine the value of the time, t, at that increment. The radius of the droplet will decrease with time as a result of evaporation. Making use of equation (5.7), the radius, r, of the droplet at this increment can be calculated. The incremental boundary layer thickness, δ_x, is

calculated using equation (5.18) and the penetration, p, is calculated using equation (5.12). By taking the difference between the boundary layer thickness and the penetration, the y-coordinate of the droplet can be found. In this way both the x and y-coordinate of the droplet is known for each increment.

Figure 5.3 shows the trajectory of droplets of 10 μm, 30 μm and 50 μm diameter in a laminar boundary layer on a flat plate. All the droplets enter the boundary layer at the same point: ξ = 0.01 m. From the figure it can be seen that for the 50 μm diameter droplet, the gravitational force dominates the buoyancy force. The droplet follows a trajectory that impacts the surface. The 30 μm diameter droplet curves towards the surface, but as the droplet becomes smaller, due to evaporation of the liquid, the buoyancy force becomes dominant, forcing the droplet upwards. The droplet evaporates before it has reached the surface. For the 10 μm diameter droplet the buoyancy and drag forces balance the gravitational force and it travels on a straight path. Because of the small size of the droplet, it evaporates rapidly.

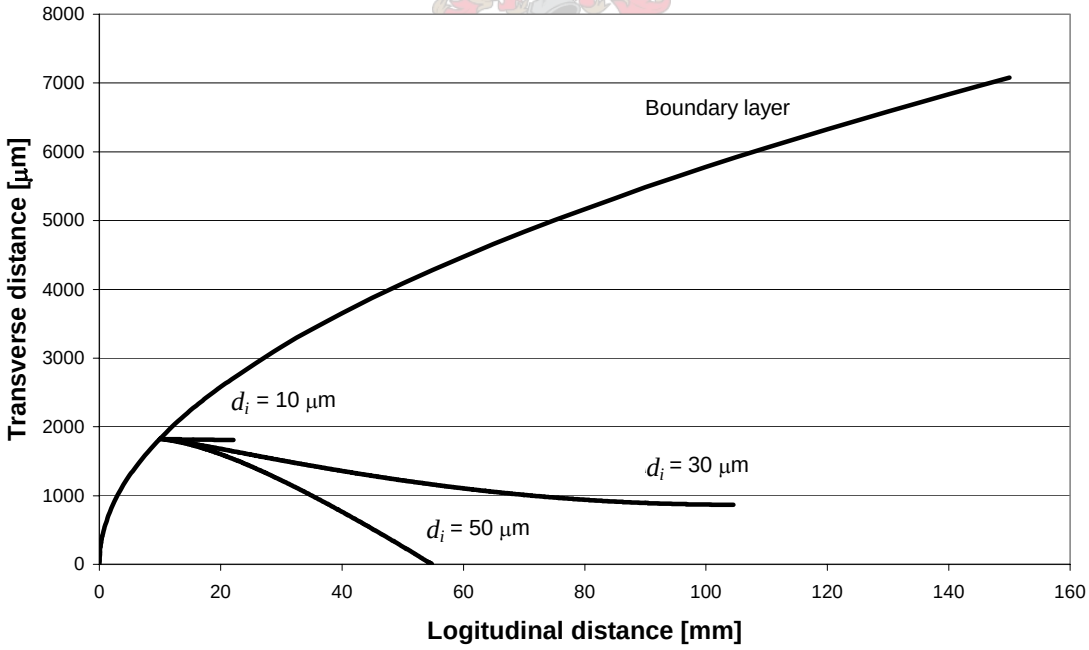

Figure 5.3 Trajectories of different sized droplets entering a boundary layer on a horizontal plate

Figure 5.4 shows the trajectories of a 40 micron diameter droplet entering the boundary layer at different points. It is apparent that as the entry point moves farther from the leading edge into the thicker part of the boundary layer, the droplet experiences more evaporation. As the droplet becomes smaller, the buoyancy and drag forces become dominant over the gravitational force. At the entry point ξ = 30 mm, the droplet doesn't impact the surface.

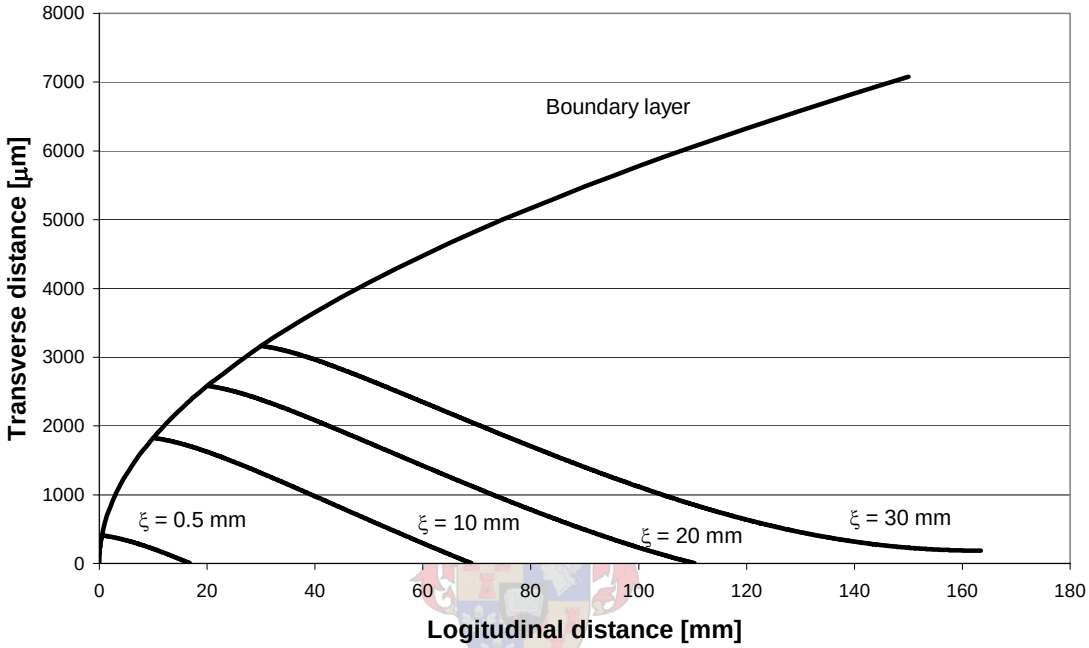

Figure 5.4 Trajectories of 40 micron droplets entering a boundary layer on a horizontal plate

It was found that droplets entering the boundary layer formed on the bottom of the plate follow the same trajectories as the droplets entering the top boundary layer. None of the droplets entering the bottom boundary layer will therefore impact the surface of the plate. These predictions are confirmed by experiments preformed by Bhatti and Savery (1975).

Heat transfer calculations

Making use of the *x*-coordinate of the point where the droplet has been completely vaporized, the boundary layer thickness, δ_x, at this point can be calculated with

equation (5.18). With knowledge of the boundary layer thickness, δ_x, and the penetration, p, at the point of vaporization, the resistances R_1 and R_2 can readily be calculated from equations (5.20) and (5.21). In the case where the droplet hasn't been completely vaporized in the boundary layer, the final droplet diameter can be determined with equation (5.7), and thus the mass differential, Δm, can be calculated. In the case where the droplet is completely vaporized in the boundary layer, Δm is simply the total mass of the droplet. With knowledge of Δm, equation (5.25) can be used to determine the coefficient K. The temperature, T_i, of the interface between the two regions can be determined with equation (5.27). Finally, making use of the coefficient K the resistance R_3 can be determined with equation (5.24). Having now determined the resistances R_1, R_2 and R_3, the equivalent resistance, R_{eq}, can be determined with equation (5.28). Making use of the equivalent resistance, R_{eq}, the heat flux, $\dot{q}''$, can be determined with equation (5.30) and the heat transfer coefficient, h, can be determined with equation (5.31). The heat transfer coefficient in the absence of droplets, $\bar{h}$, can be found with the Pohlhausen relation, equation (5.32). The ratio $\frac{h}{\bar{h}}$ gives the enhancement in heat transfer coefficient due to the vaporization of the droplets.

Figure 5.5 shows the calculations described above performed for different droplet diameters and droplet mass fluxes. It can be seen that for constant droplet mass fluxes, the larger diameter droplets cause greater enhancement in the heat transfer coefficient. This greater enhancement is due to greater evaporation rates, which result from increased exposure time and penetration of the larger-sized droplets. Figure 5.4 also shows that as the droplet mass flux in the main stream increases, the enhancement for the same diameter droplet also increases. This is to be expected, since the increase in droplet flux implies that a greater number of droplets are available for evaporation. For the largest mass flux, $\dot{m}'' = 0.04069\ kg/m^2 s$, and a droplet diameter of 45 μm, a heat transfer enhancement of 77% is achieved. This constitutes a major improvement in heat transfer, and although this mathematical model is only representative of the idealized case, if anything close to this improvement could be achieved in practice this would have major benefits.

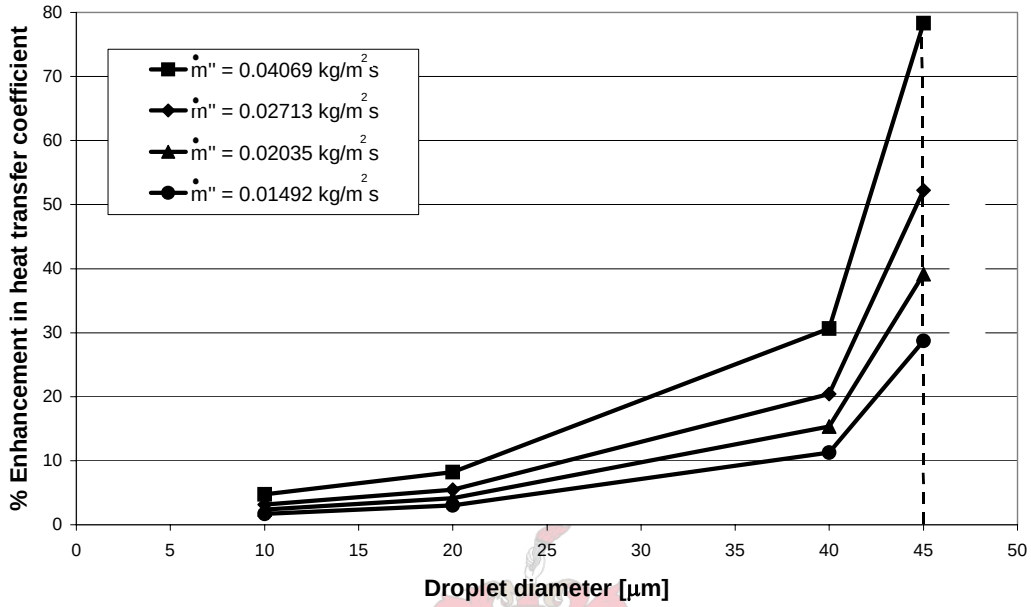

Figure 5.5 Dependence of the heat transfer on the droplet diameter and mass flux

5.6 Discussion and conclusion

The task of verifying the mathematical model derived in this chapter is a daunting one. Because of the small size of the droplets involved and the minute thickness of the boundary layer, accurate measurements become very difficult. One possible method of achieving this is by making use of a high-speed high-resolution camera.

6 Droplet evaporation and heat transfer augmentation in a boundary layer – vertical plate

This chapter describes the mathematical model derived for predicting the behavior of a liquid droplet in a laminar gas boundary layer on a vertical flat plate. This model is compared with the model derived for the horizontal plate setup.

6.1 Introduction

The equations of motion are derived for liquid droplets penetrating the hydrodynamic gas boundary layer on a vertical flat surface and vaporizing therein. For the vertical plate case, a significant force acting on the droplet in the horizontal plane is the force acting on the droplet due to rotation of the droplet.

6.2 Transverse direction equation of motion

The rotation of the droplet is caused by the velocity profile in the boundary layer, resulting in the droplet experiencing a higher air velocity at its top than at its bottom, as shown in figure 6.1.

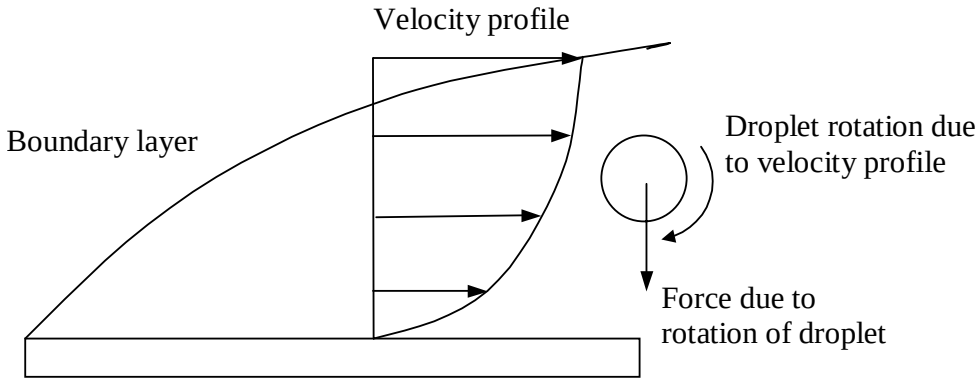

Figure 6.1 Schematic of the rotation of a droplet in a boundary layer cause by the velocity profile

The magnitude of this force can be found by applying potential flow theory to a rotating droplet. The pressure distribution on a rotating cylinder can by given as (Houghton, 1993)

$$p - p_0 = \frac{1}{2}\rho U^2 \left[1 - \left(2\sin\theta + \frac{K}{2\pi u r}\right)\right] \tag{6.1}$$

with K defined as the vortex strength

$$K = q_t 2\pi r \tag{6.2}$$

A spherical droplet can be approximated as being made up of a large number of cylinders of varying diameter. Figure 6.2 shows one such a cylinder.

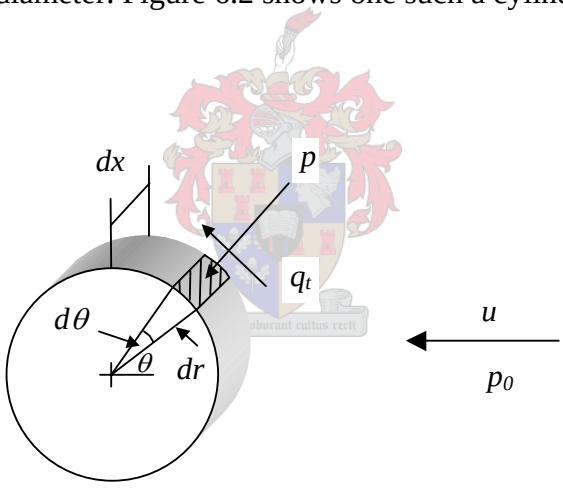

Figure 6.2 Pressure and velocity on the surface of a unit length of a cylinder

The hatched area on the cylinder is the incremental area, *da*, and can be expressed as

$$da = d\theta \cdot dr \cdot dx \tag{6.3}$$

The resultant force on the cylinder therefore is

$$F_R = (p - p_0)d\theta \cdot dr \cdot dx \tag{6.4}$$

and the resultant vertical force is

$$F_V = (p - p_0)d\theta \cdot dr \cdot dx \sin\theta \tag{6.5}$$

Substituting equation (6.1) into equation (6.5) with $B = K / 2\pi ur$ and integrating over the entire diameter of the sphere yields an equation for the vertical force on the droplet (F_V positive upwards)

$$F_V = -2\left[\int_0^r \int_0^r \int_0^{2\pi} \frac{1}{2}\rho u^2 \left[1 - (2\sin\theta + B)^2\right] \sin\theta \, d\theta \cdot dr \cdot dx\right] \tag{6.6}$$

The first integral becomes

$$\int_0^{2\pi} \frac{1}{2}\rho u^2 \left[\sin\theta(1 - B^2) - 4B\sin^2\theta - 4\sin^3\theta\right] d\theta \tag{6.7}$$

which simplifies to $4B\pi$ upon integration. Completing the integration of equation (6.7) yields

$$F_V = 2\rho u^2 r^3 B\pi \tag{6.8}$$

Substituting the definitions of *B* and *K* into equation (6.8) yields an equation for the force on a droplet due to the rotation thereof

$$F_V = 2\rho u q_t r^3 \pi \tag{6.9}$$

As in the horizontal flat plate model, free stream turbulence superimposed on the boundary layer is assumed to cause the initial transverse velocity component that propels the droplets towards the solid surface. The transverse and flow direction equations of motion are again solved simultaneously to obtain an expression for the exposure time of the droplets in the boundary layer. The same assumptions made for

the flat plate model are applicable to this model, with the addition of the following assumptions:

- The tangential velocity of the droplet is equal to the difference in air velocity it experiences at the top and bottom of the droplet.
- The force on the droplet due to the rotation of the droplet is calculated using the boundary layer velocity at the point of droplet entry.

Consider a water droplet entering a boundary layer formed on a vertical plate. The top view of this is shown schematically in figure 6.3. The gravity and buoyancy forces that acted on the droplet in the horizontal plate case are now absent. The forces acting on the droplet in the transverse direction consist of a force due to the rotation of the droplet and a drag force.

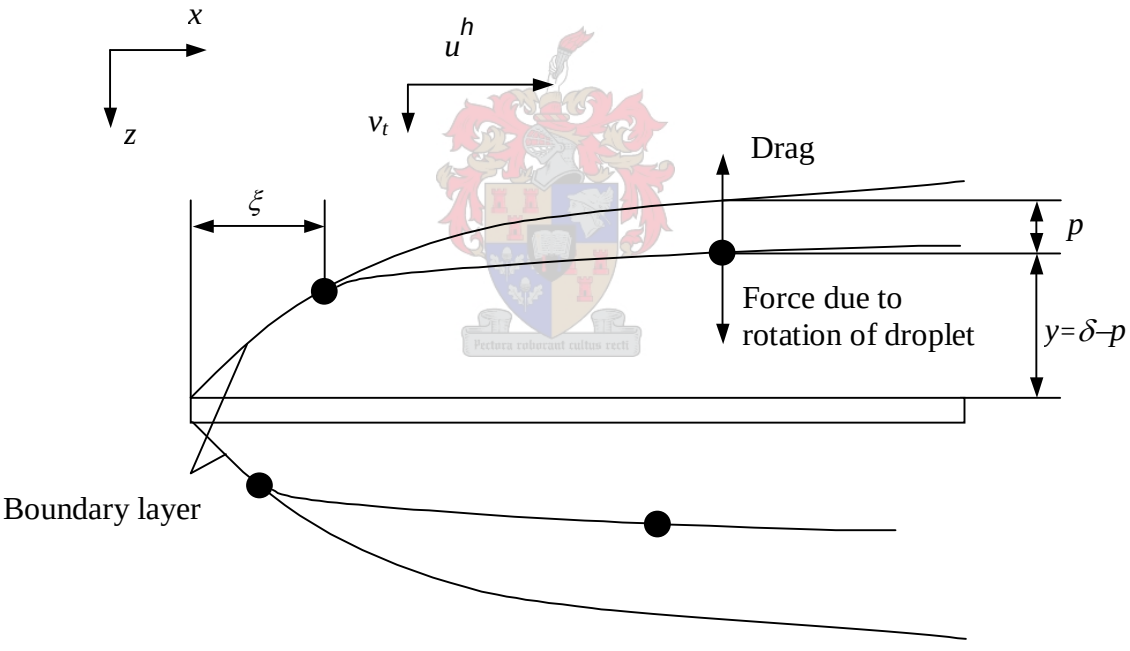

Figure 6.3 Schematic of a liquid droplet in a gas boundary layer formed on a vertical plate

According to Newton's second law of motion

$$\frac{d}{dt}\left(m\frac{dp}{dt}\right) = 2\rho u_{bl} q_t r^3 \pi - 6\pi\mu r \frac{dp}{dt} \tag{6.10}$$

Expressing m in terms of r, simplifying and rearranging yields

$$\frac{d^2p}{dt^2}+\left(\frac{3}{r}\frac{dr}{dt}+\frac{9\mu}{2\rho_l r^2}\right)\frac{dp}{dt}=\frac{3u_{bl}q_t}{2} \tag{6.11}$$

This equation has the same form as equation (5.11), except that the parameter β is now defined as

$$\beta=\frac{3u_{bl}q_t}{2} \tag{6.12}$$

The same procedure that was followed for the horizontal plate model is now followed for the vertical plate model to determine the trajectories of droplets in the boundary layer.

The heat transfer calculations are identical to the horizontal plate model and will not be repeated for this model.

6.3 Results of mathematical model

The use of the equations derived in the preceding section can be illustrated by applying them to the finned surface of an air-cooled heat exchanger. The same conditions that were used for the horizontal plate model were used to perform the calculations for the vertical plate model.

Calculations were first performed to determine the trajectories of droplets of the same size (30 micron) entering the boundary layer formed on a vertical plate at different longitudinal distances on the plate. The results of the calculations are shown in figure 6.4. The graph shows the trajectories of the droplets as well as the point where the droplets have been completely vaporized. It can be seen that the force due to the rotation of the droplets and the drag force, both being relatively small forces, have only a small effect on the droplets. As the droplets enter the boundary layer, they start to spin in a clockwise direction (relative to the graph shown) as a result of the velocity

profile. This results in a downward force on the droplets, forcing them towards the surface.

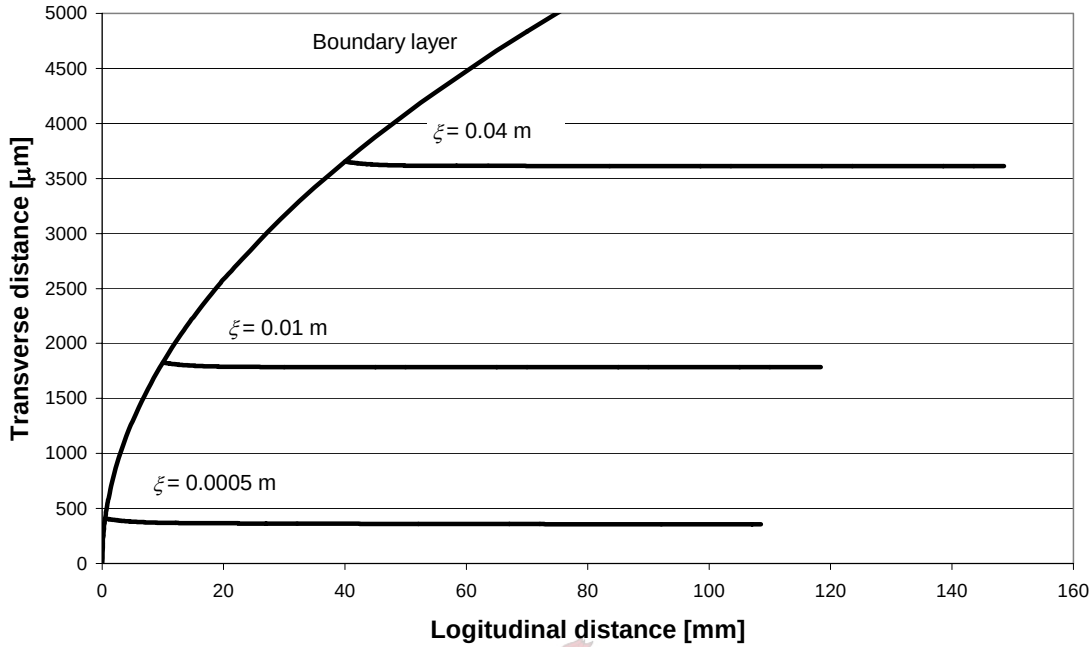

Figure 6.4 Trajectories of liquid droplets entering a boundary layer on a vertical plate at different longitudinal distances

Once the droplets start to move, a drag force is exercised in the upward direction, resulting in smaller resultant force acting towards the surface. The droplet then moves toward the surface at a very slow rate, and is vaporized before it has impacted the surface. This will be the case for all droplets except those that enter extremely near to the leading edge of the plate.

Calculations were also performed for droplets of different diameter entering the boundary layer at the same point (ξ = 0.01 m). The results of these calculations are shown in figure 6.5.

This graph shows that the as the droplet becomes larger, it experiences a bigger force towards the surface. A possible explanation for the phenomenon is that the larger droplets experience a higher rate of rotation and therefore a larger downward force.

This higher rate of rotation is as a result of the bigger difference in velocities that the droplet experiences at its top and bottom.

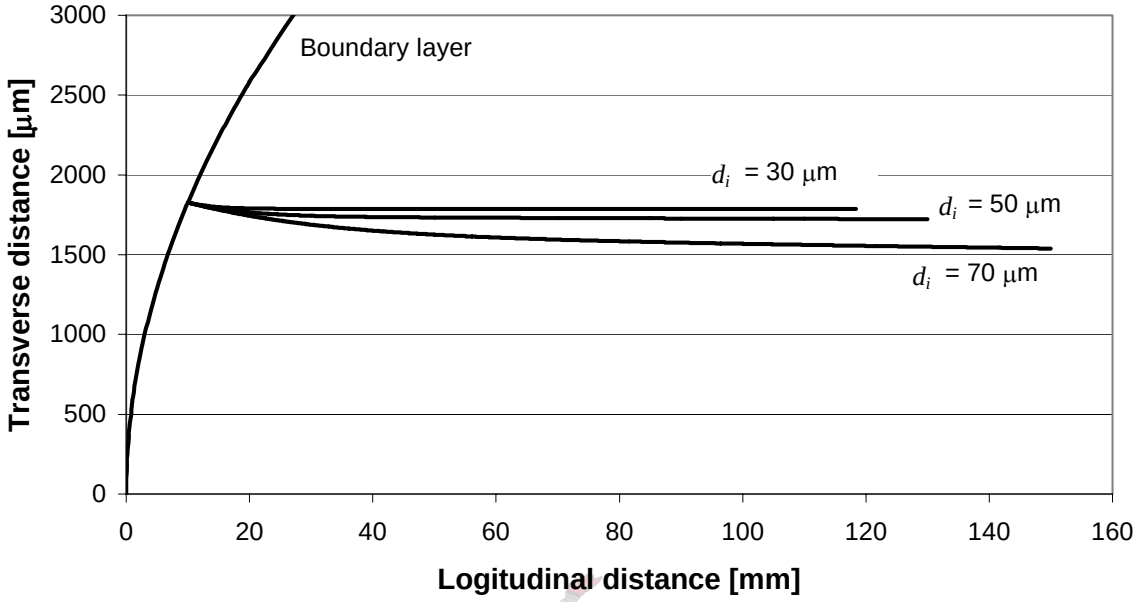

Figure 6.5 Trajectories of different sized liquid droplets entering a boundary layer on a vertical plate at the same point

6.4 Discussion and conclusion

Comparing the droplet trajectories of the horizontal plate model with the vertical plate model, it can be seen that for the case where the fins of a heat exchanger is vertical, the droplets experience a reduced force towards the surface. This is due the face that the large influence of gravity that is present in the horizontal plate model is absent in the vertical plate model. This indicates that heat exchangers with vertical fin configurations would experience reduced surface wetting if droplets of sufficiently small size is used to cool the heat exchanger.

The models derived for the evaporation of a droplet in a free stream (chapter 4) and evaporation of a droplets in a hydrodynamic boundary layer (chapters 5 and 6) can be combined to show the behavior of a droplet during its entire lifetime, from the

moment it issues from the nozzle orifice to the moment it has been completely vaporized in a boundary layer formed around a flat plate.

7 Electrostatic spray

This chapter contains an overview of previous work done on the electrostatic charging of droplets, and the most common uses in industry. The design of a capacitive type electrostatic nozzle is described. The system designed to produce the required input signal to the nozzle is also explained.

7.1 Introduction

During the latter part of the 20th century there was a period of rapid development of electrostatics-bases technology for extensive implementation across various industrial, commercial and business sectors. Foremost developments include electrostatic processes for effectively applying liquid and powder coatings to manufactured goods, xerographic copying, precipitation of particulate pollutants from flue gases, manufacture of abrasive papers, ink-jet printing, etc. Considerable advances were also made in development of beneficial applications of electrostatics in agricultural and biological systems.

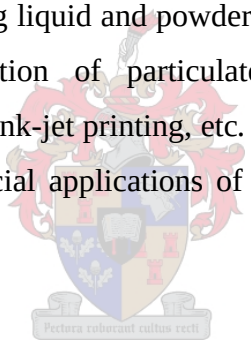

7.2 Electrostatic forces for controlling particulate dynamics

The Lorentz equation quantifies the force F imposed upon a particulate of charge q and velocity v when acted upon by an electric field E and a magnetic field B as

$$F = q(E + vxB) \tag{7.1}$$

For charged bodies being fixed or moving relatively slowly, the electric force component qE dominates over the negligible magnetic component. This provides the basis for various electrostatic processes in which dynamic control of particulate trajectories is achieved for purposes of dispersion, propulsion, attraction, deposition, conveyance, separation, etc. For liquid and solid matter of diameters under several hundred micrometers, common particulate-charging methods - like corona charging

and induction charging - impart charge-to-mass ratios quite adequate to provide electrostatic forces that 10-50 fold dominate over gravity in electric fields well under the 30 kV/cm dielectric strength characteristic of air. Therefore, technological implementation of electrostatic forces for use with charged powder and droplet applications is quite feasible.

7.3 Review of literature

The pioneering work by Lenard (1892) near the close of the 19th century set the stage for the understanding and implementation of the electric charge associated with liquid mists and sprays. He investigated the intense electrification and sparks associated with liquid surface disruptions caused by the bubbling and misting of waterfalls in the Austrian Alps, and named the phenomenon “Wasserfall-Elektrizität”.

Extensive research on the use of electrostatic spray for the use in pesticide-spraying processes has been continued at the University of Georgia by Law and his graduate students (1983). This work provided a successful pneumatic-atomizing, embedded-electrode, electrostatic-induction spray-charging nozzle (Law, 1978).

Law (1987) investigated the maintenance of charge on electrified clouds of airborne spray moving from charging nozzles to grounded-plant targets. Neutralization of the cloud's charge by naturally occurring ambient air ions (1-2 x 10^3 ion pairs/cm^3) is shown not to be a significant charge loss; a moderately charged (e.g. 15 μC/m^3) spray cloud would have to traverse 30 km to encounter an equal charge of air ions. Law and Bowen (1975) theoretically and experimentally investigated the charge-loss phenomena associated with aqueous-based pesticide droplets subject to in-flight evaporation. Mass loss by evaporation was found to convey no appreciable droplet charge. As a result, as surface charge density increases on an evaporating droplet and reaches the critical Rayleigh value for onset of hydrodynamic instability, the droplet ruptures. In this case typically 30% of droplet charge is ejected on 5% of its mass as the surface ruptures. Although the parent droplet experiences a charge loss, the overall spray-cloud charge is conserved, and the greater electrical mobility of sibling droplets offers droplet-trajectory options of possible entomological benefit.

In contrast, airborne pesticide spray clouds can experience considerable charge losses by electrical discharges induced to flow from sharp points and edges of grounded targets under action of the approaching cloud's space-charge field (Law and Bowen, 1975; Law and Lane, 1982). Cooper and Law (1987) have shown positively-charged sprays exacerbate this induced-discharge problem; they thus provided the motivation for selecting negatively charged pesticide sprays for most electrostatic crop spraying applications. Laser Doppler analysis of charged-droplet trajectories in the vicinity of grounded target points by Law and Bailey (1984) at the University of Southampton documented that charge and momentum transferred to the approaching charged-droplet cloud could locally cause velocity reversal and actual droplet repulsion. This droplet repulsion phenomenon might be applied to the problem of preventing water droplets from settling onto the surface of a heat exchanger.

Moon, Lee et al. (2003) studied the problem of improving the deposition efficiency of conventional pesticide spraying nozzles. They found that on conventional electrostatic spraying nozzles using direct current high voltage, a great current leakage was existent as a result of the charged droplets being attracted to and impacting on the high voltage electrode. As a result, the high voltage drops greatly, and the charging performance decreases significantly. One method of overcoming this problem is by making use of near sonic velocity air blasts to prevent the droplets from reaching the induction electrode (Law, 1978), as shown in figure 7.1.

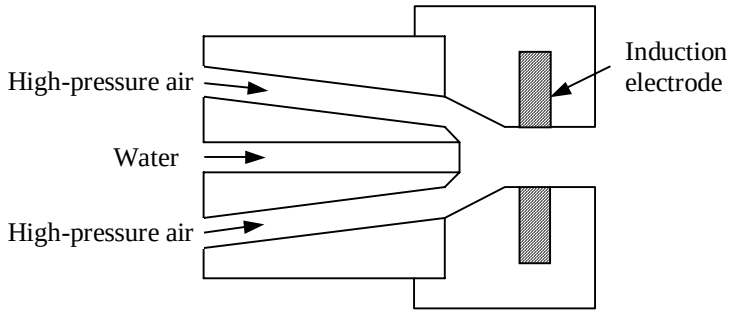

Figure 7.1 Embedded electrode electrostatic spray nozzle with high velocity air shroud

It was found that this nozzle was very efficient in charging water droplets, and that almost no current leakage was evident. However, the nozzle requires a high-pressure compressor to produce the high air velocity and high-pressure piping. The additional cost of the compressor and piping must be considered when choosing this type of nozzle.

Moon, Lee et al. (2003) proposed the use of a capacitive type electrostatic spraying nozzle to overcome the problem of current leakage. This nozzle was chosen to produce the charged spray required for the experiments performed for this thesis. A description of this nozzle is given in section 7.5.

7.4 Electrostatic spray applied to heat exchanger performance improvement

As indicated by the review of literature, the most common application of electrostatic spray is in the agricultural industry where electrostatic spray is used to improve the deposition of pesticides when sprayed on crops. Another common application is the use of electrostatic sprays in the painting industry to improve paint coating.

As stated earlier in the literature review on heat exchanger performance improvement, one of the major concerns of the performance improvement of air cooled heat exchangers with the use of evaporative cooling is the corrosion caused by droplets impacting the heat exchanger and wetting the surface (Woest et al. ,1991; Leidenfrost and Korenic 1982). The concept of preventing the wetting of the heat exchanger by means of electrostatic spray consists of the following. A charge of a certain polarity (either negative or positive) is placed on the droplets of a fine spray by means of an electrostatic charging device. The same charge is placed on an air-cooled heat exchanger. The spray is then directed at the heat exchanger. The forces described by equation (7.1) act on the droplet as it enters the electrical field surrounding the heat exchanger. If the charge on the droplet and the heat exchanger are sufficient, this electrostatic force can be used to repel the droplet when it comes close to the heat exchanger and thus prevents it from impacting the surface of the heat exchanger. In

this way the heat exchanger remains dry. In the literature review it was also apparent that the major area of concern regarding surface wetting when very small droplets are used is the leading edge of the fins of a heat exchanger, where the boundary layer is very thin (Kröger and Branfield, 2003). By either controlling the charge of the droplet or the charge on the heat exchanger, the droplets can be prevented from impacting the leading edge of the fins. In this way they can be made to enter the boundary layer around the surface of the fins, and as a result the heat transfer improvements mentioned in chapter 5 might be exploited. Figure 7.2 shows this process on a heat exchanger fin.

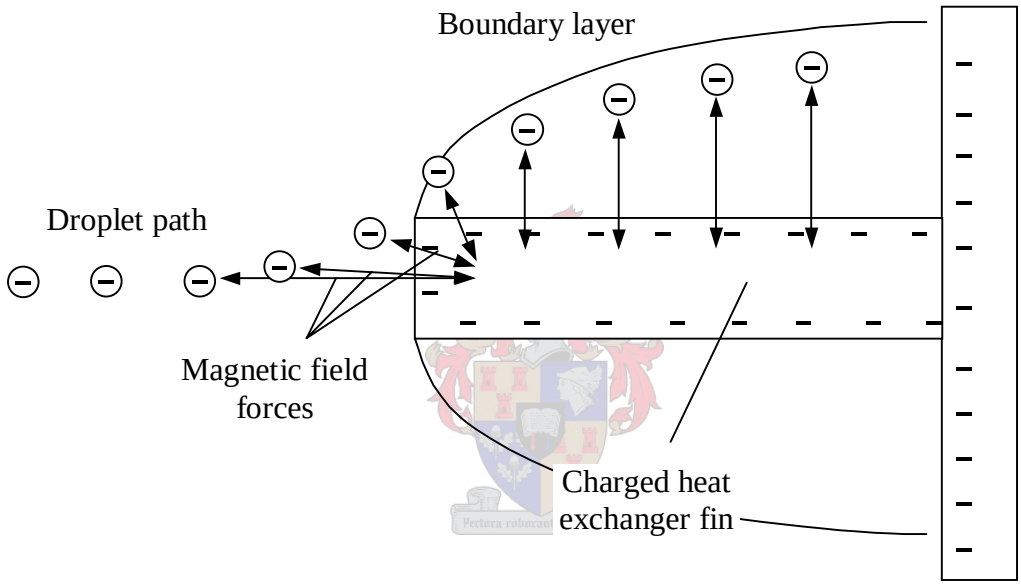

Figure 7.2 Path of charged droplet interacting with charged heat exchanger fin

A theoretical analysis of the interaction of the electric field, aerodynamic delivery and target geometry presents obvious difficulty. As a result of this difficulty, empirical studies should provide the expedient avenue for research.

7.5 Capacitive electrostatic nozzle

A major consideration of a pre-cooling system to be used with an air-cooled heat exchanger is the capital outlay and the operating cost of the system. Because of this it

was felt that the nozzle designed by Law (1978) (shown in figure 7.1), although very effective in charging liquid droplets, might be too expensive. The capacitive type electrostatic nozzle proposed by Moon, Lee et al. (2003) was chosen for the experiments because of its simplicity and affordability.

Conceptual nozzle configuration

Figure 7.3 shows the conceptual equivalent electrical circuit of a capacitive electrostatic spraying nozzle. C_a is the air-gap capacitance between the water film on the inside of the cone and the water column issuing from the orifice. C_t is the capacitance of the insulating layer of the cone between the water film and the ring-type induction electrode. In order to maximize the droplet charging efficiency, most of the voltage has to be applied across C_a, as indicated by

$$V_{ap} = V_a + V_{tr} \cong V_a \tag{7.2}$$

since

$$C_t \rangle\rangle C_a$$

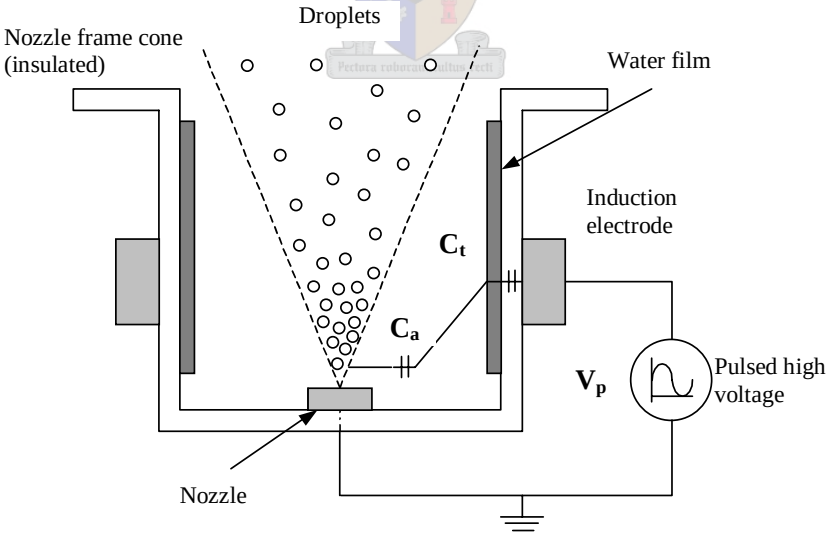

Figure 7.3 Conceptual equivalent circuit of electrostatic spraying nozzle

If a pulsed voltage, $V_{p,}$ is applied on the induction electrode installed on the outside of the insulating layer of the nozzle frame cone, then an induction charge, Q_i, is stored in

the water film formed on the inside wall of the nozzle cone. An induction voltage, V_i, would appear on this water film, on the opposite side of the induction electrode. The induction voltage would in this case be $V_i = \frac{Q_i}{C_a}$, where C_a is the air-gap capacitance between the water film formed on the inside of the nozzle frame cone and the water column issuing from the orifice of the nozzle. The water film becomes, in effect, the induction ring, with the induction voltage, V_i, on it. V_i acts as an applied voltage to the water column issuing from the orifice of the nozzle.

If this applied voltage is made to be only positive, electric charges of negative polarity will be drawn from ground (the water supply is grounded) to the nozzle and the water spraying from the nozzle. As the droplets are formed, the electric charge present on the liquid at that moment will remain on the droplets as they are propelled away from the nozzle.

The advantage of this type of nozzle is that the water film on the inside of the nozzle frame cone becomes the induction electrode, but it isn't directly connected to ground. There can therefore be no current leakage if charged droplets hit the water film. Thus there is no voltage drop, as was the problem with conventional type electrostatic nozzles when the charged droplets impacted the induction electrode.

Geometrical design

Moon, Lee et al. (2003) performed parametric studies of a capacitive nozzle to determine the highest charging performance. They investigated different parameters to determine the configuration required for maximum performance. The configuration tested is shown in figure 7.4.

They found the most important parameters were the induction electrode width, *w*, the distance between the induction electrode and the nozzle, *z*, and the nozzle frame cone diameter, d_i. They determined the following values for these parameters:

w = 4 mm

z = 4 mm

d_i = 25 mm

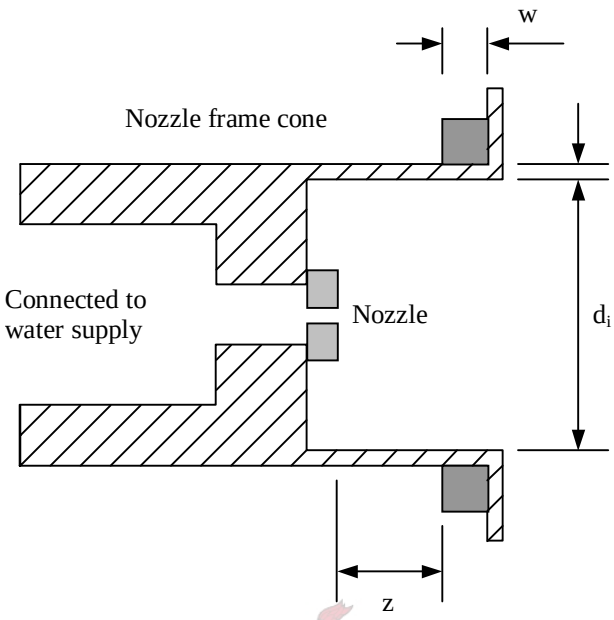

Figure 7.4 Key parameters of capacitive electrostatic spray nozzle

A nozzle frame cone and induction ring were manufactured having these dimensions. A wick was fixed on the inside of the cone opposite the induction electrode to ensure that a proper water film formed on the inside of the cone. The wick remained wet as a result of water droplets from the spay impacting it. A drainage pipe was also included to prevent the water film formed on the inside of the cone from reaching the water issuing from the nozzle orifice and causing a short circuit. The nozzle frame cone was manufactured in such a way as to allow different types of spray nozzles to be attached. The completed configuration is shown in figure 7.5.

The design drawings of the nozzle frame cone and induction ring are given in Appendix D.

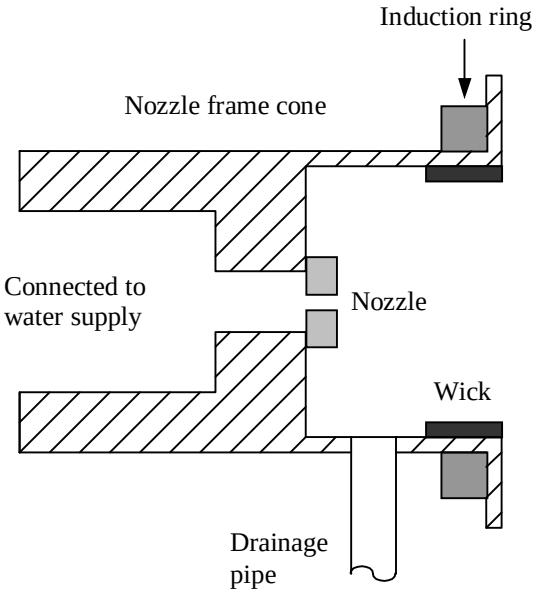

Figure 7.5 Configuration of capacitive electrostatic spray nozzle

Pulsed high voltage signal

As explained in the previous section, the capacitive type electrostatic spraying nozzle requires a pulsed voltage to operate. In addition, this pulsed voltage has to have a positive polarity to produce negatively charged water droplets. For the input wave signal, Moon, Lee et al. (2003) found that optimum droplet charging took place with a positive sinusoidal signal with frequency of 10 kHz. For the experiments performed for this section, a maximum amplitude of 7 kV was used. This sinusoidal waveform is shown in figure 7.6.

The required input signal was achieved making use of a signal generator, an amplifier, a high voltage transformer and a voltage clamp, as shown in figure 7.7. This system is described in detail below.

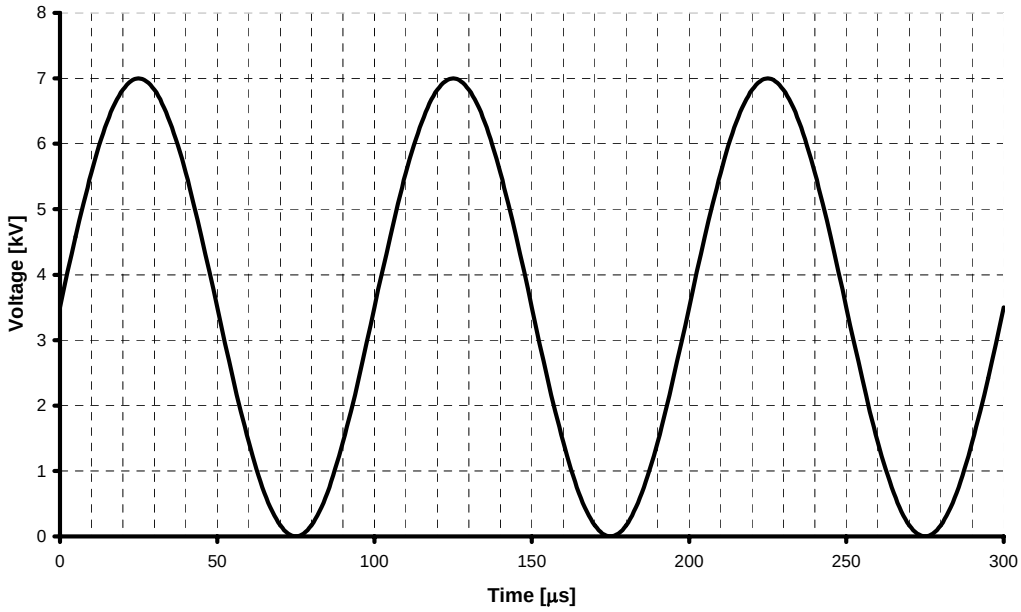

Figure 7.6 Sinusoidal input signal

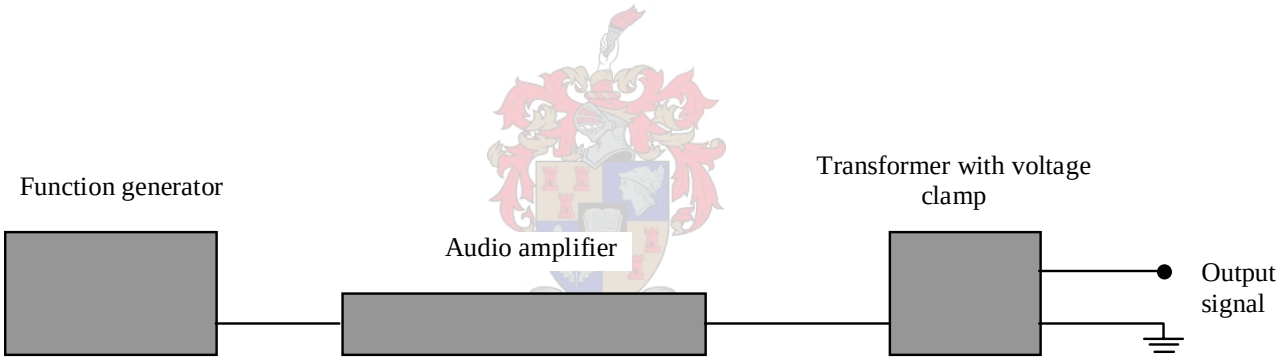

Figure 7.7 Configuration of input signal system

A function generator (Tektronix CFG250) was used to produce the initial sinusoidal signal. This signal had an amplitude of 7 V, and a frequency of 10 kHz. An operational amplifier (FK351) was used to build a non-inverting amplifier to amplify the signal generated by the signal generator. The circuit diagram of the non-inverting amplifier is shown in figure 7.8.

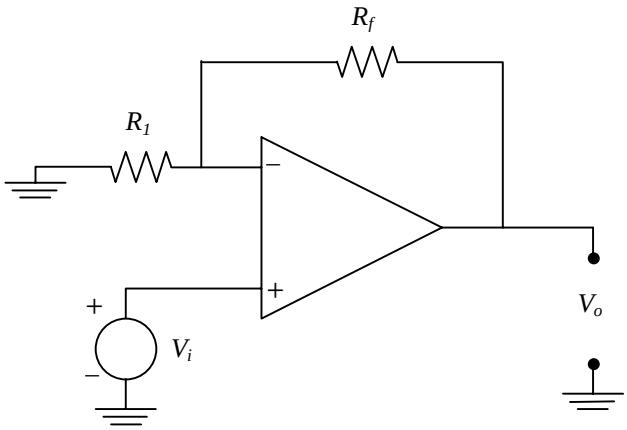

Figure 7.8 Diagram of non-inverting amplifier

An output voltage of 70 V was required. This meant that the voltage gain, A_v, had to be a factor 10. The voltage gain of the amplifier can be found with the following equation:

$$A_v = 1 + \frac{R_f}{R_1} \tag{7.3}$$

By a judicious choice of R_f and R_1, the required voltage gain could be achieved. However, it was found that this particular operational amplifier could not deliver the power required to drive the high voltage transformer. The non-inverting amplifier was therefore replaced by an integrated audio amplifier (Technics SU-V300). This audio amplifier could also produce the required amplification of the signal to 70 V, as well as having enough power to drive the high voltage transformer.

A high voltage transformer was used to increase the signal from 70 V to 7 kV. The required signal (shown in figure 7.6.) had to be kept positive (i.e. it had to have a DC offset to keep it above 0 V.) This could be achieved by making use of a voltage clamp. Because a transformer would remove any DC component of the signal, it was found that the voltage clamp had to be installed downstream of the transformer. The voltage clamp used to clamp the signal above 0 V is shown in figure 7.9. A capacitor, *C*, and diode, *D*, are connected in series with the incoming signal, V_i. The output

signal, V_o, measured over D will be the input signal, V_i, clamped at 0 V. Figure 7.10 shows the high voltage transformer with the voltage clamp.

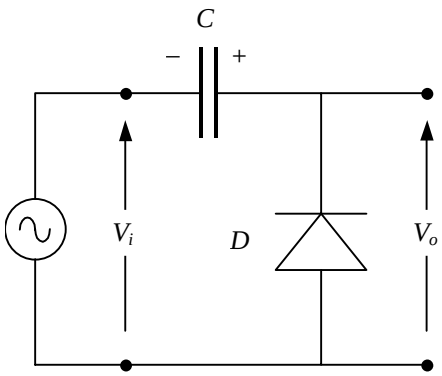

Figure 7.9 Diagram of the voltage clamp

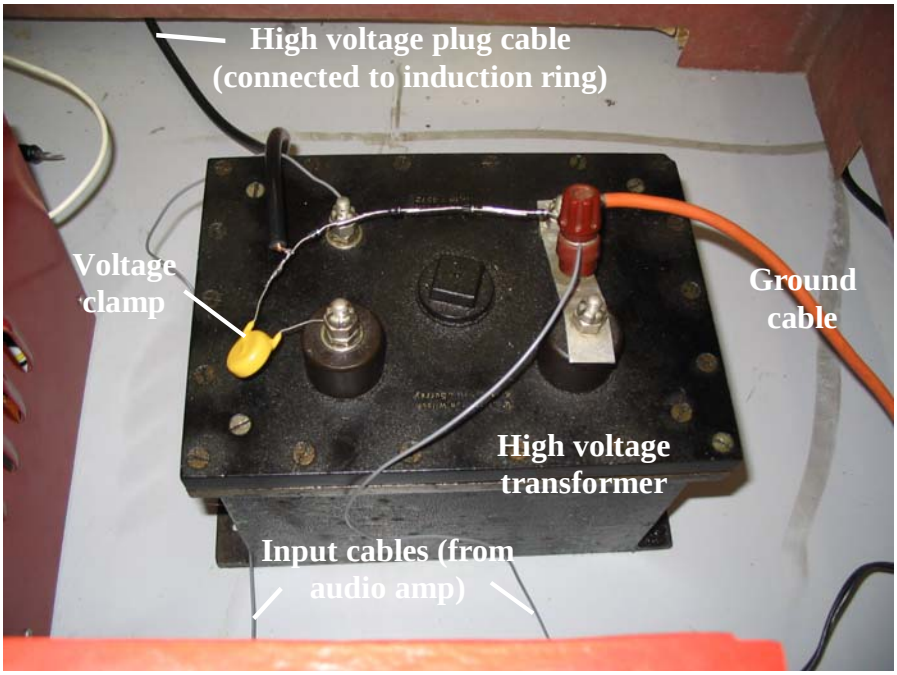

Figure 7.10 High voltage transformer with voltage clamp

The complete setup for the input signal together with the waveform of the signal at different stages in the system is shown in figure 7.11.

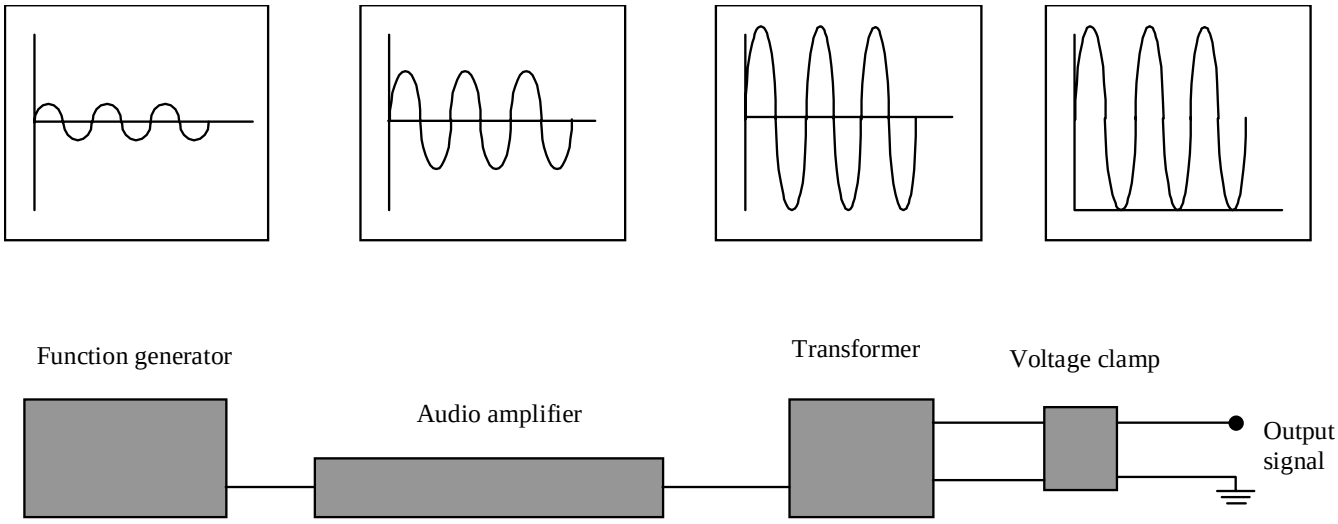

Figure 7.11 Complete input signal system with waveforms

8 Nozzle charging performance experiment

This chapter contains details on the experiments performed to determine the charging performance of the capacitive electrostatic charging nozzle. The results are presented and discussed.

8.1 Introduction

It was desired to determine the charging performance of the proposed capacitive electrostatic nozzle. This could be achieved by spraying the charged spray onto a conductive target plate and measuring the current flowing from the plate to ground.

8.2 Experimental setup

The completed experimental setup is shown schematically in figure 8.1. The capacitive electrostatic nozzle was connected to a high-pressure water pump. A pressure gauge was installed between the pump and the nozzle to measure the nozzle pressure. The pump speed (and therefore the pressure) was controlled using a variable speed drive (Yaskawa Varispeed 616G3). The water pump was connected to the municipal water supply. The municipal water supply was taken to be at zero potential. The input signal system described in the previous chapter was connected to the induction ring on the nozzle frame cone. The input signal was measured using a digital oscilloscope (Tektronix TDS 2014) with a high voltage probe. A target plate was installed downstream of the nozzle. The object of the target plate is to collect all the charged droplets issuing from the nozzle. If the droplets impacting the plate carried a charge, a current would flow from the plate if it were connected to ground. The target plate was insulated from ground using plastic insulators. Because of the dispersion of the smaller droplets, it was found that it would be necessary to make use of an additional target cone to make sure that all the droplets were collected. A 1 MΩ resistor was connected between the target cone and ground. The same was done for the target plate. A digital voltmeter (Fluke 75) was used to measure the voltage drop

over the resistor. Making use of Ohm's law, the current flowing through the resistor could be calculated, and thus the current flowing from the plate could be found. In performing this measurement, the inlet impedance of the digital voltmeter becomes a factor, because of the relatively large resistor that the measurement is taken over. The inlet impedance of the digital voltmeter was found to be 10 MΩ. This resistance in parallel with the 1 MΩ resistor forms a 0.9 MΩ resistor. This decreased overall resistance must be taken into account in calculating the current.

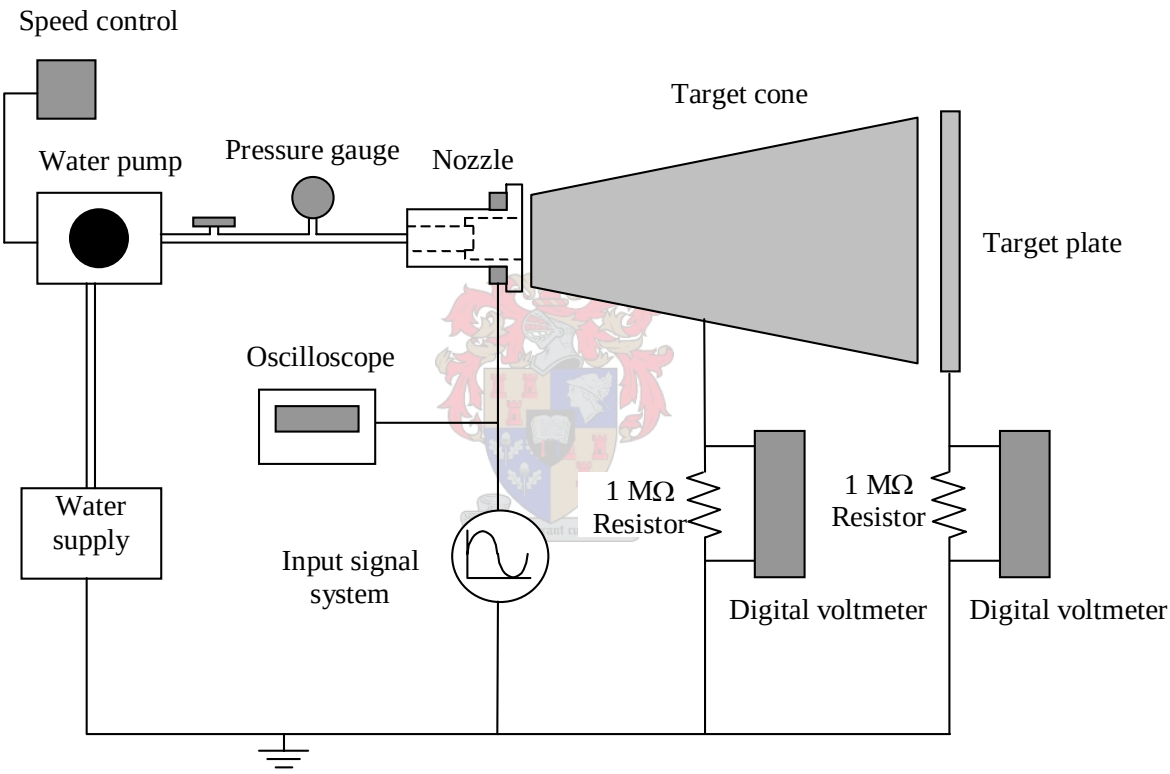

Figure 8.1 Schematic setup of nozzle charging performance experiment

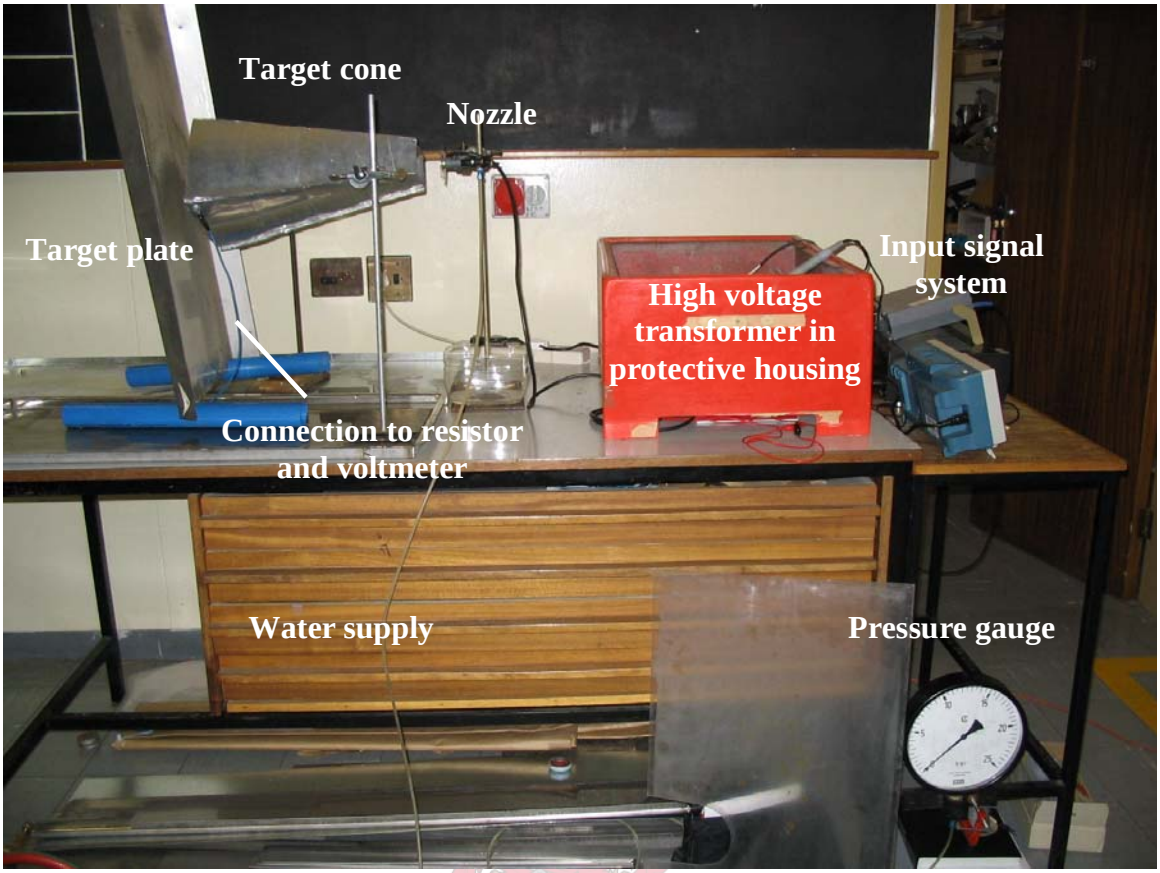

Figure 8.2 Setup of nozzle charging performance experiment

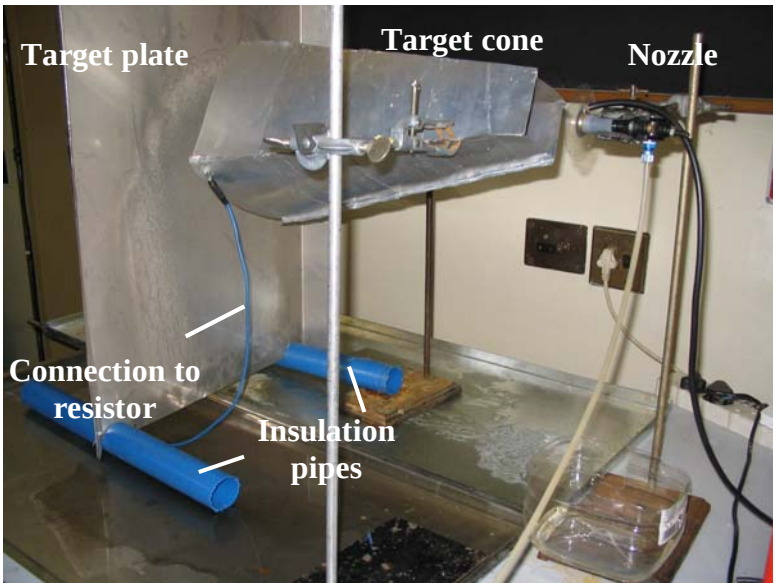

Figure 8.3 Setup of target plate and target cone

8.3 Experimental results

A series of experiments were performed to determine the relation of the input signal voltage to the droplet charge. From preliminary tests it was found that in order to have a measurable current running from the target plates to ground, is was necessary to make use of a nozzle with a relatively large flow rate. A Lurmark HollowTip HCX8 nozzle with a flow rate of 0.0142 kg/s at 800 kPa was used. For each voltage setting from 2 kV to 7 kV a measurement of the voltage drop over the 1 MΩ resistor was taken for both the target plate and target cone. These tests were performed 5 times to ensure consistent and repeatable results. The data obtained from the tests are given in Appendix C. The result of the experiment is given in figure 8.4.

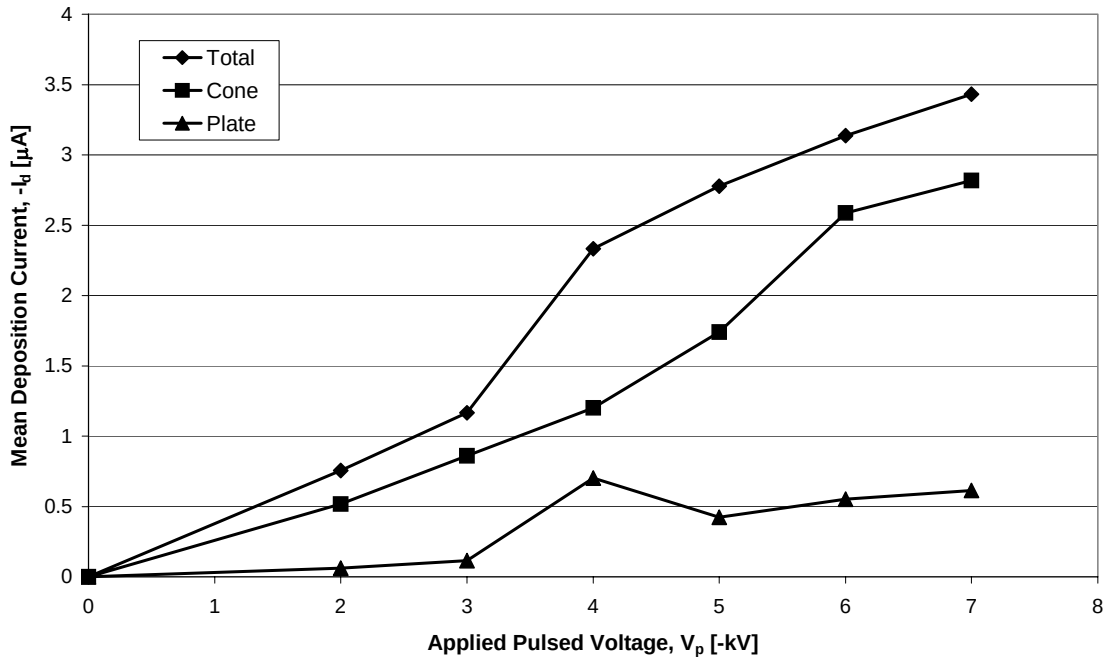

Figure 8.4 Results of nozzle charging performance experiment

From the results it can be seen that the mean deposition current increased as the applied pulsed voltage increased. The mean deposition currents found in these experiments are about 40% of the deposition currents that Moon, Lee et al. (2003) found when they performed similar experiments. Owing to the extreme difficulty in achieving accurate measurements of the deposition current because of the small

currents encountered in the experiments, the differences in the results might be ascribed to inaccuracies in the measurements. It was, however, felt that the deposition current found was adequate for the purpose of this experiment, and that therefore that the capacitive type electrostatic nozzle worked satisfactorily. By making use of the liquid mass flow rate of the nozzle, the charge-to-mass ratio of the spray could be determined

$$CMR = \frac{q}{m} \tag{8.1}$$

By making use of this equation and the mass of a droplet, the charge on droplets of different size could be determined. Figure 8.5 shows the result of such a calculation for an applied voltage of 5 kV peak value. The figure shows an exponential rise in droplet charge as the droplet diameter increases. This is very advantageous, since the larger droplets require a larger force to prevent them from impacting the surface of the heat exchanger. The higher charge on the larger droplets will increase the force applied to them.

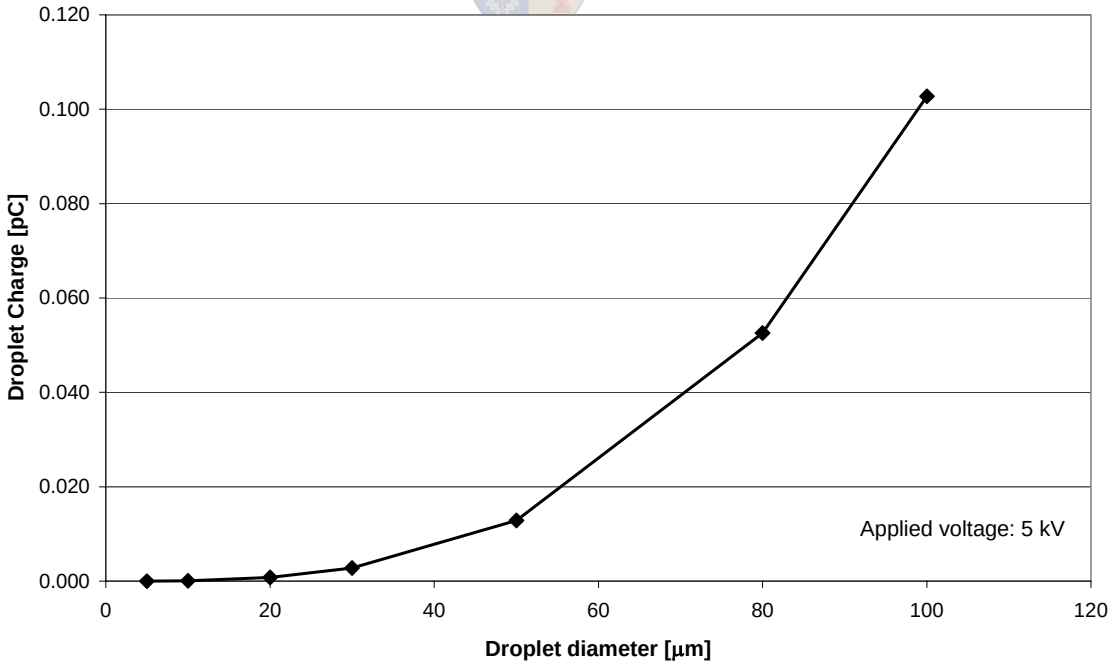

Figure 8.5 Graph of droplet charge for different droplet diameters (5 kV peak applied voltage)

One method of determining the performance of a droplet-charging device is by comparing the imparted charge to the theoretical charge limit. For airborne particles having surface tension values typical of water, this theoretical limit is imposed by hydrodynamic instability and rupture of the surface of the droplets (Law, 1975). As has been shown by Raleigh (1896), for any given liquid a maximum surface charge density exists such that the outward expanding electrical force is just balanced by the constraining force of surface tension. The value of this theoretically defined droplet-charge limit is given as (Hendriks, 1973)

$$q_{\max} = 3.3 \cdot 10^{-4} r^2 \tag{8.2}$$

Peter Castle (1982) conducted experiments on electrostatic spraying of orchards. He found that most electrostatic spraying systems imparted a droplet charge of between 10 and 50% of the theoretical charged limit predicted by equation (8.2). He called this a derating factor. Figure 8.6 shows that the measured experimental values are in the region of 10% of the theoretical limit for droplet in the range of 80 – 100 micron diameter. This system therefore has a derating factor of approximately 0.1.

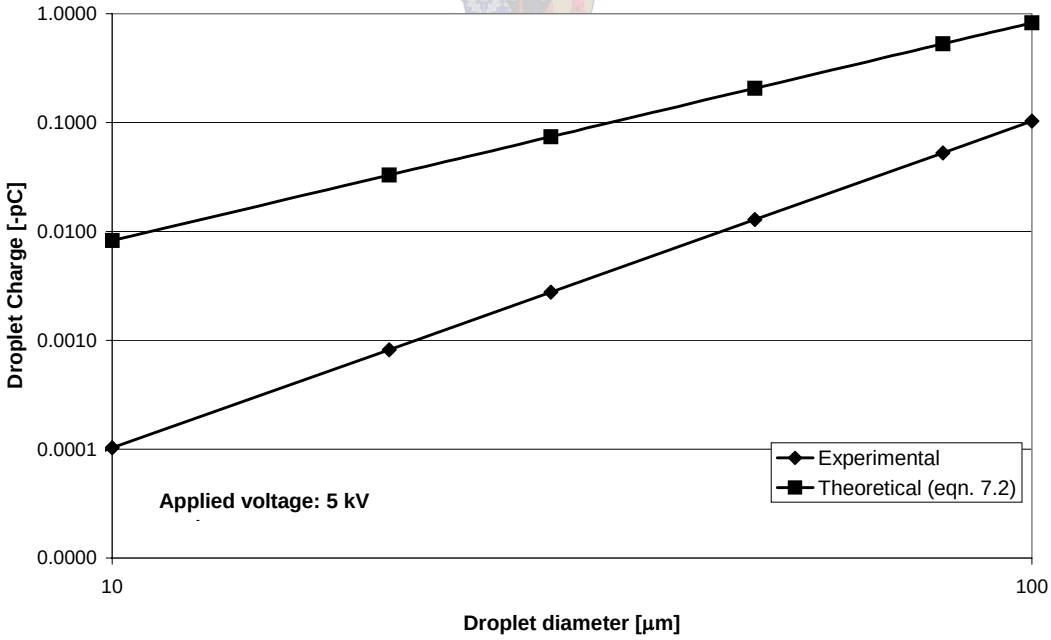

Figure 8.6 Graph of the comparison between experimental and theoretical droplet charge

8.4 Discussion and conclusion

The results of the electrostatic nozzle charging performance experiments indicated that the proposed nozzle functions satisfactorily in imparting electrical charge on liquid droplets. The experiments showed that the nozzle imparts 10% of the theoretical charge limit on the droplets. Owing to the difficulty in obtaining accurate measurements as a result of the small amounts of current encountered in the experiment, the actual charge on the droplets might be significantly higher.

9 Electrostatic spray applied to a charged heat exchanger

This chapter contains details of the experiments performed to determine the effect of making use of electrostatic forces to prevent surface wetting of a heat exchanger. The charging of the heat exchanger and the experimental set-up are discussed in detail. A technique of quantifying droplet deposition is presented and tested. The experimental results are presented and discussed.

9.1 Introduction

This chapter describes the experimental work performed to test the functionality of the capacitive type electrostatic nozzle used to prevent wetting of the fins of a heat exchanger when sprayed with droplets. The experiments are described and the results are presented and discussed.

9.2 Charging of the heat exchanger

For the purposes of this experiment, a rudimentary heat exchanger was constructed to approximate a large-scale heat exchanger. The heat exchanger was constructed from mild steel. The pitch of the fins on the heat exchanger was designed to be large enough to enable visual observations of what happens between the fins. The pitch, *P*, was chosen as 25 mm and the outside diameter, *D*, was chosen as 25 mm. Figure 9.1 shows a schematic of the heat exchanger used.

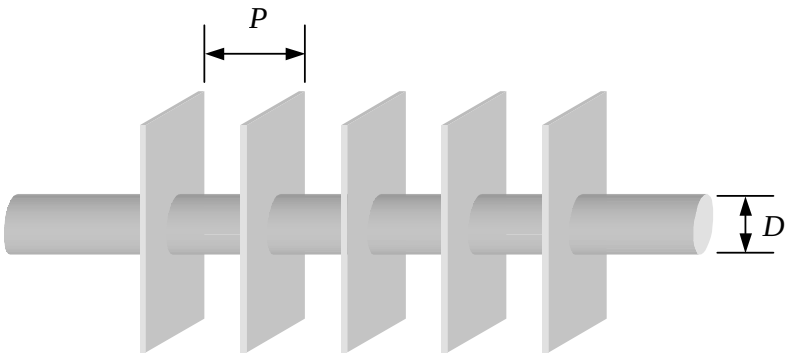

Figure 9.1 Schematic of rudimentary heat exchanger

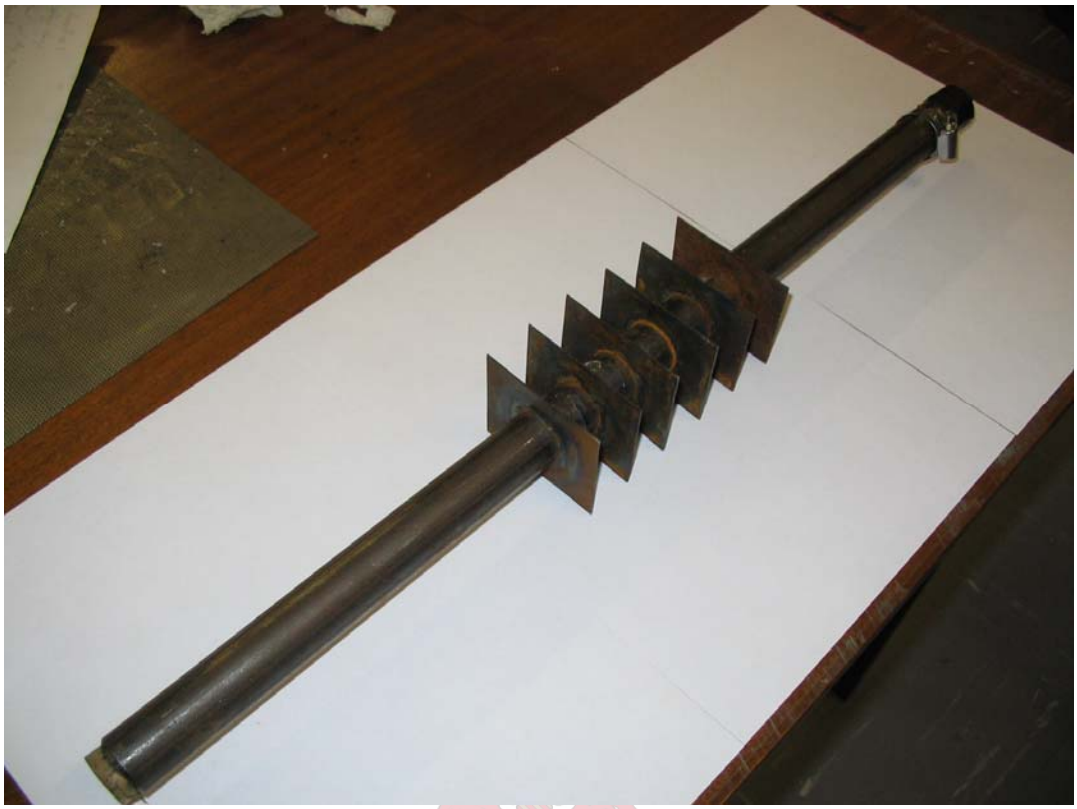

Figure 9.2 Rudimentary heat exchanger

For the purposes of the experiment, the heat exchanger had to be charged with a direct current (DC) voltage. An 11 kV high voltage DC source, obtained from the high voltage laboratory of the electrical engineering department of Stellenbosch University, was used to charge the heat exchanger. The high voltage DC source was powered with a DC power supply (GW GPR-30300 Laboratory DC Power Supply) set at 15 V. It was found that the 11 kV DC source could in fact only place a DC voltage of 8.4 kV on the heat exchanger. The DC source is shown in figure 9.3. Because the DC source could only produce a positive voltage, it was necessary to reverse the voltage clamp of the input signal system. This resulted in the droplets being positively charged, and therefore they will be repelled by the positively charged heat exchanger.

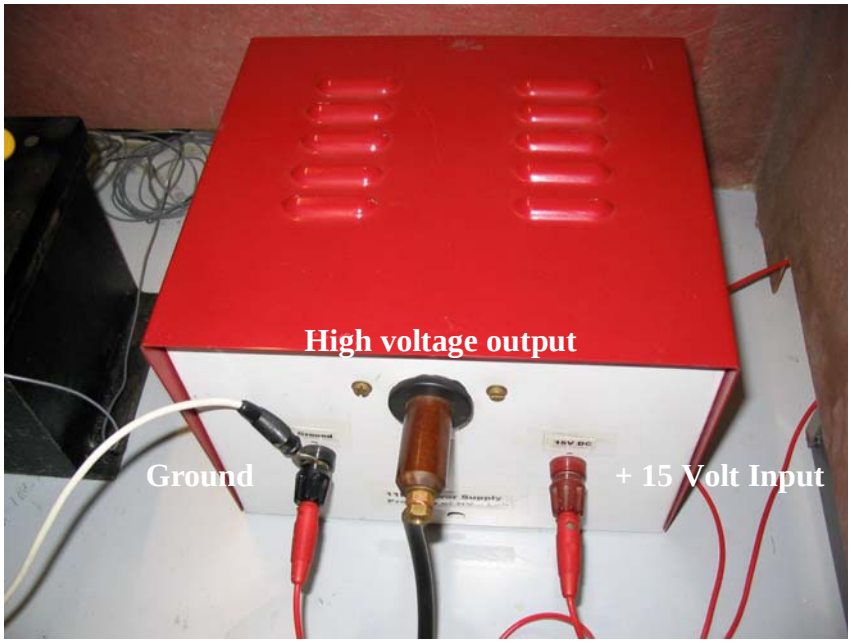

Figure 9.3 High voltage DC source

9.3 Experimental setup

The setup used for these experiments is shown schematically in figure 9.4. The capacitive electrostatic nozzle was placed in a mounting clamp, and connected to the water pump system. The induction ring of the nozzle was connected to the input signal system described in Chapter 6. Water chatchment trays were placed downstream of the nozzle to collect the excess water and thus prevent the experimental area from becoming flooded. The heat exchanger was placed in the spray path of the nozzle. In order to insulate the heat exchanger and prevent the high voltage from leaking to ground, two ceramic insulators were used to support the heat exchanger. These insulators were placed on wooden supports placed in the chatchment trays. The high voltage source described in the previous section was connected to the heat exchanger be means of a high voltage plug cable. The transformer used to generate the input signal to the induction ring of the nozzle and the high voltage DC source for the heat exchanger were placed in a protective glass fiber housing as a safety procedure, as shown in figure 9.7.

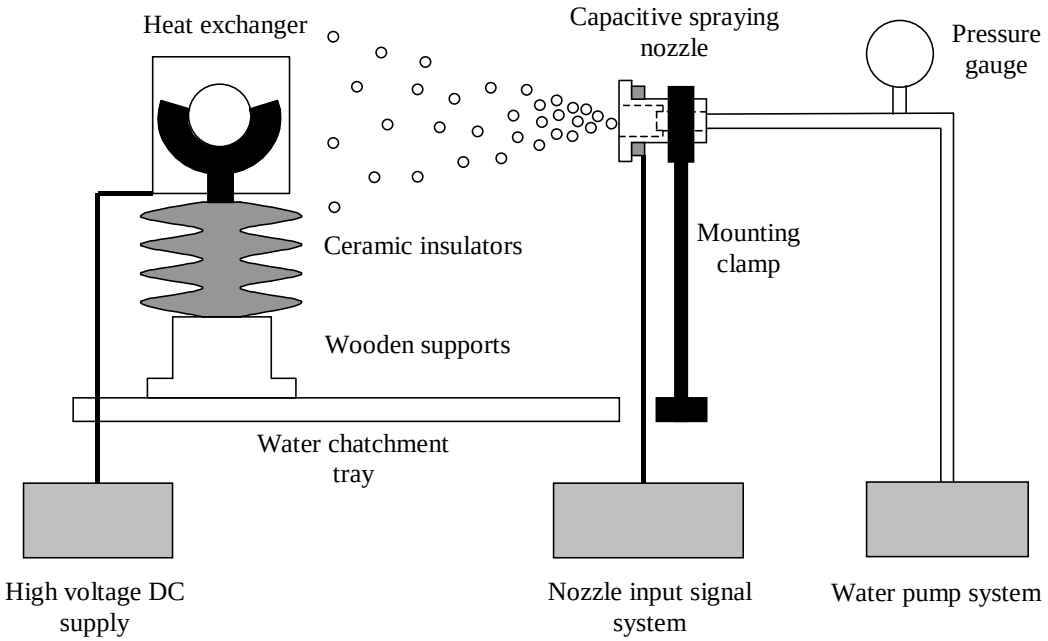

Figure 9.4 Schematic setup of electrostatic spray application experiment

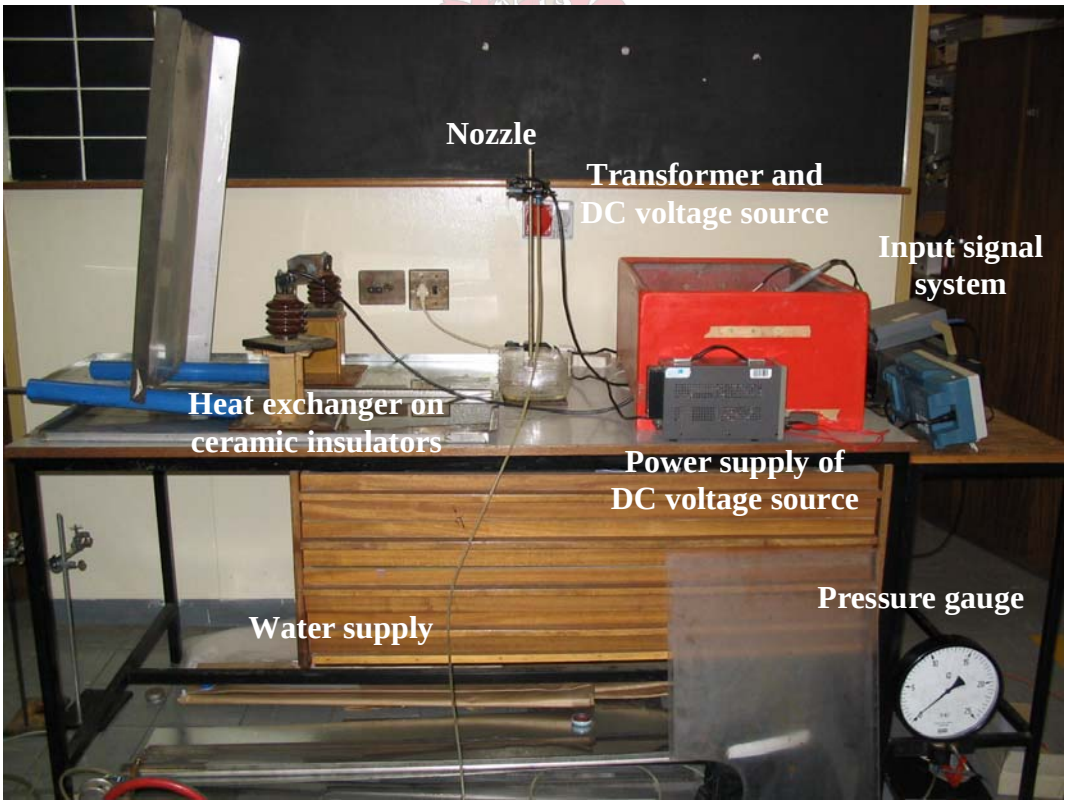

Figure 9.5 Setup of electrostatic spray application experiment

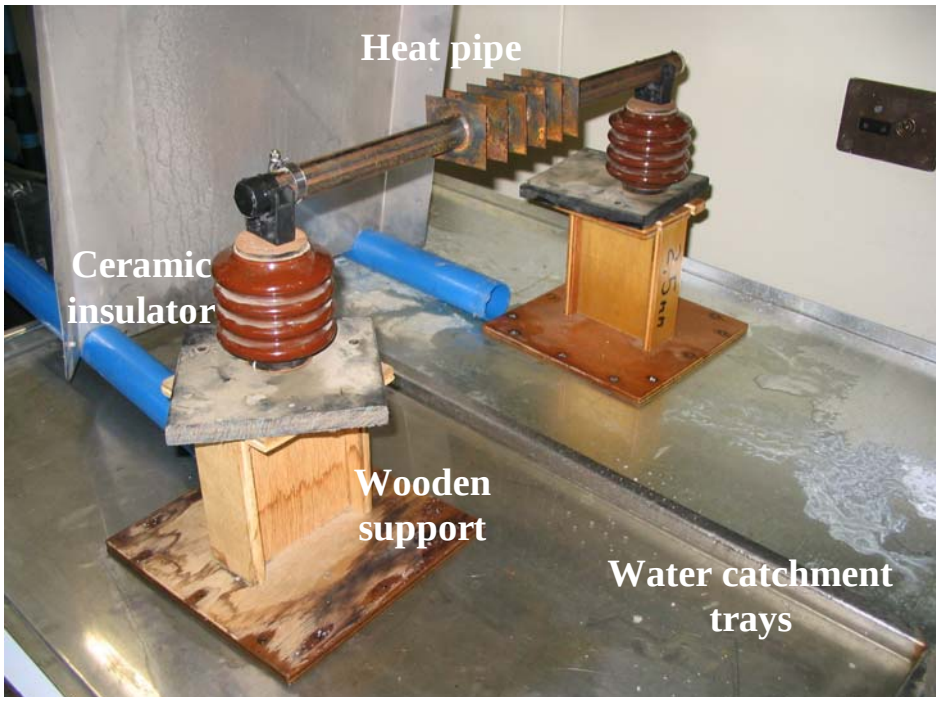

Figure 9.6 Heat exchanger mounted on ceramic insulators

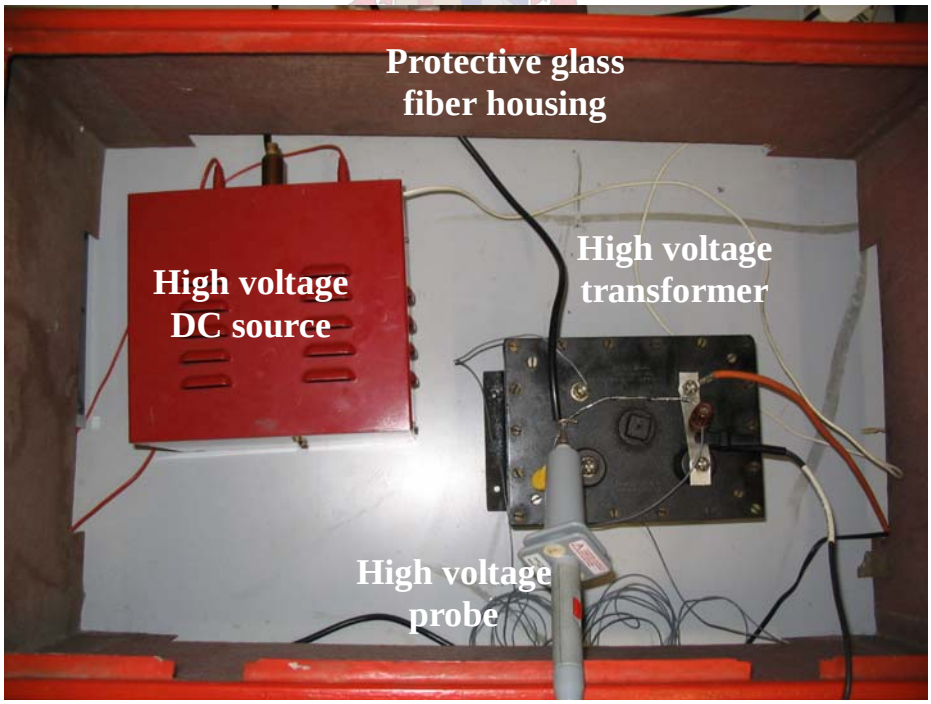

Figure 9.7 High voltage section in protective glass fiber housing

9.4 Deposition analysis

In order to measure the effectiveness of the charged spray in preventing or reducing the wetting of the heat exchanger surface, it was necessary to find a method of quantifying the mass of spray deposited. The most common method used is the one documented by Lane (1978). With this method, the targets are sprayed with a tracer-tagged solution containing a fluoride based tracer power. The tracer material is removed from the targets using a wash procedure with a wash solution of conditioned water containing 0.10% Triton X-100 surfactant. A fluorometer is then used to quantify the mass of tracer reclaimed from each target. Deposition density is then calculated and expressed as an amount of tracer material deposited per target area. This method is used extensively in agricultural research (Giles, 1985; Law, 1989). However, this method is complicated and involves the use of advanced equipment like a fluorometer. It has another drawback in that it can only be used to compare different experiments, because it doesn't provide the actual amount of water deposited onto the target, only the tracer deposition.

For the experiments performed for this project, another method of quantifying the droplet deposition onto the heat exchanger was used. This method is based on the principle that when moisture evaporates, the relative humidity of the air increases. A cylindrical Perspex container was constructed to encapsulate the heat exchanger. This container is used to measure the droplet deposition on the heat exchanger in the following manner. Four thermocouples were constructed and calibrated, with two of the thermocouples being covered with fabric. When the fabric was wetted, these thermocouples would measure the wetbulb temperature of the air. The other two thermocouples were left uncovered – they would measure the drybulb temperature of the air. These thermocouples are inserted into the container, and the container is closed and sealed. The drybulb and wetbulb temperatures in the container are measured, and the relative humidity of the air is calculated using equation (A.16) together with equation (A.5). The container is then opened, the thermocouples are removed and the heat exchanger with the droplets that impacted it during the test is inserted into the container. The container is then resealed and placed in a warm environment until all the moisture has evaporated. This point is determined by visual

inspection. The thermocouples are then re-inserted into the container and the drybulb and wetbulb temperatures are measured. The relative humidity of the air is again calculated using equation (A.16) together with equation (A.5). The procedure is shown in figure 9.8.

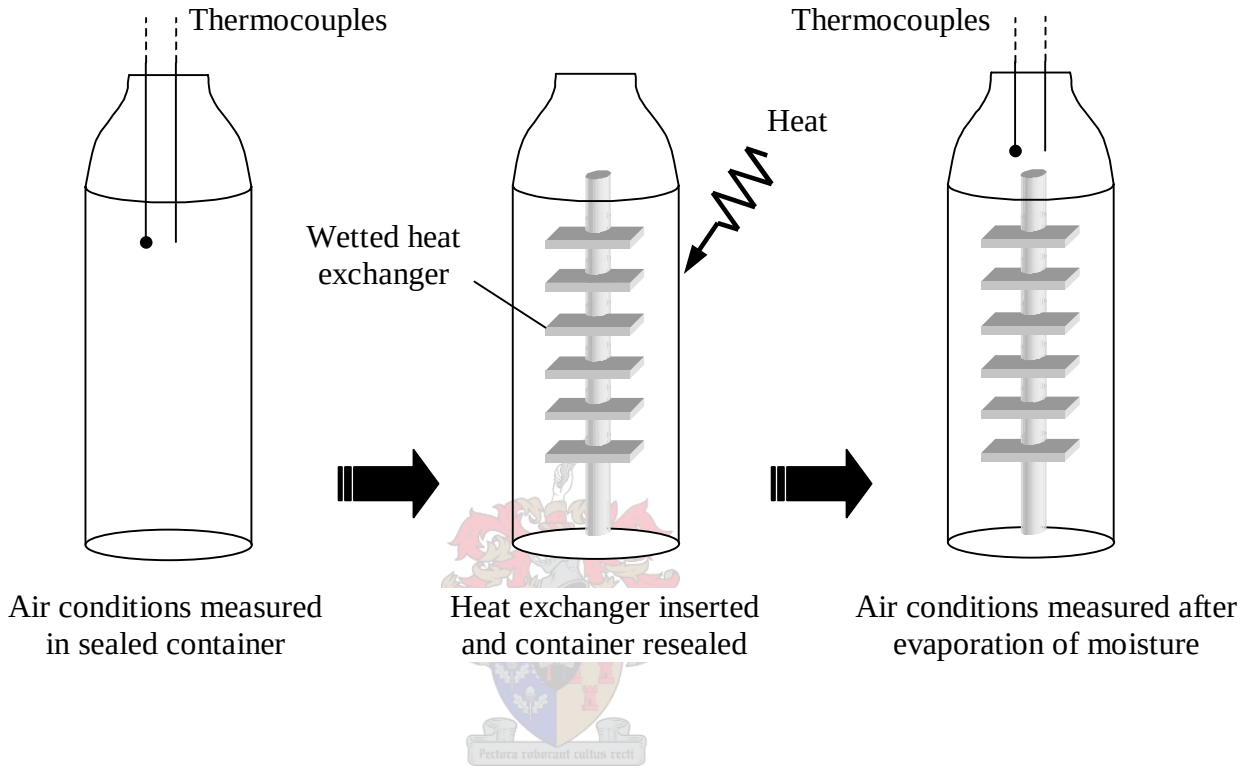

Figure 9.8 Schematic setup of deposition quantifying process

The difference between the relative humidity after the insertion of the heat exchanger and the initial relative humidity gives the change in relative humidity of the air. Knowing the volume of the container and calculating the density of the air at the initial temperature gives the mass of the dry air in the container. Making use of the following equation, the addition of water to the air can be calculated

$$m_w = \Delta\omega \cdot m_a \tag{9.1}$$

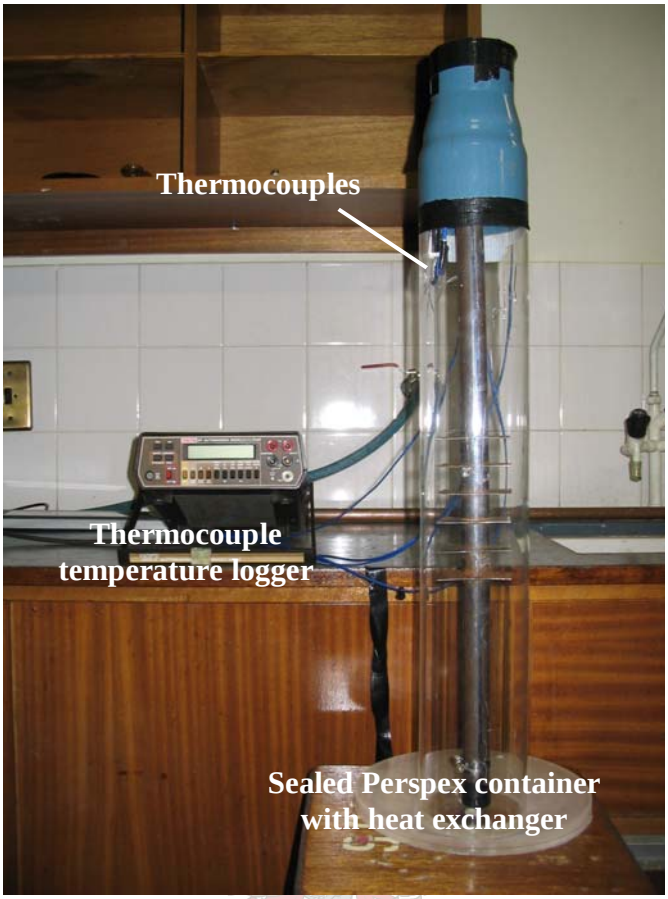

Figure 9.9 Deposition quantifying apparatus

By calculating the total area of the heat exchanger, and knowing the time duration that the heat exchanger was in the path of the spray, the droplet deposition density per unit area per unit time (DDPS) can be calculated

$$DDPS = \frac{m_w}{a_{he} \cdot t} \tag{9.2}$$

A series of tests were performed to check the accuracy of this deposition quantifying method. These test consisted of the following. The container was sealed and the conditions inside the container were measured, as explained above. The container was then opened briefly and water was sprayed into the container. Knowing the time duration and the flow rate of the nozzle, the amount of water sprayed into the container could be calculated. The container was then again sealed, and heat was added to the container until all the moisture had been evaporated. At this point the conditions inside the container was again measured, and the additional water in the air

calculated. In this manner the measured water addition could be compared with the known amount of water added by the spray. The result of this test is given in figure 9.10. It can be seen that an accuracy of about 15% was achieved, which was considered adequate for measuring the droplet deposition.

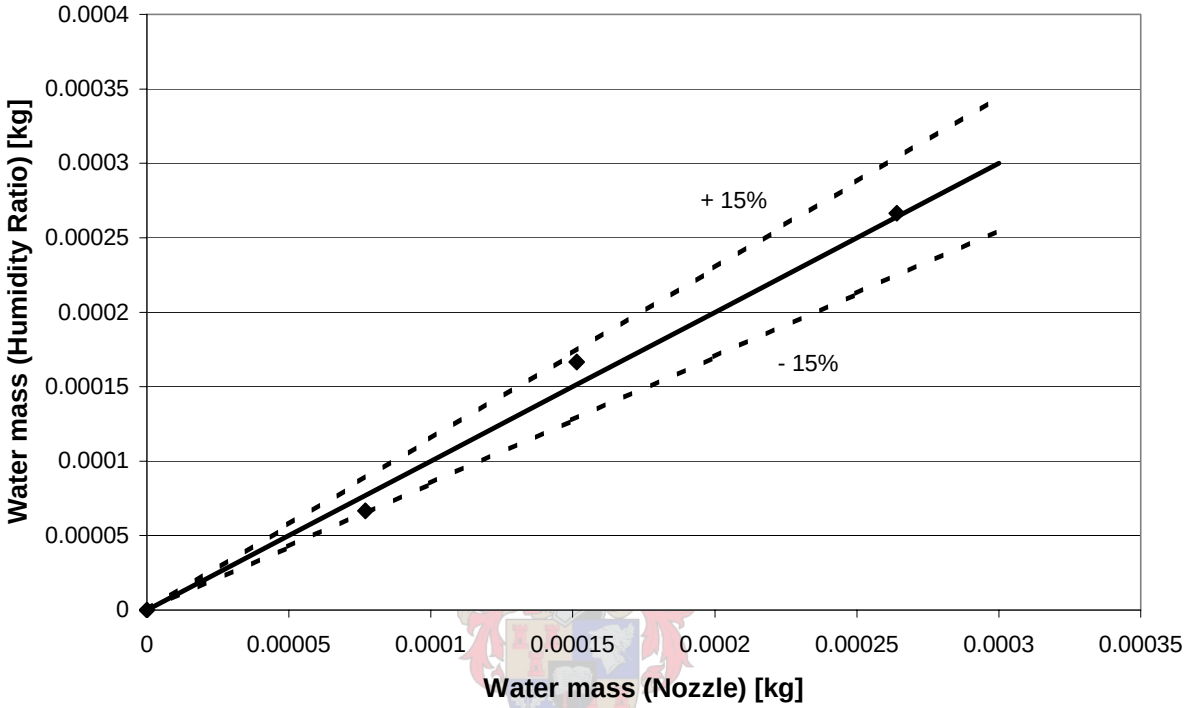

Figure 9.10 Accuracy of droplet deposition measurement

9.5 Nozzle type

It was found that the nozzle used for the nozzle charging performance experiments delivered a spray with relatively large droplets and a high flow rate. While this had been advantageous for those particular experiments, the spray application experiments required a nozzle that produced a smaller droplets size and a lower flow rate. For this purpose, a nozzle with an orifice diameter of 0.3 mm was chosen (MT Series 00003). This nozzle produces droplets in the region of 50 microns and a flow rate of 0.04 LPM at municipal water supply pressure ($\approx$300 kPa). A smaller nozzle frame cone

was constructed to house this nozzle. Figure 9.11 shows the two types of nozzle frame cones and the assembly procedure.

Figure 9.11 Nozzle assembly of large and small nozzles

9.6 Experimental procedure

In order to increase the electrostatic force on the liquid droplets, one can either increase the DC voltage on the heat exchanger, or one can increase the pulsed input voltage. With this setup, it was only possible to increase the input signal voltage. It was desired to determine the droplet deposition onto the heat exchanger surface at different input signal voltage values. The first step in the experimental procedure is to seal the Perspex container and measure the air conditions inside of the container. The high voltage DC source is then connected to the heat exchanger. The function

generator and audio amp is switched on, and the amplifier is set to the desired voltage level. The water supply is then switched on for 5 seconds. It was found that at the lowest voltage levels, 5 seconds was the maximum amount of time the heat exchanger could be sprayed before droplets started forming and falling from the heat exchanger. After 5 seconds the high voltage DC source is switched off, the heat exchanger is removed from it's mounting and placed inside the Perspex container. The container is then sealed and placed in a warm environment until all the moisture has been evaporated. Once this has happened, the air conditions in the container are measured. At this point the test has been completed, and the next test can be started.

9.7 Experimental results

A series of experiments were performed to try to determine a relation between droplet deposition and input signal peak voltage. The maximum capability of the input signal system was -7.5 kV peak voltage. The voltage values for the test were chosen as -2.5 kV, -3.75 kV, -5 kV, -6.25 kV and -7.5 kV. In order to ensure consistency and repeatability, three test runs were performed at each peak voltage level. The experimental data for the test are presented in Appendix C. Figure 9.12 indicates the effect of an increase in induction ring peak voltage on target droplet deposition density (DDPS).

A non-linear model fitting for this data yielded the following relationship

$$DDPS = -37.569 \ln(V_{ir}) + 82.937 \tag{9.3}$$

with $R^2 = 0.9931$

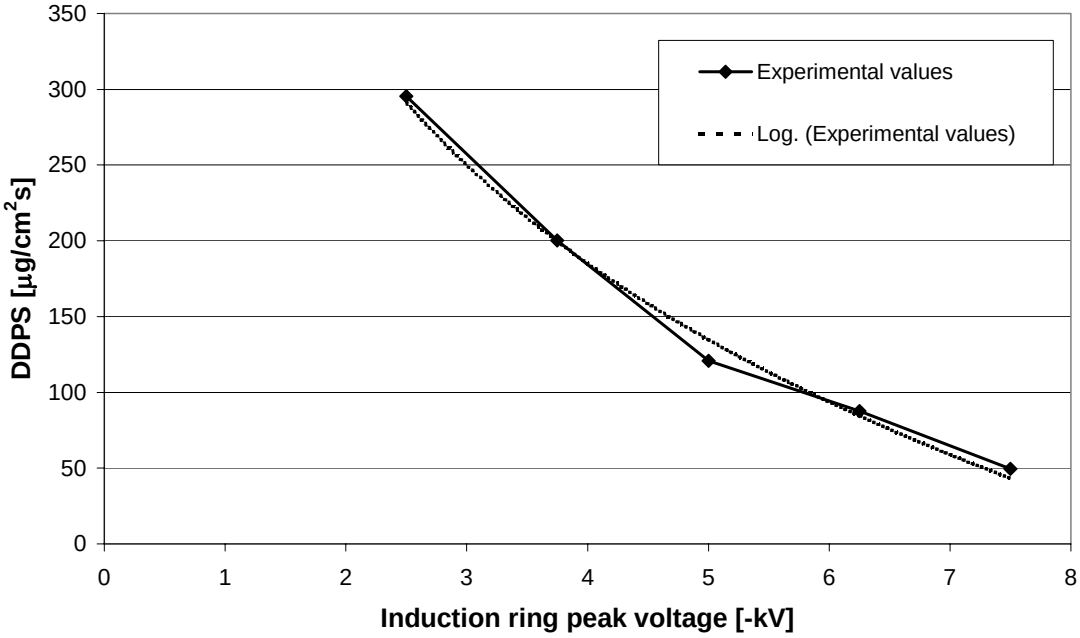

Figure 9.12 Relation between droplet deposition density and induction ring peak voltage

Inspection of figure 9.12 shows that droplet deposition density is greatly affected by the increase in induction ring peak voltage. It is evident that the droplet deposition density decreases as the induction ring peak voltage (and therefore the droplet charge) is increased. This would seem to indicate that if the droplet charge were to be continuously increased, a point would be reached were all the droplets are repelled from the surface and the heat exchanger remains dry. However, the maximum capability of the input signal system was -7.5 kV. Further tests to determine the behavior of the droplets and the deposition density at higher induction ring peak voltages could therefore not be performed using the current setup.

9.8 Discussion

The trend found in the experiments and displayed in figure 9.12 shows that the proposed method of preventing heat exchanger surface wetting when making use of air pre-cooling might hold some promise. Examples of similar work to compare these

results with could not be found in literature. However, in experiments performed by Law (1989) on the electrical interactions occurring at electrostatic spraying targets, he attempted to determine, for a spherical target, at what target potential charged spray deposition becomes significantly impeded. His results are presented in figure 9.13.

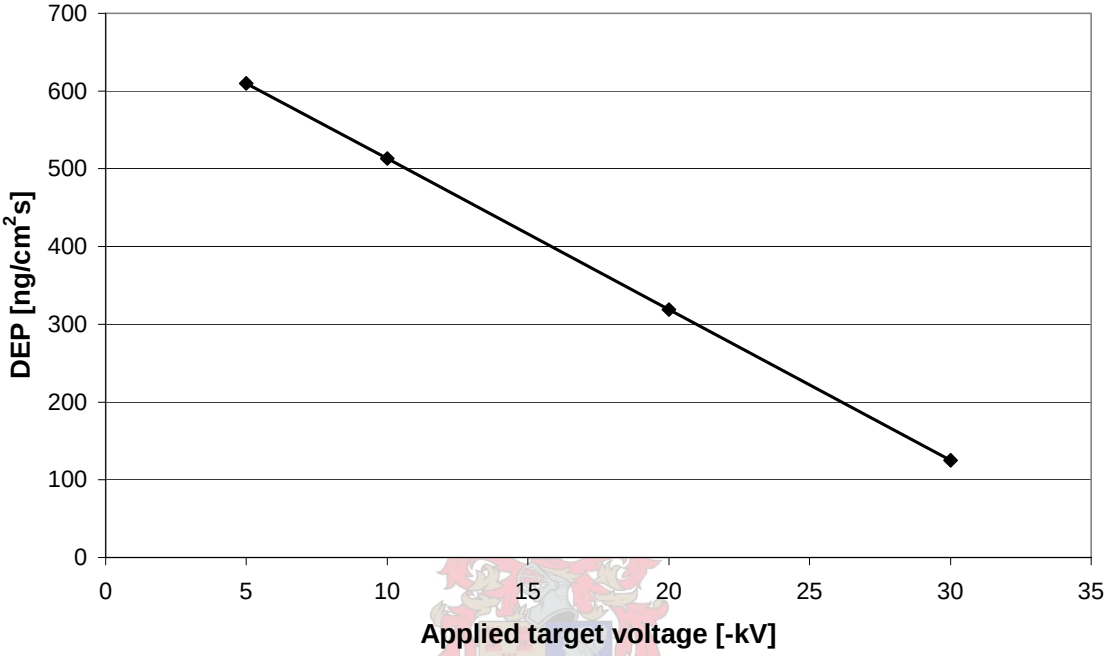

Figure 9.13 Relation between droplet deposition density and applied target voltage (Law, 1989)

Law (1989) maintained the droplet charge and increased the target potential. He made use of the fluorometric procedure explained in section 9.4 to determine the deposition density. This makes comparison of his results with the results found in this study difficult. However, he found a decrease in deposition density as the target potential is increased, indicating a similar trend as was found in the experiments performed for this study. His results also indicate that it might be advantageous to maintain the droplet charge and increase the target potential. However, increasing the potential of the heat exchanger in practice might result in additional complications and risks.

An important consideration of evaporative cooling systems is the additional power consumption associated with the system. In order to evaluate the power consumption

of the system tested in this project, a brief projection of the power consumption was done and compared to the power consumption of a conventional high pressure atomizing system. Based on information from the literature study, it was assumed that the amount of heat exchanger wetting achieved in the test performed at the highest voltage level (7.5 kV) with droplets of 50 micron was the equivalent of the heat exchanger wetting achieved when making use of a conventional high pressure spray with a droplet size of 10 micron (Branfield, 2003). It was assumed that both the electrostatic spray system and the high pressure spray system made use of pressure swirl atomizers to achieve the desired droplet size. The power required to achieve the droplets with a pressure swirl atomizer was determined using the following equation (Lefebvre, 1989)

$$SMD = 2.25\sigma^{0.25}\mu_l^{0.25}\dot{m}_l^{0.25}\Delta P_l^{-0.5}\rho_a^{-0.25} \tag{9.3}$$

In order to obtain a meaningful comparison, it was decided to calculate the increase in power consumption with increasing water flow rate. An increased water flow rate will result in increased cooling, while at the same time resulting in increased surface wetting. The results of the calculation are given in figure 9.14.

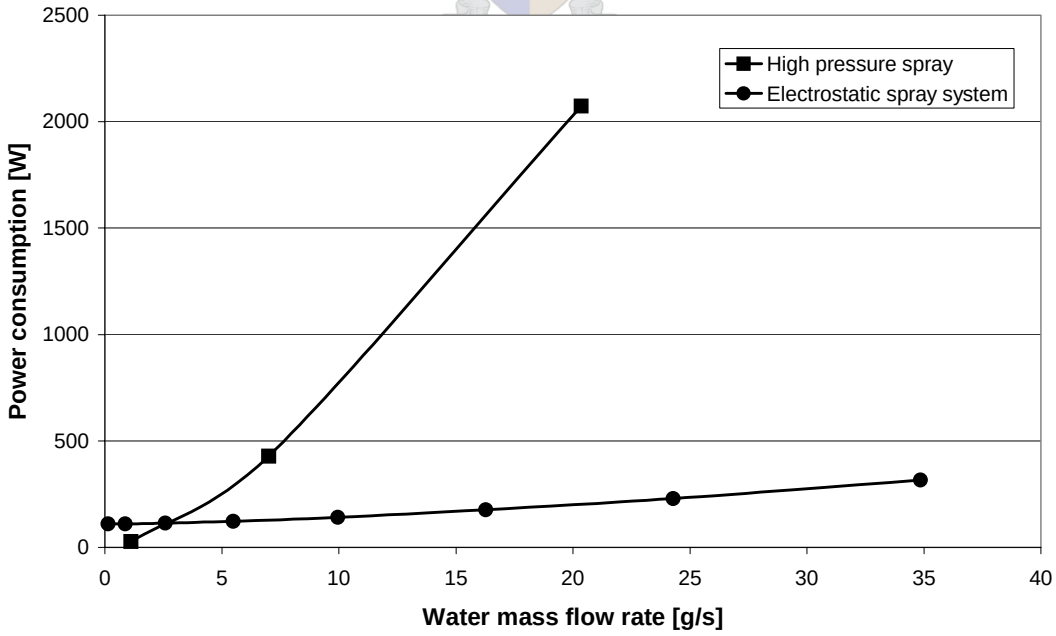

Figure 9.14 Comparison of power consumption of high pressure and electrostatic spray

The electrostatic spray system has the additional power requirement of the electronic input signal system, which remains fixed as the flow rate is increased. It is apparent from the graph that at very low flow rates, the power consumption of the electrostatic spray system is higher than the high pressure system because of the additional power consumption of the electronic input signal system. However, as the flow rate increases, the high-pressure system requires an increasing amount of power to produce the small droplet size. Because the electrostatic spray system makes use of a larger droplet size, the increase in power consumption is not so severe. This indicates that the use of an electrostatic spray system might be a possibility for applications where a higher water flow rate is required.

10 Discussion and recommendations

This chapter contains a discussion of the work done for this project. Recommendations are made as to further research required on the proposed system.

10.1 Discussion

In this study an investigation was made of the practical aspects of the performance improvement of an air-cooled heat exchanger with the use of evaporative pre-cooling of air. A study of previous work indicated that the concept is theoretically possible, but there are still many challenges to overcome and the practical application thereof is still in development.

The first part of the study concerned practical aspects of the evaporation of droplets by firstly investigating the evaporation of droplets in a free stream and secondly investigating the evaporation of droplets in a hydrodynamic boundary layer and the consequent improvement in heat transfer coefficient. The mathematical model for the evaporation of droplets in the free stream was verified by comparing it to previous theoretical work (Lefebvre, 1989; Duvenhage, 1993; Kritzinger, 1999) and previous experimental work (Hall and Diederichsen, 1953). Verification of the mathematical model for the evaporation of droplets in the boundary layer presents a challenge. The small size of the droplets involved as well as the size of a boundary layer makes accurate experimental measurements difficult. A special high speed – high-resolution camera or a laser droplet sizer might be used for such experiments.

Combining the two models derived for evaporation of a droplet in free stream and in a boundary layer yields a model for the entire lifetime of a droplet from the moment it issues from the nozzle orifice to the moment it has completely evaporated. Although the accuracy of this model still has to be verified, it already provides insights into the behavior of evaporating droplets that might be useful in the development of an effective evaporative pre-cooling system.

The second part of the study consisted of the design and testing of an evaporative cooling system using electrostatic forces to ensure that the heat exchanger remained dry. Investigation of the literature indicated that corrosion and fouling were some of the major concerns when dealing with an evaporative cooling system for performance improvement of a heat exchanger. Attention was therefore focused on preventing the droplets from impacting the heat exchanger surface.

A capacitive electrostatic nozzle was chosen for the system because of its relative simplicity and affordability. This nozzle was tested and it was found that the nozzle imparted a charge of 10% of the theoretical maximum charge on the droplets.

Experiments were performed whereby the charged spray was directed at a heat exchanger with a similar charge as the droplets in the spray. It was found that as the charge on the droplets was increased the droplet deposition on the heat exchanger decreased. The trend displayed showed that if the charge on the droplets could be increased, a point might be reached where there is zero droplet deposition on the heat exchanger. However, the input signal system could not generate a large enough input voltage to reach this point. Experiments performed by Law (1998) indicated that similar results could be obtained by increasing the heat exchanger potential.

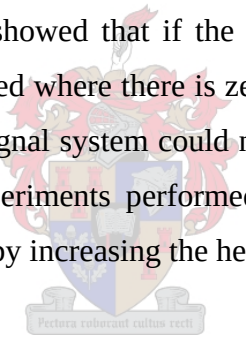

One major drawback of such an electrostatic system is that any liquid flowing in the heat exchanger that is directly connected to ground would result in the heat exchanger potential leaking to ground. A system will have to be devised whereby the liquid flowing in the pipes can be electrically disconnected from ground. However, this problem might be overcome if there is gas flowing in the heat exchanger, as is the case at synthetic fuel plants such as Sasol Secunda. The properties of the gas, however, might influence the system. Possible altercation of the gas properties by the electric field must also be considered. This concept might also be used for air-cooled condensers at power plants. However, the way in which the electric field might affect the steam must be considered.

There is clearly a need for more research into the performance improvement of air-cooled heat exchanger. At this stage, no reliable method of evaporative precooling of

air has yet been found. The only viable solution for cooling capacity shortages at present is the construction of additional dry or wet cooling towers.

10.2 Recommendations

Judging from the literature, the use of evaporative pre-cooling of air for performance improvement of air-cooled heat exchangers is still in its infancy. The concept has been shown to work, but finding a cheap, reliable method of achieving this has proven to be more challenging than initially believed. The work done for this project shows much promise. However, making use of electrostatics involves high voltage electrical system, which adds to the complexity, cost and safety concerns of the system. Some suggested areas of additional research on this subject are:

- An investigation into the effect of increased droplet charge. If the trend established in this project is followed, there should exist a point where the droplets have sufficient charge to ensure that they do not impact the surface of the heat exchanger. It might be more practical to make use of an embedded electrode electrostatic spray nozzle (Law, 1978). Despite the extra cost associated with these nozzles, they can produce a higher droplet charge.

- An investigation into the effect of maintaining the droplet charge and increasing the heat exchanger charge. Because of the droplet charge limit imposed by the theoretical maximum droplet charge, it might be necessary to make use of an increased heat exchanger voltage to attain the point where all the droplets are repelled from the heat exchanger surface.

- An investigation into the possibly of implementing such a system with an existing air-cooled heat exchanger installation. Alternatively, an investigation into the implementation of such a system with a newly built heat exchanger system specifically designed to incorporate the system. This includes factors such as safety, costs and suitable gasses and fluids in the heat exchanger.

- A simulation by means of a computer package of the electrostatic interaction occurring at the heat exchanger surface.

11 References

Bassily, A.M., Effects of evaporative inlet and aftercooling on the recuperated gas turbine cycle, Applied Thermal Engineering, Vol. 21, pp. 1875-1890, 2001.

Bassily, A.M., Performance improvements of the intercooled reheat regenerative gas turbine cycles using indirect evaporative cooling of the inlet air and evaporative cooling of the compressor discharge, Proceedings of the Institute of Mechanical Engineers Part A, Journal of Power and Energy, accepted for publication, 1990.

Bhatti, M.S. and Savery, C.W., Augmentation of heat transfer in a laminar external gas boundary layer by the vaporization of suspended droplets, Journal of Heat and Mass Transfer, pp.179-184, May 1975.

Botes, H., An investigation into the application of adiabatic pre-cooling in an air-cooled heat exchanger, M.Eng Thesis, University of Stellenbosch, 1995.

Branfield, G., Performance evaluation of heat exchangers with evaporative pre-cooling, B.Eng Thesis, University of Stellenbosch, 2003.

Conradie, T.A., Aanvullende nat verkoeling by droë verkoelde kragsentrales, M.Eng Thesis, University of Stellenbosch, 1990.

Cooper, S.C., Law, S.E., Transient characteristics of charged spray deposition occurring under action of induced target coronas: space-charge polarity effect, Proceedings of the 1987 Oxford University Conference on Electrostatics, British Institute of Physics Conference Series No. 85 (Section 1), pp. 21-26, 1987.

De Lucia, Lanfranchi, C. and Boggio, V., Benefits of compressor inlet air cooling for gas turbine cogeneration plants, Proceedings of the International Gas Turbine and Aeroengine congress and Exposition, Houston, Texas, 1995.

Duvenhage, K., Warmteruiling met adiabatiese voorverkoeling, M.Eng Thesis, University of Stellenbosch, 1993.

Elperin, I.T., Heat Transfer of Two-Phase Flow with a Bundle of Tubes, Inzhererno Fizicheski Zhurnal, Vol. 4, nr. 8, pp. 30-35, 1961.

Esterhuyse, B. D., Prediction and Measurement of the Performance of Co-current and Cross-flow Direct Evaporative Air Coolers, B.Eng Thesis, University of Stellenbosch, 2002.

Feath, G.M., Current Status of Droplet and Liquid Combustion, Prog. Energy Combust. Sci., Vol. 3, pp. 191-224, 1977.

Frossling, N., On the Evaporation of Falling Droplets, Gerlands Beitr. Geophys., Vol. 52, pp.170-216, 1938.

Gasparovic, N. and Stapersma, D., Gas turbine with heat exchanger and water injection in the compressed air, Journal of Combustion, Vol. 44, pp. 6-16, 1973.

Giles, D. K. and Law, S. E., Space charge depositions of pesticide sprays onto cylindrical target arrays, Trans. of ASAE, Vol 28(3), pp. 658-664, 1985.

Giourof, A., Gas turbine inlet air cooling: you can almost pick your payback, Power 139, Vol. 5, pp. 56 – 58, 1995.

Godsave, G.A.E., Studies of the Combustion of Drops in a Fuel Spray – the Burning of Single Drops of Fuel, Fourth Symposium (International) on Combustion, Williams and Wilkins, Baltimore, pp. 818-830, 1953.

Hall, A. R. and Diederrichsen, J., An Experimental Study of the Burning of Single Drops of Fuel in Air at Pressures up to Twenty Atmospheres, Fourth Symposium (International) on Combustion, W & W, Baltimore, pp. 837-846, 1953.

Hendriks, C. D., Charging macroscopic particles, Electrostatics and its Applications, A.D. Moore, Ed., New York, Wiley, ch.4, p. 60, 1973.

Houghton, E. L., Carpenter, P. W., Aerodynamics for Engineering Students, Arnold, London, 1993.

Hufford, P.E., Absorption chillers improve cogeneration energy efficiency. ASHRAE Journal, pp.46 – 53, 1992.

Kays, W.M., Convective Heat and Mass Transfer, McGraw-Hill, New York, pp.204-209, 1966.

Klüsener, O., The injection Process in Compressorless Diesel Engines, VDI Z., Vol. 77, No. 7, February 1933.

Kriel, D.E., Prediction and measurement of the performance of spray cooled heat exchangers, M.Eng Thesis, University of Stellenbosch, 1991.

Kritzinger, H. P., A Rotating Sprayer for the Application of Adiabatic Precooling with Atomized Water Injection on Air Cooled Heat Exchangers, M.Eng Thesis, University of Stellenbosch, 1999.

Kröger, D.G., Air-cooled heat exchangers and cooling towers, Penwell Corp, Tulsa, 2004.

Lane, M. D., Transient charge transfer occurring during electro-static deposition of particulate clouds onto foliar and metallic targets. Unpublished M.S. thesis, Department of Agricultural Engineering, University of Georgia, Athens, 1978.

Law, S. E., Electrical interactions occurring at electrostatic spraying targets, Journal of Electrostatics, Vol. 23, pp. 145-156, 1989.

Law, S.E., Bailey, A.G., Perturbations of charged-droplet trajectories caused by induced target corona: laser Doppler analysis, IEEE Trans. IA-20, Vol. 6, pp. 1613-1622, 1984.

Law, S.E., Basic phenomena active in electrostatic pesticide spraying, in: K.J. Brent, R.K. Atkin (Eds.), Rational Pesticide Use, Cambridge University Press, Cambridge, England, pp. 81-105, 1987.

Law, S.E., Bowen, H.D., Theoretically predicted interactions of surface charge and evaporation on airborne pesticide droplets, Trans. ASAE 18, Vol. 1, pp. 35-39, 45, 1975.

Law, S.E., Electrostatic pesticide spraying: concepts and practice, IEEE Trans. IA-19, Vol.2, pp 160-168, 1983.

Law, S.E., Embedded-electrode electrostatic-induction spray-charging nozzle: theoretical and engineering design, Trans. ASAE 21, Vol. 6, pp 1096-1104, 1978.

Law, S.E., Lane, M.D., Electrostatic deposition of pesticide sprays onto ionizing targets: charge- and mass-transfer analysis, IEEE Trans. IA-18, Vol. 6, pp. 673-679, 1982.

Lee, S.L., Yang, Z.H. and Hsyua, Y., Cooling of a heated surface by mist flow, Journal of Heat Transfer, Vol.116, pp.167-172, 1994.

Lefebvre, A.H., Atomization and Sprays, Hemisphere Publishing Corporation, New York, 1989.

Leidenfrost, W. and Korenic, B., Evaporative cooling and heat transfer augmentation related to reduced condenser temperatures, Heat Transfer Engineering, Vol.3, Nos.3-4, pp. 38-59, 1982.

Lenard, P., Über die Electricität der Wasserfalle, Ann. Phys. 3, Vol.46, pp 584-636, 1892.

Masters, K., Spray Drying Handbook, 4th edition, George Godwin Limited, London, 1985.

Mathur, G.D., Direct-Indirect evaporative cooling with heat pipe heat exchangers, National Heat Transfer Conference: Minneapolis, Paper 91-HT-20, 1991.

Najjar, Y.S. and Zaamout, M.S., Enhancing gas-turbine engine performance by means of the evaporative regenerative cycle, Journal of the Institute of Energy, Vol. 69, pp. 2-8, 1996.

Nakayama, W., Kuwahara, H. and Hirasawa S., Heat transfer from tube banks to air/water mist flow, International Journal of Heat and Mass Transfer, Vol.31, No.2, pp.449-460, 1988.

Oplatka, G., Improved operating characteristics of dry cooling towers by partial precooling of the air, Brown Boveri Review, No.3/4-81, pp.136-143, 1981.

Perlman, H., Trends in Water use: 1950-1990, Estimated use of water in the United States in 1990, US Geological Services: Water-use Home Page, http://h20.er.usgs.gov/public/watuse/wutrends.html, 1996.

Peter Castle, G.S. and Inculet, I.I., Space charge effects in orchard spraying, IEEE Trans. IA IA-19, Vol. 3, pp. 476-480, 1982.

Probert, R.P., Philos. Mag., Vol. 37, p. 94, 1946.

Ranz, W.E. and Marshall, W.R., Evaporation from drops, Chemical engineering progress, Vol.48, Part 1, pp.141-146, Part 2, pp. 173-180, 1952.

Rubin, A.M., Demonstration of adiabatic cooling to improve the performance of air-cooled heat exchangers, Franklin Institute Research Laboratories, Pennsylvania, 1975.

Savery, C.W., Juedes, D.L. and Borman, G.L., n-Heptane, Carbon Dioxide and Chlorotrifluoromethane Droplet Vaporisation Measurements at Supercritical Pressures, Ind. Chem. Fundam., Vol. 10, No. 4, pp.543-553, 1971.

Schlichting, H., Boundary Layer Theory, McGraw-Hill, New York, 6th Ed., pp. 130, 1968.

Spalding, D.B., The Combustion of Liquid Fuels, Fourth Symposium (International) on Combustion, Williams and Wilkins, Baltimore, pp. 847-864, 1953.

Surface, M.O., System designs for dry cooling towers, Power Engineering, pp. 42-50, September 1977.
Turner, P. R., Guide to Scientific Computing, 2nd edition, MacMillan Press Ltd., Londen, 2000.

Wachtell, G.P., Atomised water injection to improve dry cooling tower performance, Franklin Institute Research Laboratories, Report no. COO-2241-1, 1974.

White, F.M., Fluid Mechanics, 4th edition, McGraw-Hill Book Co., Singapore, 1994.

Williams, A., Fundamentals of Oil Combustion, Prog. Energy Combust. Sci., Vol. 2, pp. 167-179, 1976.

Woest, M., Hearn, I. and Lennon, S.J., Investigation into the corrosion behaviour of galvanized finned tubing for cooling under deluge enhanced wet/dry cooling conditions, ESCOM, Scientific Investigations Report No. S91/030, 1991.

Yang, W.-J. and Clarke, D.W., Spray cooling of air-cooled compact heat exchangers, International Journal of Heat and Mass Transfer, Vol.18, pp.311-317, 1975.

Appendix A - Properties of fluids

Appendix A gives the fluid properties of dry air, saturated water vapor, mixtures of air and water vapor and saturated water liquid.

The thermophysical properties of dry air from 220K to 380K at standard atmospheric pressure (101325 N/m^2)

Density:

$$\rho_a = \frac{p_a}{287.08 \cdot T}, [\text{kg/m}^3] \tag{A.1}$$

Specific Heat:

$$c_{p_a} = 1.045356 \cdot 10^3 - 3.161783 \cdot 10^{-1} \cdot T + 7.083814 \cdot 10^{-4} \cdot T^2 - 2.705209 \cdot 10^{-7} \cdot T^3, \quad [\text{J/kgK}] \tag{A.2}$$

Dynamic Viscosity:

$$\mu_a = 2.287973 \cdot 10^{-6} + 6.259793 \cdot 10^{-8} \cdot T - 3.1315956 \cdot 10^{-11} \cdot T^2 + 8.15038 \cdot 10^{-15} \cdot T^3, \quad [\text{kg/ms}] \tag{A.3}$$

Thermal conductivity:

$$k_a = -4.937787 \cdot 10^{-4} + 1.018087 \cdot 10^{-4} \cdot T - 4.627937 \cdot 10^{-8} \cdot T^2 + 1.250603 \cdot 10^{-11} \cdot T^3, \quad [\text{W/mK}] \tag{A.4}$$

The thermophysical properties of saturated water vapor from 273.15K to 380K.

Vapor pressure:

$$p_v = 10^z, \ [\mathrm{N/m^2}] \tag{A.5}$$

$$z = 10.79586\left(1-\frac{273.16}{T}\right) + 5.02808\log_{10}\left(\frac{273.16}{T}\right) + 1.50474\cdot 10^{-4}\left[1-10^{-8.29692\left(\frac{T}{273.16}-1\right)}\right] + 4.2873\cdot 10^{-4}\left[10^{4.76955\left(1-\frac{273.16}{T}\right)}-1\right] + 2.786118312$$

Specific heat:

$$c_{p_v} = 1.3605\cdot 10^3 + 2.31334\cdot T - 2.46784\cdot 10^{-10}\cdot T^5 + 5.91332\cdot 10^{-13}\cdot T^6, \quad [\mathrm{J/kgK}] \tag{A.6}$$

Dynamic viscosity:

$$\mu_v = 2.562435\cdot 10^{-6} + 1.816683\cdot 10^{-8}\cdot T + 2.579066\cdot 10^{-11}\cdot T^2 - 1.067299\cdot 10^{-14}\cdot T^3, \quad [\mathrm{kg/ms}] \tag{A.7}$$

Thermal conductivity:

$$k_v = 1.3406\cdot 10^{-2} - 3.756191\cdot 10^{-5}\cdot T + 2.217964\cdot 10^{-7}\cdot T^2 \cdot -1.111562\cdot 10^{-10}\cdot T^3, \quad [\mathrm{W/mK}] \tag{A.8}$$

Vapor density:

$$\rho_v = -4.062329056 + 0.10277044\cdot T - 9.76300388\cdot 10^{-4}\cdot T^2 + 4.475240795\cdot 10^{-6}\cdot T^3 - 1.004596894\cdot 10^{-8}\cdot T^4 + 8.9154895\cdot 10^{-12}\cdot T^5, \quad [\mathrm{kg/m^3}] \tag{A.9}$$

Temperature:

$$T = 164.630366 + 1.832295 \cdot 10^{-3} \cdot p_v + 4.27215 \cdot 10^{-10} \cdot p_v{}^2 + 3.738954 \cdot 10^3 \cdot p_v{}^{-1} - 7.01204 \cdot 10^5 \cdot p_v{}^{-2} + 16.161488 \ln p_v - 1.437169 \cdot 10^{-4} \cdot p_v \cdot \ln p_v, [K] \quad \text{(A.10)}$$

The thermophysical properties of mixtures of air and water vapour.

Density:

$$\rho_{av} = (1+w)\left[\frac{1-w}{w+0.62198}\right]\frac{p_{abs}}{287.08\cdot T},\ [\text{kg}_{\text{air-vapour}}/\text{m}^3] \tag{A.11}$$

Specific heat [1978 FA1]:

$$c_{p_{av}} = \frac{(c_{p_a} + w\cdot c_{p_v})}{1+w},\ [\text{J/kg}_{\text{air-vapour}}] \tag{A.12}$$

or the specific heat of the air-vapor mixture per unit mass of dry air:

$$c_{p_{ma}} = c_{p_a} + w\cdot c_{p_v},\ [\text{J/kg}_{\text{dry air}}] \tag{A.13}$$

Dynamic viscosity:

$$\mu_{av} = \frac{X_a\mu_a\sqrt{M_a} + X_v\mu_v\sqrt{M_v}}{X_a\sqrt{M_a} + X_v\sqrt{M_v}},\ [\text{kg/ms}] \tag{A.14}$$

where $M_a = 28.97\,kg/mole, M_v = 18.016\,kg/mole, X_a = \frac{1}{1+1.608w}, X_v = \frac{w}{w+0.622}$

Thermal conductivity:

$$k_{av} = \frac{X_a k_a\sqrt[3]{M_a} + X_v k_v\sqrt[3]{M_v}}{X_a\sqrt[3]{M_a} + X_v\sqrt[3]{M_v}},\ [\text{W/mK}] \tag{A.15}$$

Humidity ratio:

$$w = \left(\frac{2501.6 - 2.3263(T_{wb} - 273.15)}{2501.6 + 1.8577(T - 273.15) - 4.184(T_{wb} - 273.15)} \right) \left(\frac{0.62509\, p_{v_{wb}}}{p_{abs} - 1.005\, p_{v_{wb}}} \right) - \left(\frac{1.00416(T - T_{wb)}}{2501.6 + 1.8577(T - 273.15) - 4.184(T_{wb} - 273.15)} \right), \quad [\text{kg/kg}_{\text{dry air}}] \tag{A.16}$$

Enthalpy:

$$i_{av} = \frac{c_{p_a}(T - 273.15) + w(i_{fgwo} + c_{p_v}(T - 273.15))}{1 + w}, \; [\text{J/kg}_{\text{air-vapour}}] \tag{A.17}$$

or the enthalpy of the air-vapor mixture per unit mass of dry air

$$i_{ma} = c_{p_a}(T - 273.15) + w(i_{fgwo} + c_{p_v}(T - 273.15), \; [\text{J/kg}_{\text{dry air}}] \tag{A.18}$$

where the specific heats are evaluated at $\frac{T+273.15}{2}$ and the latent heat i_{fgwo}, is evaluated at 273.15 K according to equation (A.23).

The thermophysical properties of saturated water liquid from 273.15K to 380K.

Density:

$$\rho_w = \frac{1}{1.49343 \cdot 10^{-3} - 3.7164 \cdot 10^{-6} \cdot T + 7.09782 \cdot 10^{-9} \cdot T^2 - 1.90321 \cdot 10^{-20} \cdot T^6}, \quad \text{(A.19)}$$

[kg/m^3]

Specific heat:

$$c_{p_w} = 8.15599 \cdot 10^3 - 28.0627 \cdot T + 5.11283 \cdot 10^{-2} \cdot T^2 - 2.17582 \cdot 10^{-13} \cdot T^6, \quad \text{(A.20)}$$

[J/kgK]

Dynamic viscosity:

$$\mu_w = 2.414 \cdot 10^{-5} \cdot 10^{\frac{247.8}{T-140}}, \text{ [kg/ms]} \quad \text{(A.21)}$$

Thermal conductivity:

$$k_w = -6.14255 \cdot 10^{-1} + 6.9962 \cdot 10^{-3} \cdot T - 1.01075 \cdot 10^{-5} \cdot T^2 + 4.74737 \cdot 10^{-12} \cdot T^4, \quad \text{(A.22)}$$

[W/mK]

Latent heat of vaporization:

$$i_{fgw} = 3.4831814 \cdot 10^{-6} - 5.8627703 \cdot 10^3 \cdot T + 12.139568 \cdot T^2 - 1.40290431 \cdot 10^{-2} \cdot T^3, \text{ [J/kg]} \quad \text{(A.23)}$$

Critical pressure:

$$p_{wc} = 22.09 \cdot 10^6, \text{ [N/m}^2\text{]} \quad \text{(A.24)}$$

Surface tension:

$$\sigma_w = 5.148103 \cdot 10^{-2} + 3.998714 \cdot 10^{-4} \cdot T - 1.4721869 \cdot 10^{-6} \cdot T^2 + 1.21405335 \cdot 10^{-9} \cdot T^3, \quad \text{[N/m]} \tag{A.25}$$

Appendix B – Sample calculations

Appendix B gives sample calculations of the mathematical models derived in chapter4 and 5.

Droplet lifetime in free stream air (chapter 4)

Consider the following input data for the calculation of the droplet evaporation rate and lifetime for a droplet traveling in free stream air, as described in chapter 4.

Free stream velocity, $u_\infty = 3\,\frac{\mathbf{m}}{\mathbf{s}}$

Free stream temperature, $T_\infty = 302\,\mathbf{K}$

Droplet surface temperature ($\approx$ wetbulb temperature), $T_s = 291\,\mathbf{K}$

Humidity ratio, $\omega = 8\cdot 10^{-3}\,\frac{\mathbf{kg\,H_2O}}{\mathbf{kg\ dry\ air}}$

Droplet density, $\rho_l = 998.7\,\frac{\mathbf{kg}}{\mathbf{m}^3}$

Air density, $\rho_{av} = 1.16\,\frac{\mathbf{kg}}{\mathbf{m}^3}$

Thermal conductivity of droplet, $k = 0.0262\,\frac{\mathbf{W}}{\mathbf{m}\cdot\mathbf{K}}$

Enthalpy of vaporization, $h_{fg} = 2.257\cdot 10^6\,\frac{\mathbf{J}}{\mathbf{kg}}$

Air specific heat (average), $c_p = 1008\,\frac{\mathbf{J}}{\mathbf{kg}\cdot\mathbf{K}}$

Dynamic viscosity of air, $\mu_a = 1.87\cdot 10^{-5}\,\frac{\mathbf{kg}}{\mathbf{m}\cdot\mathbf{s}}$

Initial droplet radius, $r = 22.5\cdot 10^{-6}\ \mathbf{m}$

Prandtl number, $\mathrm{Pr} = 0.705$

Droplet lifetime

It is assumed that the droplet reaches a situation of steady state relatively early in its lifetime. Therefore either B_M or B_T (defined in equation (4.13)) can be used for the calculations.

Calculating B_T yields the following

$$\begin{aligned} B_T &= \frac{c_{pa}\left(T_\infty - T_s\right)}{h_{fg}} \\ &= \frac{1008\left(302 - 291\right)}{2.257 \cdot 10^6} \\ &= 0.004913 \end{aligned}$$

The total lifetime of the droplet can be determined by determining the change in droplet mass in increments. For this calculation an increment of 0.05 s was chosen.

Making use of equation (4.23), the relative velocity of the droplet in the moving air stream for the first increment can be determined

$$\begin{aligned} u_R &= 5.05 \cdot 10^9 \cdot {d_d}^3 + 2.86 \cdot 10^7 \cdot {d_d}^2 + 16.48 \cdot d_d \\ &= 5.05 \cdot 10^9 \cdot \left(2 \cdot 22.5 \cdot 10^{-6}\right)^3 + 2.86 \cdot 10^7 \cdot \left(2 \cdot 22.5 \cdot 10^{-6}\right)^2 + 16.48 \cdot \left(2 \cdot 22.5 \cdot 10^{-6}\right) \\ &= 0.06 \ \frac{\mathbf{m}}{\mathbf{s}} \end{aligned}$$

The Reynolds number of the droplet can then be determined

$$\begin{aligned} \mathrm{Re} &= \frac{\rho_a \cdot u_R \cdot d_d}{\mu_a} \\ &= \frac{1.16 \cdot 0.06 \cdot 2\left(22.5 \cdot 10^{-6}\right)}{1.87 \cdot 10^{-5}} \\ &= 0.17 \end{aligned}$$

The rate of evaporation of the droplet can now be determined using equation (4.28)

$$\dot{m}_d = 2\pi \cdot d_d \left(\frac{k}{c_p}\right)_a \ln(1+B_T)\left(1+0.3\cdot \mathrm{Re}_d^{\,0.5}\,\mathrm{Pr}_a^{\,0.33}\right)$$

$$= 2\pi \cdot \left(2\cdot 22.5\cdot 10^{-6}\right)\left(\frac{0{,}0262}{1008}\right)_a \ln(1+0.004913)\left(1+0.3\cdot(0.17)^{0.5}\cdot 1\right)$$

$$= 4.04\cdot 10^{-11}\,\frac{\mathbf{kg}}{\mathbf{s}}$$

The change in droplet mass for this increment can now be calculated

$$\Delta m_d = \dot{m}_d \cdot t$$

$$= 4.04\cdot 10^{-11}\cdot 0.05$$

$$= 2.02\cdot 10^{-12}\ \mathbf{kg}$$

Subtracting this mass from the initial mass of the droplet gives the mass of the droplet at the second increment. The initial mass of the droplet can be calculated as

$$m_{d,1} = \frac{4}{3}\pi r_d^{\,3}\cdot \rho_l$$

$$= \frac{4}{3}\pi\left(22.5\cdot 10^{-6}\right)^3 \cdot 998.7$$

$$= 4.77\cdot 10^{-11}\ \mathbf{kg}$$

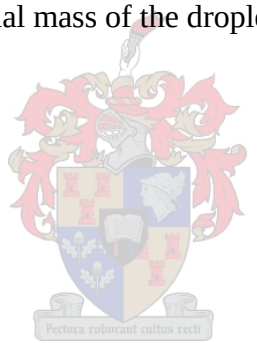

The droplet mass at the second interval is thus

$$m_{d,2} = m_{d,1} - \Delta m$$

$$= 4.77\cdot 10^{-11} - 2.02\cdot 10^{-12}$$

$$= 4.563\cdot 10^{-11}\ \mathbf{kg}$$

The droplet radius at this point can be determined as follows

$$r_{d,2} = \left(\frac{3m_{d,2}}{4\rho_l \pi} \right)^{1/3}$$
$$= \left(\frac{3\left(4.563 \cdot 10^{-11}\right)}{4(998.7)\pi} \right)^{1/3}$$
$$= 22.17 \cdot 10^{-6} \ \mathbf{m}$$

At this point the droplet evaporation rate for the next increment can be determined, and the calculation can be continued until the droplet has been completely evaporated, or until the droplet has entered a boundary layer, at which point the model derived in chapter 5 can be used to determine the droplet behavior.

Droplet lifetime in a laminar boundary layer (chapter 5)

Consider the following input data for the calculation of the droplet trajectory and heat transfer coefficient enhancement for a droplet traveling in a laminar boundary layer on a flat plate, as described in chapter 5.

Flow direction free stream velocity, $u_\infty = 1{,}524\,\dfrac{\mathbf{m}}{\mathbf{s}}$

Transverse velocity, $v_t = 0.0152\,\dfrac{\mathbf{m}}{\mathbf{s}}$

Free stream temperature, $T_\infty = 308\,\mathbf{K}$

Flat surface temperature, $T_0 = 323\,\mathbf{K}$

Average boundary layer temperature, $T_{av} = \dfrac{T_0 + T_\infty}{2}$

$= 315.5\,\mathbf{K}$

Droplet surface temperature ($\approx$ wetbulb temperature), $T_s = 291\,\mathbf{K}$

Mass flux of droplets in the free stream, $\dot{m}'' = 0.01492\,\dfrac{\mathbf{kg}}{\mathbf{m}^2\mathbf{s}}$

Atmospheric pressure, $p_{atm} = 101325\,\mathbf{Pa}$

Flat surface width, $b = 0.3048\,\mathbf{m}$

Flat surface length, $l = 0.15\,\mathbf{m}$

Spacing between two flat surfaces, $s = 0.001\,\mathbf{m}$

Point of entry of droplet in boundary layer, $\xi = 0.0005\,\mathbf{m}$

Molecular weight of droplet, $M = 18\,\dfrac{\mathbf{kg}}{\mathbf{kg\ mole}}$

Average molecular weight of the boundary layer, $\overline{M} = 28\,\dfrac{\mathbf{kg}}{\mathbf{kg\ mole}}$

Droplet density, $\rho_l = 1001\,\dfrac{\mathbf{kg}}{\mathbf{m}^3}$

Average boundary layer density, $\rho_{av} = 1.25\,\dfrac{\mathbf{kg}}{\mathbf{m}^3}$

Dynamic viscosity of droplet, $\mu_l = 1.95 \cdot 10^{-5}\ \dfrac{\mathbf{kg}}{\mathbf{m \cdot s}}$

Kinematic viscosity of droplet, $\nu_l = 2.04 \cdot 10^{-5}\ \dfrac{\mathbf{m}^2}{\mathbf{s}}$

Binary vapor diffusivity, $D = 2.29 \cdot 10^{-5}\ \dfrac{\mathbf{m}^2}{\mathbf{s}}$

Thermal conductivity of droplet, $k = 0.034\ \dfrac{\mathbf{W}}{\mathbf{m \cdot K}}$

Enthalpy of vaporization, $h_{fg} = 2.4 \cdot 10^{6}\ \dfrac{\mathbf{J}}{\mathbf{kg}}$

Average Sherwood number, $Sh_{av} = 2.59$

Initial droplet radius, $r = 22.5 \cdot 10^{-6}\ \mathbf{m}$

Droplet trajectory

The vapor pressure at the droplet surface temperature and the average boundary layer temperature can be determined with equation (A.5)

At the droplet surface temperature:

$$p_{v,T_s} = 10^{z}$$

$$z = 10.79586\left(1 - \frac{273.16}{T_s}\right) + 5.02808\log_{10}\left(\frac{273.16}{T_s}\right) + 1.50474 \cdot 10^{-4}\left[1 - 10^{-8.29692\left(\frac{T_s}{273.16} - 1\right)}\right] + 4.2873 \cdot 10^{-4}\left[10^{4.76955\left(1 - \frac{273.16}{T_s}\right)} - 1\right] + 2.786118312$$

$$= 10.79586\left(1 - \frac{273.16}{291}\right) + 5.02808\log_{10}\left(\frac{273.16}{291}\right) + 1.50474 \cdot 10^{-4}\left[1 - 10^{-8.29692\left(\frac{291}{273.16} - 1\right)}\right] + 4.2873 \cdot 10^{-4}\left[10^{4.76955\left(1 - \frac{273.16}{291}\right)} - 1\right] + 2.78611831$$

$$= 3.31$$

$$p_{v,T_s} = 10^{3.31}$$
$$= 2.041 \cdot 10^3 \,\mathbf{Pa}$$
$$= 2.041 \,\mathbf{kPa}$$

At the average boundary layer temperature:

$$p_{v,T_{av}} = 10^z$$

$$z = 10.79586\left(1 - \frac{273.16}{T_{av}}\right) + 5.02808\log_{10}\left(\frac{273.16}{T_{av}}\right)$$
$$+ 1.50474 \cdot 10^{-4}\left[1 - 10^{-8.29692\left(\frac{T_{av}}{273.16} - 1\right)}\right] + 4.2873 \cdot 10^{-4}\left[10^{4.76955\left(1 - \frac{273.16}{T_{av}}\right)} - 1\right] + 2.786118312$$
$$= 10.79586\left(1 - \frac{273.16}{315.5}\right) + 5.02808\log_{10}\left(\frac{273.16}{315.5}\right)$$
$$+ 1.50474 \cdot 10^{-4}\left[1 - 10^{-8.29692\left(\frac{315.5}{273.16} - 1\right)}\right] + 4.2873 \cdot 10^{-4}\left[10^{4.76955\left(1 - \frac{273.16}{315.5}\right)} - 1\right] + 2.78611831$$
$$= 3.92$$

$$p_{v,T_{av}} = 10^{3.92}$$
$$= 8.316 \cdot 10^3 \,\mathbf{Pa}$$
$$= 8.316 \,\mathbf{kPa}$$

The mole fraction at the droplet surface temperature and the average boundary layer temperature can be determined in the following manner:

At the droplet surface temperature:

$$Y_0 = Y\left(p_{v,T_s}\right)$$
$$= \frac{p_{v,T_s}}{p_{atm}}$$
$$= \frac{2041}{101325}$$
$$= 0.02$$

At the average boundary layer temperature:

$$
\begin{aligned}
Y_{av} &= Y\left(p_{v,T_{av}}\right) \\
&= \frac{p_{v,T_{av}}}{p_{atm}} \\
&= \frac{8316}{101325} \\
&= 0.082
\end{aligned}
$$

The parameter λ, defined by equation (5.5), can be determined as follows:

$$
\begin{aligned}
\lambda &= \frac{1}{2}\cdot\left[\left(\frac{M}{\overline{M}}\right)\cdot\left(\frac{\rho_{av}}{\rho_l}\right)\cdot D\cdot Sh_{av}\cdot\ln\left(\frac{1-Y_{av}}{1-Y_0}\right)\right] \\
&= \frac{1}{2}\cdot\left[\left(\frac{18}{25}\right)\cdot\left(\frac{1.25}{1001}\right)\cdot\left(2.29\cdot10^{-5}\right)\cdot\left(2.59\right)\cdot\ln\left(\frac{1-0.082}{1-0.02}\right)\right] \\
&= -1.554\cdot10^{-9}\ \frac{\mathbf{m}^2}{\mathbf{s}}
\end{aligned}
$$

The parameters α and β are calculated with equations (5.9) and (5.10) respectively

$$
\begin{aligned}
\alpha &= \left(3\lambda + \frac{9\mu}{2\rho_l}\right) \\
&= \left(3\left(-1.554\cdot10^{-9}\right) + \frac{9\left(1.95\cdot10^{-5}\right)}{2\left(1001\right)}\right) \\
&= 8.3\cdot10^{-8}\ \frac{\mathbf{m}^2}{\mathbf{s}}
\end{aligned}
$$

$$
\begin{aligned}
\beta &= \left(1-\frac{\rho_{av}}{\rho_l}\right)\cdot g \\
&= \left(1-\frac{1.25}{1001}\right)\cdot 9.81 \\
&= 9.794\ \frac{\mathbf{m}}{\mathbf{s}^2}\cdot
\end{aligned}
$$

The coefficients *A* and *B* can be calculated with equations (5.13) and (5.14) respectively

$$A = \left[\frac{\beta r_0^{\,2}}{\alpha + 2\lambda} - v_t \right] \frac{r_0^{\,\alpha/\lambda}}{(\alpha - 2\lambda)}$$

$$= \left[\frac{9.794\left(22.5\cdot 10^{-6}\right)^2}{8.3\cdot 10^{-8} + 2\left(-1.554\cdot 10^{-9}\right)} - 0.0152 \right] \frac{\left(22.5\cdot 10^{-6}\right)^{\left(8.3\cdot 10^{-8}\right)/\left(-1.554\cdot 10^{-9}\right)}}{\left[8.3\cdot 10^{-8} - 2\left(-1.554\cdot 10^{-9}\right)\right]}$$

$$= 9.144\cdot 10^{253}$$

$$B = -r_0^{\,2}\left[\frac{\beta r_0^{\,2}}{\left(\alpha^2 + 4\lambda^2\right)} - \frac{v_t}{(\alpha - 2\lambda)} + \frac{\beta r_0^{\,2}}{4\lambda(\alpha + 2\lambda)} \right]$$

$$= -\left(22.5\cdot 10^{-6}\right)^2 \left[\frac{9.794\left(22.5\cdot 10^{-6}\right)^2}{\left(\left(8.3\cdot 10^{-8}\right)^2 + 4\left(-1.554\cdot 10^{-9}\right)^2\right)} - \frac{0.0152}{8.3\cdot 10^{-8} - 2\left(-1.554\cdot 10^{-9}\right)} + \frac{9.794\left(22.5\cdot 10^{-6}\right)^2}{4\left(-1.554\cdot 10^{-9}\right)\left[8.3\cdot 10^{-8} + 2\left(-1.554\cdot 10^{-9}\right)\right]} \right]$$

$$= 4.78\cdot 10^{-3}$$

The coefficient *C* can be calculated with equation (5.16)

$$C = r_0^{\,2}\left(\frac{\left(\beta r_0^{\,2} - 4\lambda v_t\right)}{4\lambda(\alpha - 2\lambda)} \right)$$

$$= 22.5\cdot 10^{-6}\left[\frac{\left(9.794\cdot\left(22.5\cdot 10^{-6}\right) - 4\left(-1.554\cdot 10^{-9}\right)(0.0152)\right)}{4\left(-1.554\cdot 10^{-9}\right)\left(8.3\cdot 10^{-8} - 2\left(-1.554\cdot 10^{-9}\right)\right)} \right]$$

$$= -4.779\cdot 10^{-3}$$

Euler's method can now be used to integrate equation (5.19)

The first iteration was performed in the following manner:

At $i = 1$

Increment, $\Delta x = 0.0001\,\mathbf{m}$

Initial droplet radius, $r_1 = r_0$

Time, $t_1 = 0\ \mathbf{s}$

Droplet entry point, $x_1 = \xi = 0.0005\,\mathbf{m}$

The boundary layer thickness at $i = 1$ can be calculated with equation (5.18)

$$\delta_1 = 5\left(\frac{\nu x_1}{u_\infty}\right)^{1/2}$$
$$= 5\left(\frac{\left(2.04\cdot10^{-5}\right)\left(0.0005\right)}{1.524}\right)^{1/2}$$
$$= 4.091\cdot10^{-4}\,\mathbf{m}$$

The time differential over the first interval, *dt*, can now be determined

$$dt = \frac{5\nu^{1/2}x_1^{1/2}}{u_\infty^{3/2}\left[5\left(\frac{\nu}{u_\infty}\right)^{1/2}x_1^{1/2} - A\left(r_0^{\,2}+2\lambda t\right)^{\left(1-\frac{\alpha}{2\lambda}\right)} + C - \frac{\beta\left(r_0^{\,2}+2\lambda t\right)^2}{4\lambda(\alpha+2\lambda)}\right]}\cdot dx$$
$$= \frac{5\left(2.04\cdot10^{-5}\right)^{1/2}\left(0.0005\right)^{1/2}}{\left(1.524\right)^{3/2}\left[\begin{array}{l}5\left(\frac{2.04\cdot10^{-5}}{1.524}\right)^{1/2}\left(0.0005\right)^{1/2} \\ -\left(9.144\cdot10^{253}\right)\left(\left(22.5\cdot10^{-6}\right)^2+2\left(-1.554\cdot10^{-9}\right)t_i\right)^{\left(1-\frac{\left(8.3\cdot10^{-8}\right)}{2\left(-1.554\cdot10^{-9}\right)}\right)} \\ +\left(-4.779\cdot10^{-3}\right)-\frac{9.794\left(\left(22.5\cdot10^{-6}\right)^2+2\left(-1.554\cdot10^{-9}\right)t_i\right)^2}{4\left(-1.554\cdot10^{-9}\right)\left(8.3\cdot10^{-8}-2\left(-1.554\cdot10^{-9}\right)\right)}\end{array}\right]}$$
$$= 6.562\cdot10^{-5}\,\mathbf{s}$$

The time at the second increment is therefore

$$t_2 = t_1 + dt$$
$$= 0 + 6.562\cdot10^{-5}$$
$$= 6.562\cdot10^{-5}\,\mathbf{s}$$

The decrease in droplet radius as a result of evaporation can be determined with equation (5.7)

$$r_2 = \sqrt{r_0^{\,2} + 2\lambda t_2}$$
$$= \sqrt{22.5\cdot10^{-6} + 2\left(-1.554\cdot10^{-9}\right)6.562\cdot10^{-5}}$$
$$= 2.24954\cdot10^{-5}\,\mathbf{m}$$

The penetration of the droplet into the boundary layer can be determined with equation (5.12)

$$p_1 = A(r_0^{\,2} + 2\lambda t)^{(1-\alpha/2\lambda)} + B + \frac{\beta(r_0^{\,2} + 2\lambda t)^2}{4\lambda(\alpha + 2\lambda)}$$
$$= 9.144\cdot10^{253}\left(\left(22.5\cdot10^{-6}\right)^2 + 2\left(-1.554\cdot10^{-9}\right)t_i\right)^{\left(1-\left(8.3\cdot10^{-8}\right)/2\left(-1.554\cdot10^{-9}\right)\right)} + 4.78\cdot10^{-3}$$
$$+ \frac{9.794\left(\left(22.5\cdot10^{-6}\right)^2 + 2\left(-1.554\cdot10^{-9}\right)t_i\right)^2}{4\left(-1.554\cdot10^{-9}\right)\left(8.3\cdot10^{-8} + 2\left(-1.554\cdot10^{-9}\right)\right)}$$
$$= 1.022\cdot10^{-6}\,\mathbf{m}$$

The *y*-coordinate of the droplet at this stage can be determined by subtracting the penetration from the boundary layer thickness

$$y_1 = \delta_1 + p_1$$
$$= 4.091\cdot10^{-4} - 1.022\cdot10^{-6}$$
$$= 4.08\cdot10^{-4}\,\mathbf{m}$$

The iterations continue until the droplet has completely evaporated, i.e. $r = 0$, or the droplet has impacted the surface, i.e. $y = 0$.

.

For this calculation, $r = 0$ at $i = 860$

From the calculations shown above, both the *x*- and *y*-coordinate of the droplet can be determined as it travels in the boundary layer, and the trajectory can be plotted.

Heat transfer coefficient

The following additional input data is required to determine the enhancement of heat transfer coefficient:

Prandtl number, $\Pr = 0.705$

The Reynolds number can be determined with the following equation

$$\begin{aligned}\mathrm{Re} &= \frac{l \cdot u_\infty}{\nu} \\ &= \frac{0.15 \cdot 1.524}{2.04 \cdot 10^{-5}} \\ &= 1.121 \cdot 10^4\end{aligned}$$

With knowledge of the Prandtl and Reynolds numbers, the Nusselt number can be determined using the Polhausen relation (Kays, 1966) given by equation (5.32)

$$\begin{aligned}Nu &= 0.664\,\mathrm{Re}^{1/2}\,\mathrm{Pr}^{1/3} \\ &= 0.664\left(1.121 \cdot 10^4\right)^{1/2}(0.705)^{1/3} \\ &= 62.559\end{aligned}$$

The heat transfer coefficient in the absence of droplets, $\bar{h}$, can now be determined

$$\begin{aligned}\bar{h} &= \frac{Nu \cdot k}{l} \\ &= \frac{(62.559)(0.034)}{0.15} \\ &= 14.18\,\frac{\mathbf{W}}{\mathbf{m}^2\mathbf{K}}\end{aligned}$$

The resistances R_1 and R_2 can be determined using equations (5.20) and (5.21) respectively, and making use of the boundary layer thickness, α, the penetration, p, and the flow direction length, x, at the point where the droplet has completely evaporated (i.e. at $i = 860$)

$$R_1 = \frac{1}{\bar{h} b x_{860}} \left(\frac{\delta_{860} - \rho_{860}}{\delta_{860}} \right)$$
$$= \frac{1}{(14.18)(0.3048)(0.0863)} \left(\frac{0.00536 - 0.00475}{0.00536} \right)$$
$$= 0.298 \frac{\mathbf{K}}{\mathbf{W}}$$

$$R_2 = \frac{1}{\bar{h} b x_{860}} \left(\frac{\rho_{860}}{\delta_{860}} \right)$$
$$= \frac{1}{(14.18)(0.3048)(0.0863)} \left(\frac{0.00475}{0.00536} \right)$$
$$= 2.38 \frac{\mathbf{K}}{\mathbf{W}}$$

The coefficient *K* can be determined using equation (5.25). In this case, the droplet has been completely vaporized, therefore equation (5.25) simplifies to

$$K = \frac{6}{\dot{m}'' s b h_{fg}}$$
$$= \frac{6}{(0.01492)(0.001)(0.03048)(2.4 \cdot 10^6)}$$
$$= 0.55$$

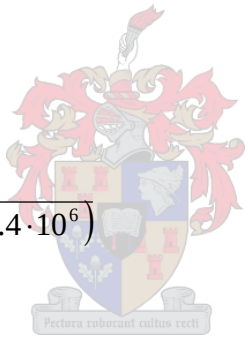

The interface temperature can be determined with equation (5.27)

$$T_i = \frac{K(R_1 T_\infty + R_2 T_0) - R_1 R_2}{K(R_1 + R_2)}$$
$$= \frac{0.55(0.298(308) + 2.38(323)) - 0.298(2.38)}{0.55(0.298 + 2.38)}$$
$$= 320.852 \mathbf{K}$$

The resistance R_3 can now be determined with equation (5.24)

$$R_3 = K(T_i - T_\infty)$$
$$= 0.55(320.85 - 308)$$
$$= 7.065 \frac{\mathbf{K}}{\mathbf{W}}$$

Making use of the three resistances calculated above, the equivalent resistance, R_{eq} can be determined with equation (5.28)

$$R_{eq} = \frac{R_1R_2 + R_2R_3 + R_1R_3}{R_2 + R_3}$$
$$= \frac{(0.298)(2.38) + (2.38)(7.065) + (0.298)(7.065)}{(2.38) + (7.065)}$$
$$= 2.078 \frac{\mathbf{K}}{\mathbf{W}}$$

The heat flux, $\dot{q}''$, from the surface can now be determined with equation (5.30)

$$\dot{q}'' = \frac{(T_0 - T_\infty)}{R_{eq} b x_{860}}$$
$$= \frac{(323 - 308)}{2.078(0.3048)(0.863)}$$
$$= 274.099 \frac{\mathbf{W}}{\mathbf{m}^2}$$

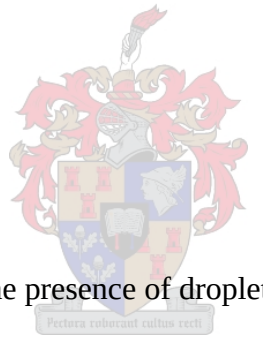

The heat transfer coefficient in the presence of droplets is given by equation (5.31)

$$h = \frac{274.099}{(323 - 308)}$$
$$= 18.273 \frac{\mathbf{W}}{\mathbf{m}^2\mathbf{K}}$$

By comparing the heat transfer coefficient in the presence of droplets to the heat transfer coefficient in the absence of droplets, the enhancement in heat transfer coefficient can be found

$$Enhancement = \frac{h - \bar{h}}{\bar{h}} \cdot 100$$
$$= 28.87\ \%$$

Appendix C – Experimental data

Appendix C gives the experimental data of all the experiments performed.

Nozzle charging performance experimental data

Tables C.1 to C.6 give the tabulated data for the nozzle charging performance experiment. The tables also contain the sample variance, s^2, and a boxplot showing the sample mean, y, the first quartile, Q_1, and third quartile, Q_3, upper inner fence, *UIF*, and lower inner fence, *LIF*, and possible outliers, as indicated in figure C.1. The boxplots following each table represents the plate and the cone data respectively. Data falling inside the inner fences (*LIF* and *UIF*) is considered to be "good" data, while data falling outside these fences (i.e. outliers) is considered "questionable" data.

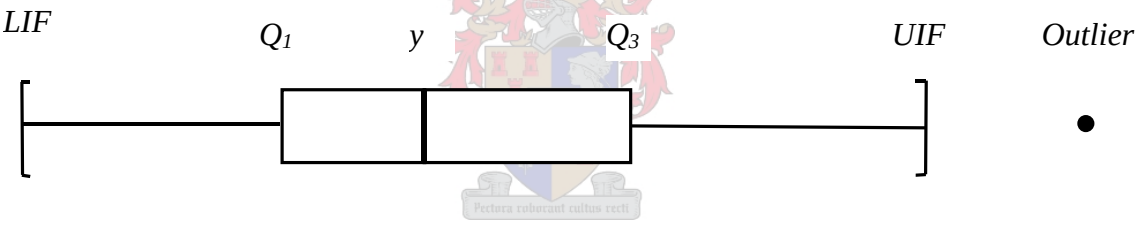

Figure C.1 Description of boxplot

Table C.1 Summary of experimental data of Nozzle Charging Performance Test 1

Water pressure [bar]	8							
Induction ring voltage [kV]	2							
		Reading						
		1	2	3	4	5	Average	s^2
Voltage drop over resistor (Plate) [V]		0.05	0.08	0.02	0.08	0.081	**0.0622**	0.000729
Voltage drop over resistor (Cone) [V]		0.3	0.8	0.29	0.6	0.6	**0.518**	0.04812

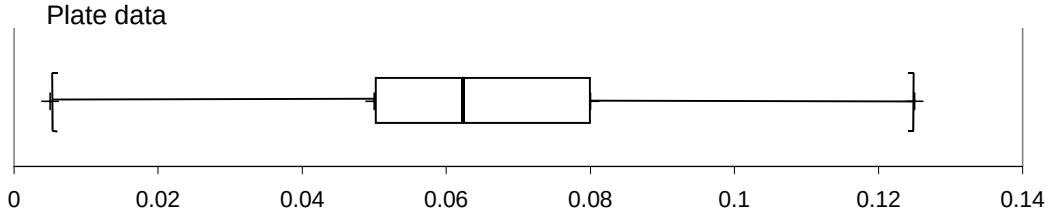

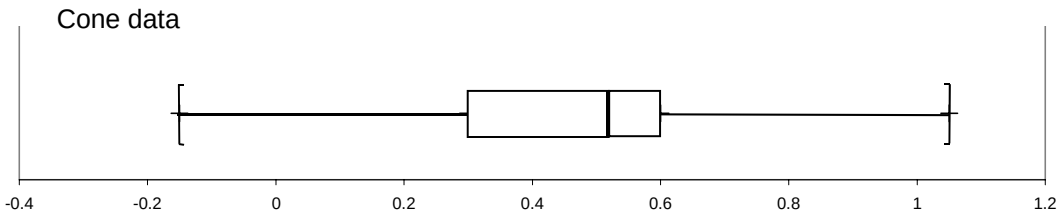

Table C.2 Summary of experimental data of Nozzle Charging Performance Test 2

Water pressure [bar]	8							
Induction ring voltage [kV]	3							
		Reading						
		1	2	3	4	5	Average	s^2
Voltage drop over resistor (Plate) [V]		0.1	0.14	0.08	0.05	0.2	**0.114**	0.00338
Voltage drop over resistor (Cone) [V]		0.4	1.2	0.85	1	0.85	**0.86**	0.08675

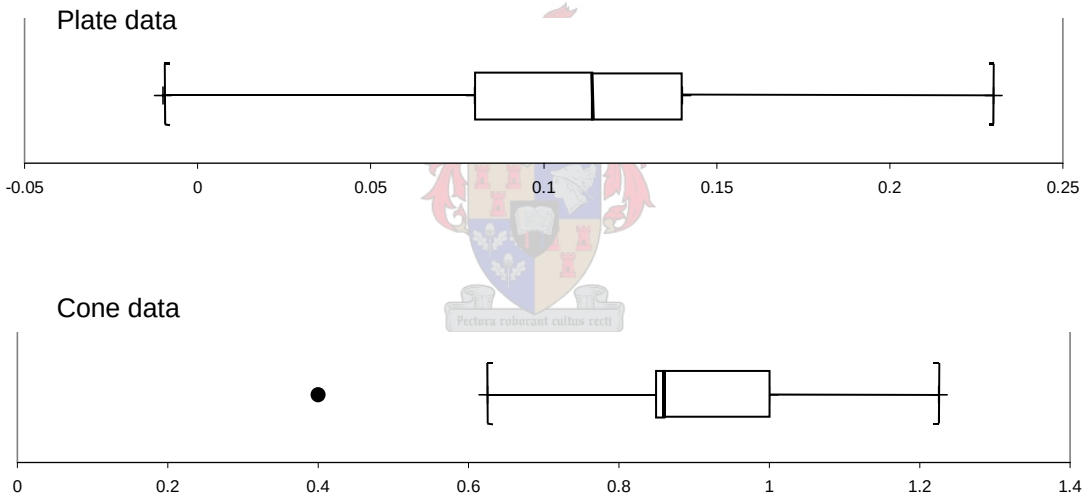

Table C.3 Summary of experimental data of Nozzle Charging Performance Test 3

Water pressure [bar]	8							
Induction ring voltage [kV]	4							
		Reading						
		1	2	3	4	5	Average	s^2
Voltage drop over resistor (Plate) [V]		0.76	0.85	0.75	0.75	0.4	**0.702**	0.03027
Voltage drop over resistor (Cone) [V]		0.9	1	1.2	1.2	1.7	**1.2**	0.095

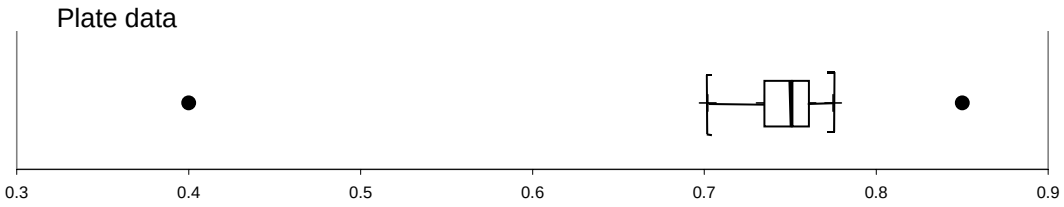

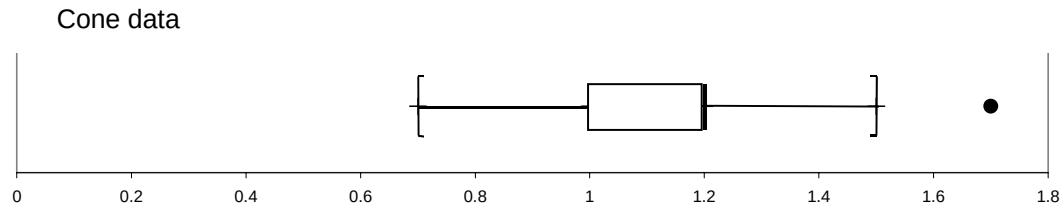

Table C.4 Summary of experimental data of Nozzle Charging Performance Test 4

Water pressure [bar]	8						
Induction ring voltage [kV]	5						
		Reading					
		1	2	3	4	5	Average	s^2
Voltage drop over resistor (Plate) [V]		0.92	0.45	0.2	0.35	0.2	**0.424**	0.08813
Voltage drop over resistor (Cone) [V]		1.4	1.25	1.25	2.6	2.2	**1.74**	0.38675

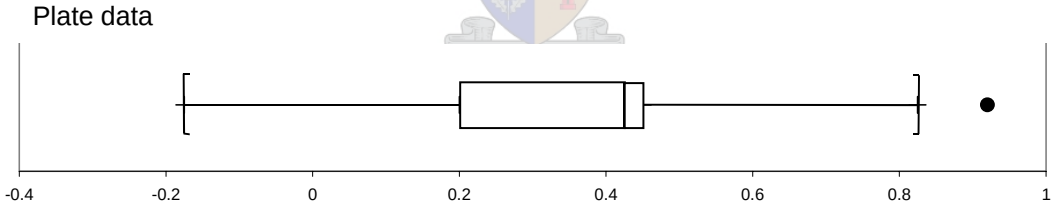

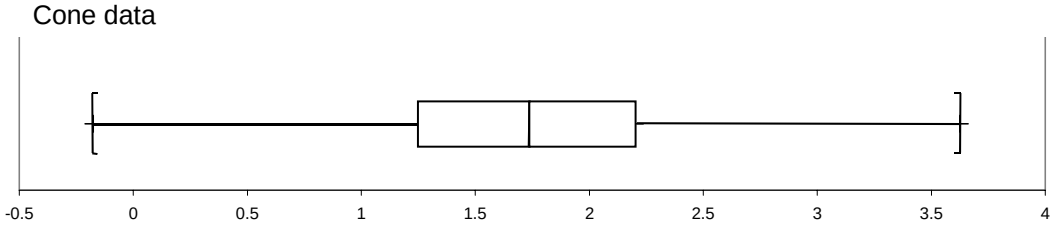

Table C.5 Summary of experimental data of Nozzle Charging Performance Test 5

Water pressure [bar]	8							
Induction ring voltage [kV]	6							
		Reading						
		1	2	3	4	5	Average	s^2
Voltage drop over resistor (Plate) [V]		0.76	0.61	0.45	0.54	0.4	**0.552**	0.02007
Voltage drop over resistor (Cone) [V]		2.53	1.97	2.87	2.75	2.81	**2.586**	0.13508

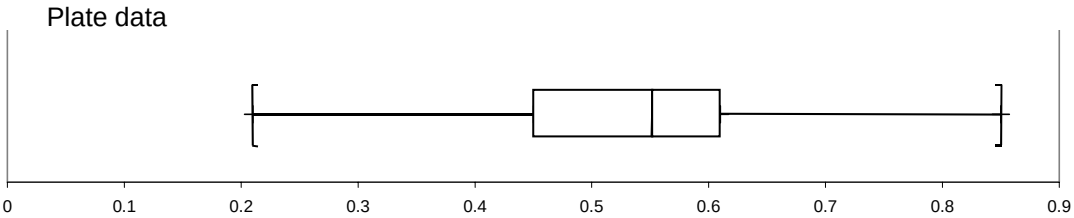

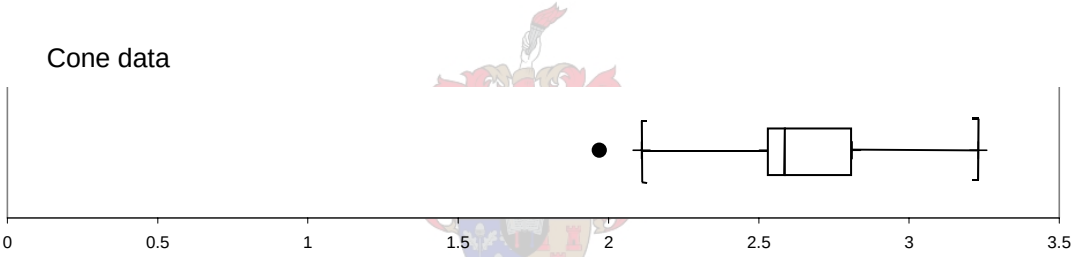

Table C.6 Summary of experimental data of Nozzle Charging Performance Test 6

Water pressure [bar]	8							
Induction ring voltage [kV]	7							
		Reading						
		1	2	3	4	5	Average	s^2
Voltage drop over resistor (Plate) [V]		0.53	0.63	0.76	0.65	0.5	**0.614**	0.01073
Voltage drop over resistor (Cone) [V]		2.98	2.9	2.11	2.9	3.2	**2.818**	0.17172

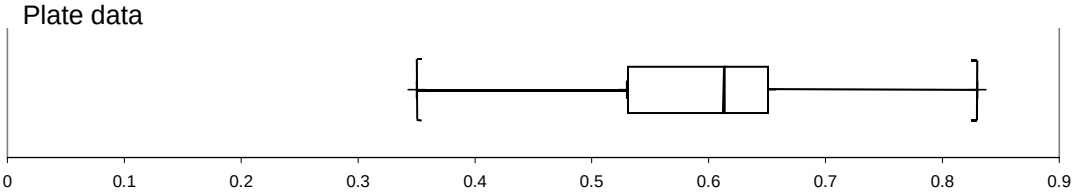

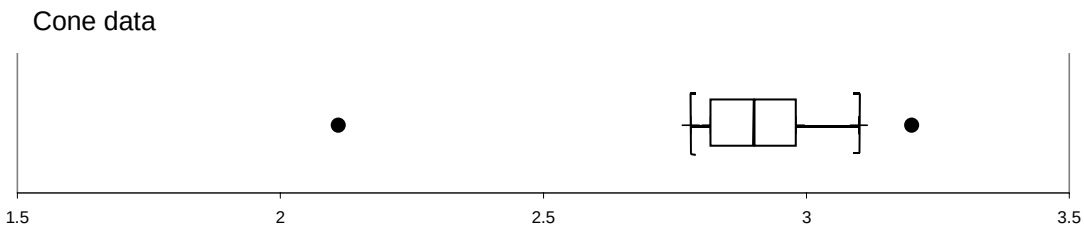

Applied electrostatic spray experimental data

Tables C.7 to C.11 give the tabulated data for the applied electrostatic spray experiment. Each test consisted of 3 runs. The average of the three runs as well as the sample variance, s^2, is given. A boxplot of the data for ΔHR obtained from the three runs is also given.

Table C.7 Summary of experimental data of Applied Electrostatic Spray Test 1

Run 1						
Dry conditions						
T_{db1} [°C]	16.9	T_{wb1} [°C]	15.7			
T_{db2} [°C]	16.5	T_{wb2} [°C]	15.9	Humidity ratio		
Average	16.7		15.8	(eqn. A.16)	**Psat@T**	**Rel Hum**
	289.85		288.95	0.010970498	1899.931	0.918161
Wet conditions						
T_{db1} [°C]	39.1	T_{wb1} [°C]	39			
T_{db2} [°C]	39.2	T_{wb2} [°C]	38.9	Humidity ratio		
Average	39.15		38.95	(eqn. A.16)	**Psat@T**	**Rel Hum**
	312.3		312.1	0.046463861	7049.312	0.9924403
				ΔHR		
Atmospheric pressure [Pa]			100650	**0.035493363**		

Run 2						
Dry conditions						
T_{db1} [°C]	16.8	T_{wb1} [°C]	15.2			
T_{db2} [°C]	17.2	T_{wb2} [°C]	15.3	Humidity ratio		
Average	17		15.25	(eqn. A.16)	**Psat@T**	**Rel Hum**
	290.15		288.4	0.010218418	1936.458	0.840083
Wet conditions						
T_{db1} [°C]	38.1	T_{wb1} [°C]	38			
T_{db2} [°C]	38.1	T_{wb2} [°C]	37.9	Humidity ratio		
Average	38.1		37.95	(eqn. A.16)	**Psat@T**	**Rel Hum**
	311.25		311.1	0.043870532	6661.787	0.9954196
				ΔHR		
Atmospheric pressure [Pa]			100650	**0.033652114**		

Run 3						
Dry conditions						
T_{db1} [^{o}C]	17.6	T_{wb1} [^{o}C]	16.1			
T_{db2} [^{o}C]	16.9	T_{wb2} [^{o}C]	16.1	Humidity ratio		
Average	17.25		16.1	(eqn. A.16)	**Psat@T**	**Rel Hum**
	290.4		289.25	0.01109009	1967.366	0.8961859
Wet conditions						
T_{db1} [^{o}C]	39.4	T_{wb1} [^{o}C]	39.1			
T_{db2} [^{o}C]	39.5	T_{wb2} [^{o}C]	39.1	Humidity ratio		
Average	39.45		39.1	(eqn. A.16)	**Psat@T**	**Rel Hum**
	312.6		312.25	0.046800782	7163.549	0.9832
				ΔHR		
Atmospheric pressure [Pa]			100650	**0.035710692**		

Average of runs	**s^2**
0.034952057	**1.2792E-06**

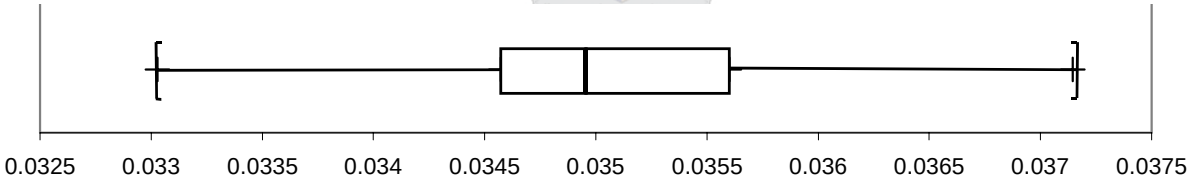

Table C.8 Summary of experimental data of Applied Electrostatic Spray Test 2

Run 1						
Dry conditions						
T_{db1} [^{o}C]	17.7	T_{wb1} [^{o}C]	16.3			
T_{db2} [^{o}C]	17.4	T_{wb2} [^{o}C]	16.4	Humidity ratio		
Average	17.55		16.35	(eqn. A.16)	**Psat@T**	**Rel Hum**
	290.7		289.5	0.0112585	2005.026	0.8924691
Wet conditions						
T_{db1} [^{o}C]	35.1	T_{wb1} [^{o}C]	34.5			
T_{db2} [^{o}C]	35.3	T_{wb2} [^{o}C]	34.5	Humidity ratio		
Average	35.2		34.5	(eqn. A.16)	**Psat@T**	**Rel Hum**
	308.35		307.65	0.035621356	5685.630	0.958892
				ΔHR		
Atmospheric pressure [Pa]			100650	**0.024362856**		

Run 2						
Dry conditions						
T_{db1} [^{o}C]	17.8	T_{wb1} [^{o}C]	15.9			
T_{db2} [^{o}C]	17.9	T_{wb2} [^{o}C]	16.3	Humidity ratio		
Average	17.85		16.1	(eqn. A.16)	**Psat@T**	**Rel Hum**
	291		289.25	0.010840897	2043.317	0.8438178
Wet conditions						
T_{db1} [^{o}C]	35.6	T_{wb1} [^{o}C]	34.9			
T_{db2} [^{o}C]	35.7	T_{wb2} [^{o}C]	34.6	Humidity ratio		
Average	35.65		34.75	(eqn. A.16)	**Psat@T**	**Rel Hum**
	308.8		307.9	0.036063575	5828.447	0.9463719
				ΔHR		
Atmospheric pressure [Pa]			100650	**0.025222678**		

Run 3						
Dry conditions						
T_{db1} [^{o}C]	17.5	T_{wb1} [^{o}C]	16.2			
T_{db2} [^{o}C]	16.9	T_{wb2} [^{o}C]	16	Humidity ratio		
Average	17.2		16.1	(eqn. A.16)	**Psat@T**	**Rel Hum**
	290.35		289.25	0.011110866	1961.150	0.9006811
Wet conditions						
T_{db1} [^{o}C]	34.9	T_{wb1} [^{o}C]	33.2			
T_{db2} [^{o}C]	35	T_{wb2} [^{o}C]	33.1	Humidity ratio		
Average	34.95		33.15	(eqn. A.16)	**Psat@T**	**Rel Hum**
	308.1		306.3	0.032394877	5607.605	0.8885314
				ΔHR		
Atmospheric pressure [Pa]			100650	**0.021284011**		

Average of runs	**s^2**
0.023623182	**4.2886E-06**

Table C.9 Summary of experimental data of Applied Electrostatic Spray Test 3

Run 1						
Dry conditions						
T_{db1} [^oC]	16.8	T_{wb1} [^oC]	15.9			
T_{db2} [^oC]	16.3	T_{wb2} [^oC]	16	Humidity ratio		
Average	16.55		15.95	(eqn. A.16)	**Psat@T**	**Rel Hum**
	289.7		289.1	0.011172935	1881.895	0.9464831
Wet conditions						
T_{db1} [^oC]	28.9	T_{wb1} [^oC]	28.8			
T_{db2} [^oC]	29.1	T_{wb2} [^oC]	28.9	Humidity ratio		
Average	29		28.85	(eqn. A.16)	**Psat@T**	**Rel Hum**
	302.15		302	0.02553494	4005.060	0.9938617
				ΔHR		
Atmospheric pressure [Pa]			100940	**0.014362006**		

Run 2						
Dry conditions						
T_{db1} [^oC]	16.8	T_{wb1} [^oC]	15.9			
T_{db2} [^oC]	16.9	T_{wb2} [^oC]	16.2	Humidity ratio		
Average	16.85		16.05	(eqn. A.16)	**Psat@T**	**Rel Hum**
	290		289.2	0.011164311	1918.118	0.9279048
Wet conditions						
T_{db1} [^oC]	29	T_{wb1} [^oC]	28.9			
T_{db2} [^oC]	29.3	T_{wb2} [^oC]	29	Humidity ratio		
Average	29.15		28.95	(eqn. A.16)	**Psat@T**	**Rel Hum**
	302.3		302.1	0.025668059	4039.935	0.9902149
				ΔHR		
Atmospheric pressure [Pa]			100940	**0.014503749**		

Run 3						
Dry conditions						
T_{db1} [^{o}C]	17	T_{wb1} [^{o}C]	16.2			
T_{db2} [^{o}C]	16.9	T_{wb2} [^{o}C]	16	Humidity ratio		
Average	16.95		16.1	(eqn. A.16)	**Psat@T**	**Rel Hum**
	290.1		289.25	0.01118094	1930.328	0.9233849
Wet conditions						
T_{db1} [^{o}C]	29.5	T_{wb1} [^{o}C]	29			
T_{db2} [^{o}C]	29.6	T_{wb2} [^{o}C]	28.7	Humidity ratio		
Average	29.55		28.85	(eqn. A.16)	**Psat@T**	**Rel Hum**
	302.7		302	0.02529749	4134.230	0.954206
				ΔHR		
Atmospheric pressure [Pa]			100940	**0.01411655**		

Average of runs	**s^2**
0.014327435	**3.8377E-08**

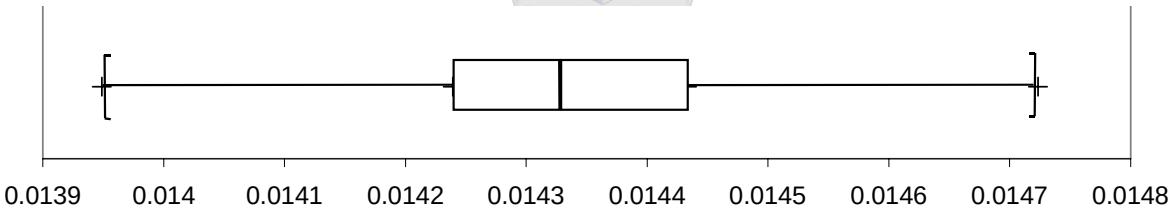

Table C.10 Summary of experimental data of Applied Electrostatic Spray Test 4

Run 1						
Dry conditions						
T_{db1} [^oC]	17	T_{wb1} [^oC]	16.4			
T_{db2} [^oC]	17.5	T_{wb2} [^oC]	16.6	Humidity ratio		
Average	17.25		16.5	(eqn. A.16)	**Psat@T**	**Rel Hum**
	290.4		289.65	0.011525805	1967.366	0.933437
Wet conditions						
T_{db1} [^oC]	27.1	T_{wb1} [^oC]	26.5			
T_{db2} [^oC]	27	T_{wb2} [^oC]	26.3	Humidity ratio		
Average	27.05		26.4	(eqn. A.16)	**Psat@T**	**Rel Hum**
	300.2		299.55	0.021785491	3574.949	0.9554757
				ΔHR		
Atmospheric pressure [Pa]			100940	**0.010259686**		

Run 2						
Dry conditions						
T_{db1} [^oC]	17.2	T_{wb1} [^oC]	16.7			
T_{db2} [^oC]	17.3	T_{wb2} [^oC]	16.2	Humidity ratio		
Average	17.25		16.45	(eqn. A.16)	**Psat@T**	**Rel Hum**
	290.4		289.6	0.011466702	1967.366	0.9287371
Wet conditions						
T_{db1} [^oC]	27.3	T_{wb1} [^oC]	26.5			
T_{db2} [^oC]	27.4	T_{wb2} [^oC]	26.5	Humidity ratio		
Average	27.35		26.5	(eqn. A.16)	**Psat@T**	**Rel Hum**
	300.5		299.65	0.021834928	3638.378	0.9408767
				ΔHR		
Atmospheric pressure [Pa]			100940	**0.010368226**		

Run 3						
Dry conditions						
T_{db1} [^{o}C]	17.7	T_{wb1} [^{o}C]	16.2			
T_{db2} [^{o}C]	17.9	T_{wb2} [^{o}C]	16.8	Humidity ratio		
Average	17.8		16.5	(eqn. A.16)	**Psat@T**	**Rel Hum**
	290.95		289.65	0.011297034	2036.891	0.8840004
Wet conditions						
T_{db1} [^{o}C]	27.8	T_{wb1} [^{o}C]	26.7			
T_{db2} [^{o}C]	27.9	T_{wb2} [^{o}C]	26.7	Humidity ratio		
Average	27.85		26.7	(eqn. A.16)	**Psat@T**	**Rel Hum**
	301		299.85	0.021978766	3746.273	0.919593
				ΔHR		
Atmospheric pressure [Pa]			100940	**0.010681732**		

Average of runs	**s^2**
0.010436548	**4.8032E-08**

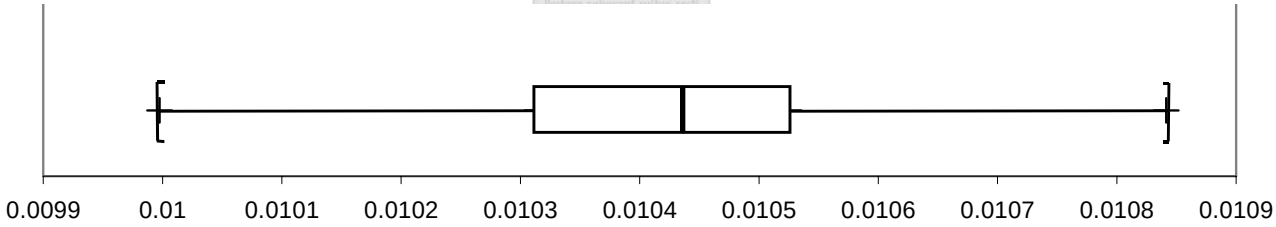

Table C.11 Summary of experimental data of Applied Electrostatic Spray Test 5

Run 1						
Dry conditions						
T_{db1} [^oC]	18.8	T_{wb1} [^oC]	17.7			
T_{db2} [^oC]	19.4	T_{wb2} [^oC]	17.3	Humidity ratio		
Average	19.1		17.5	(eqn. A.16)	**Psat@T**	**Rel Hum**
	292.25		290.65	0.011998435	2209.847	0.8619619
Wet conditions						
T_{db1} [^oC]	24.7	T_{wb1} [^oC]	23.8			
T_{db2} [^oC]	24.9	T_{wb2} [^oC]	23.1	Humidity ratio		
Average	24.8		23.45	(eqn. A.16)	**Psat@T**	**Rel Hum**
	297.95		296.6	0.017880822	3129.159	0.8988237
				ΔHR		
Atmospheric pressure [Pa]			100650	**0.005882387**		

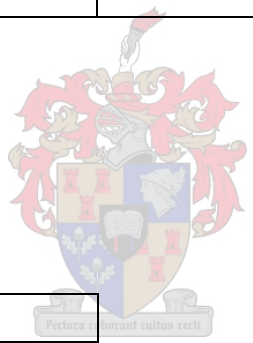

Run 2						
Dry conditions						
T_{db1} [^oC]	18.9	T_{wb1} [^oC]	17.9			
T_{db2} [^oC]	19	T_{wb2} [^oC]	17.6	Humidity ratio		
Average	18.95		17.75	(eqn. A.16)	**Psat@T**	**Rel Hum**
	292.1		290.9	0.01233265	2189.255	0.8964091
Wet conditions						
T_{db1} [^oC]	24.8	T_{wb1} [^oC]	23.7			
T_{db2} [^oC]	24.8	T_{wb2} [^oC]	23.9	Humidity ratio		
Average	24.8		23.8	(eqn. A.16)	**Psat@T**	**Rel Hum**
	297.95		296.95	0.018377976	3129.159	0.9257569
				ΔHR		
Atmospheric pressure [Pa]			100940	**0.006045326**		

Run 3						
Dry conditions						
T_{db1} [^{o}C]	19.3	T_{wb1} [^{o}C]	17.6			
T_{db2} [^{o}C]	19.2	T_{wb2} [^{o}C]	18	Humidity ratio		
Average	19.25		17.8	(eqn. A.16)	**Psat@T**	**Rel Hum**
	292.4		290.95	0.012269668	2230.608	0.8753848
Wet conditions						
T_{db1} [^{o}C]	25	T_{wb1} [^{o}C]	23.5			
T_{db2} [^{o}C]	25.1	T_{wb2} [^{o}C]	24	Humidity ratio		
Average	25.05		23.75	(eqn. A.16)	**Psat@T**	**Rel Hum**
	298.2		296.9	0.018192666	3176.168	0.90312
				ΔHR		
Atmospheric pressure [Pa]			100940	**0.005922998**		

Average of runs	**s^2**
0.005950237	**7.1937E-09**

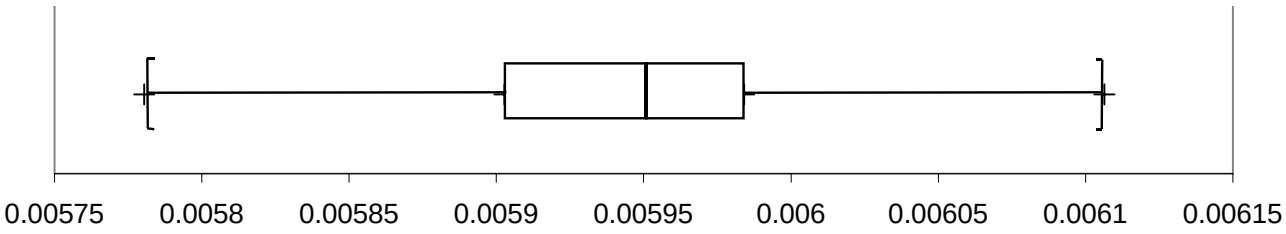

Appendix D – Detail design drawings

Appendix D contains the design drawings for the two types of nozzles manufactured as well as the design drawings of the heat exchanger.

Design drawings

This section includes the detail design drawings for the large and small nozzle frames used in the experiments performed, as well as the design drawings of the steam pipe used in the electrostatic spray application experiment.

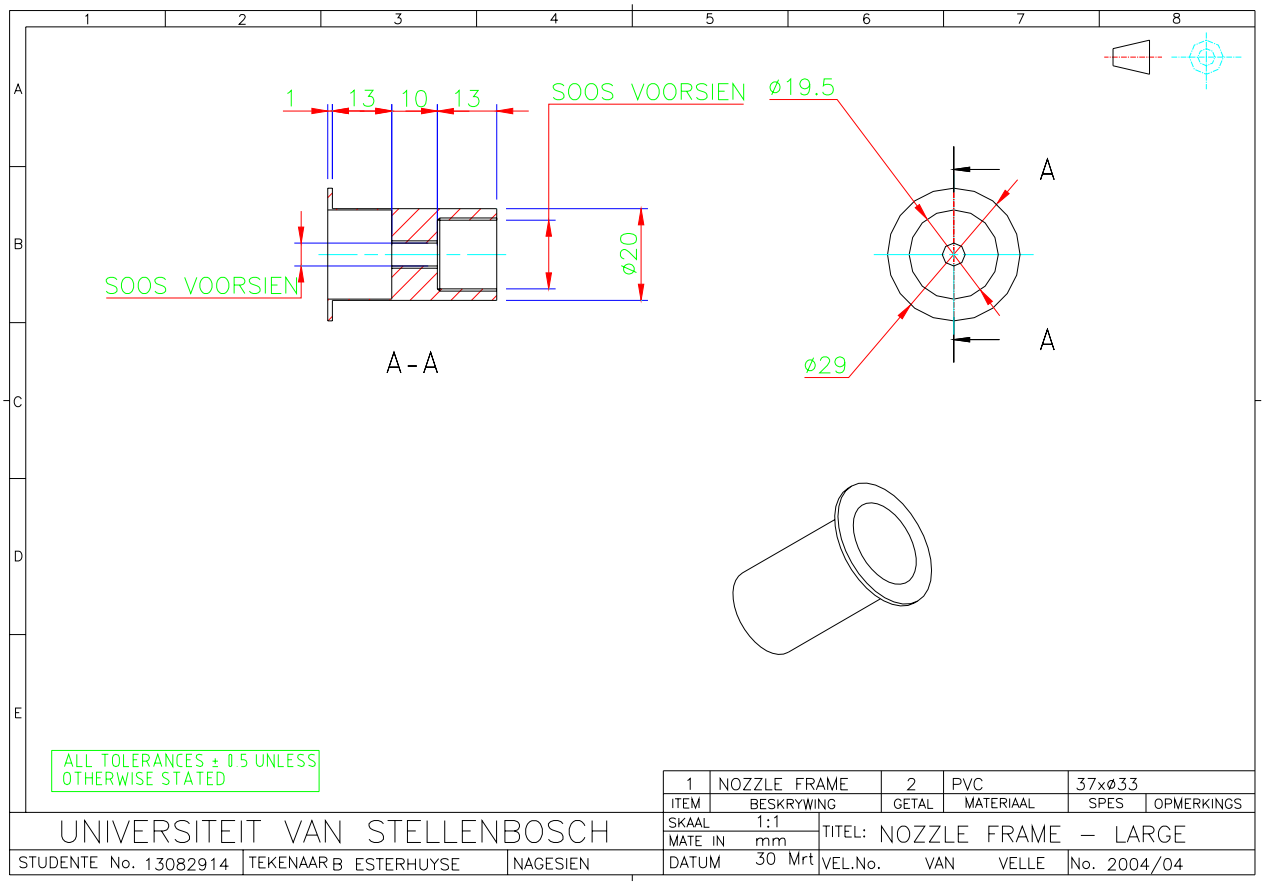

Figure D.1 Design drawing of large nozzle frame

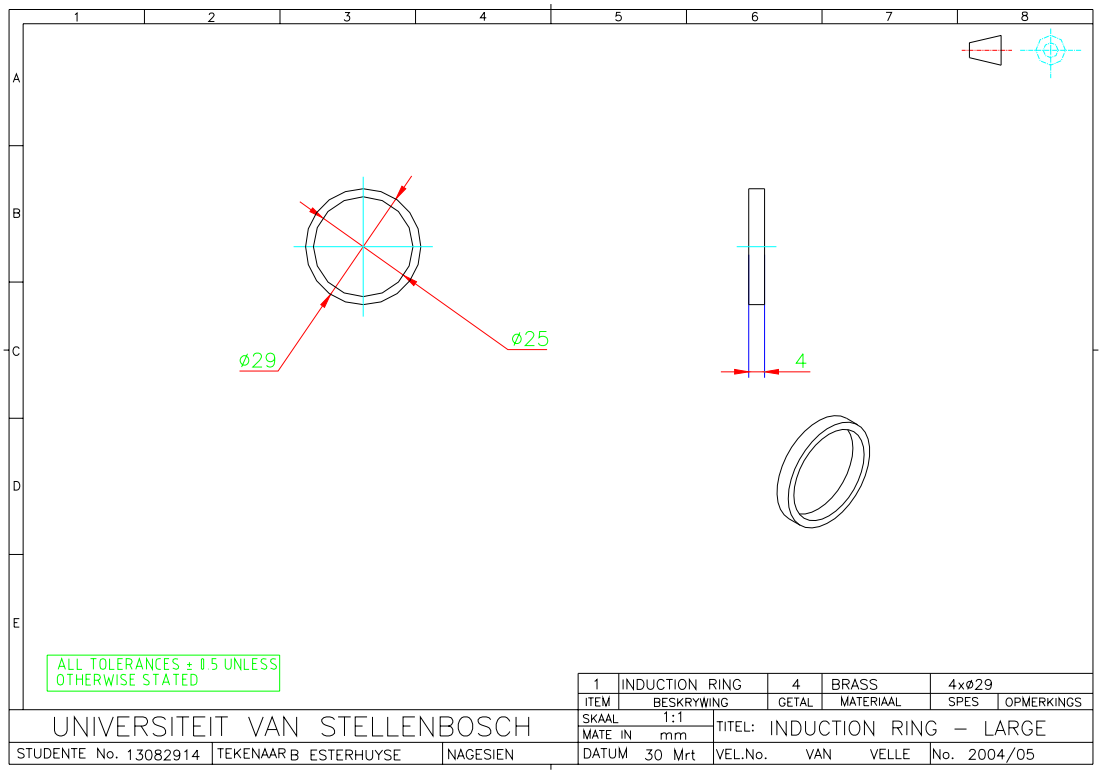

Figure D.2 Design drawing of large induction ring

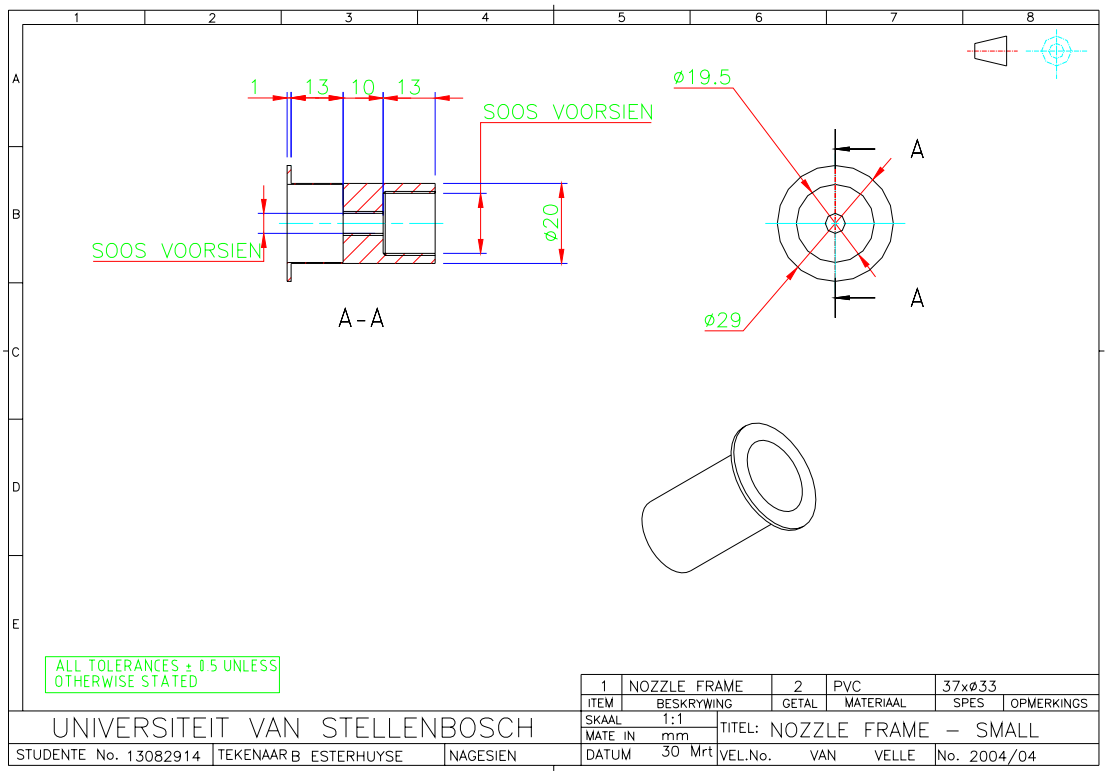

Figure D.3 Design drawing of small nozzle frame

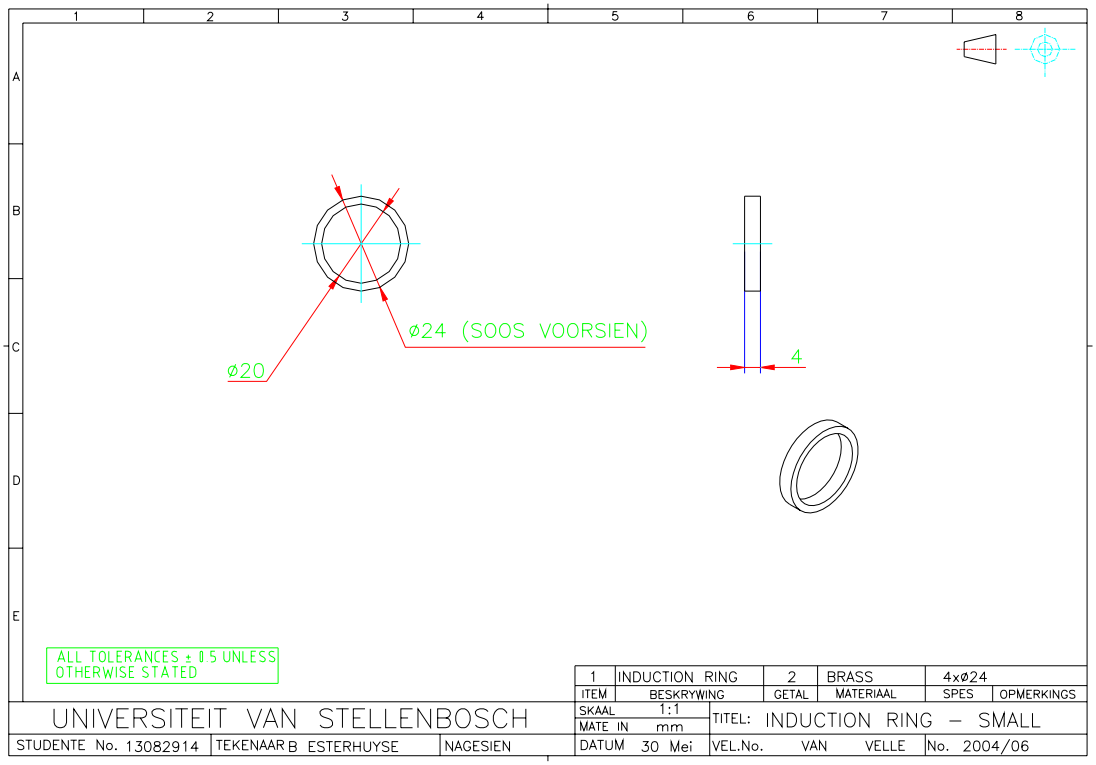

Figure D.4 Design drawing of small induction ring

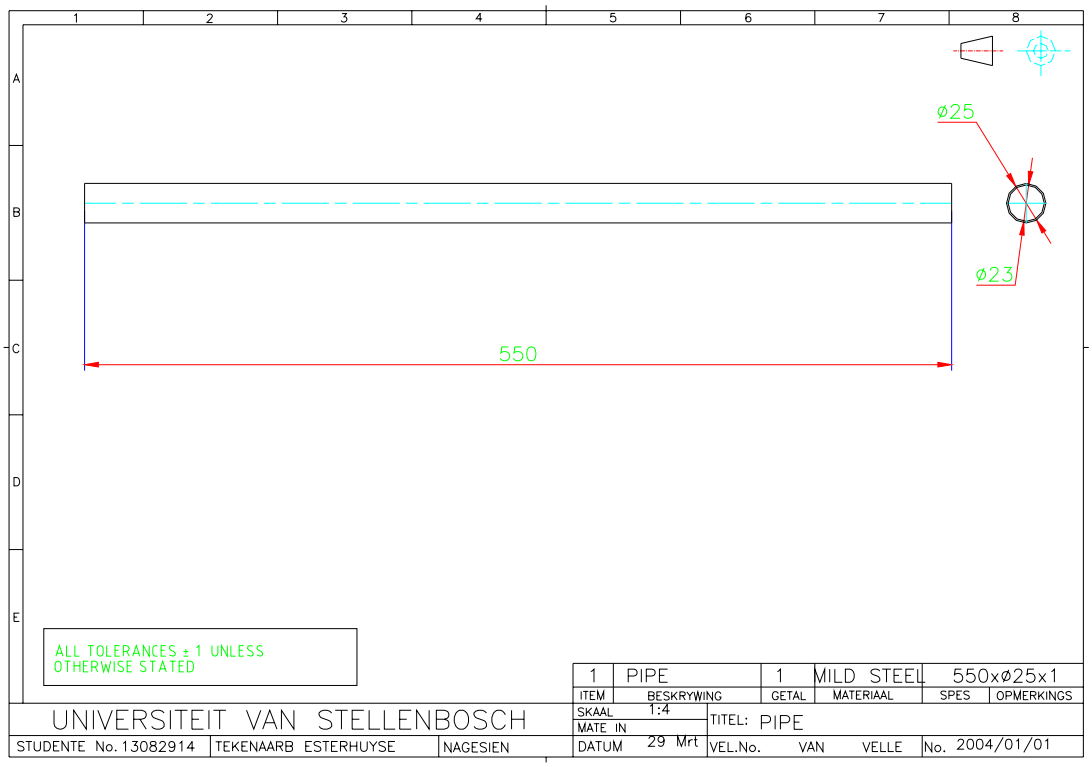

Figure D.5 Design drawing of steam pipe

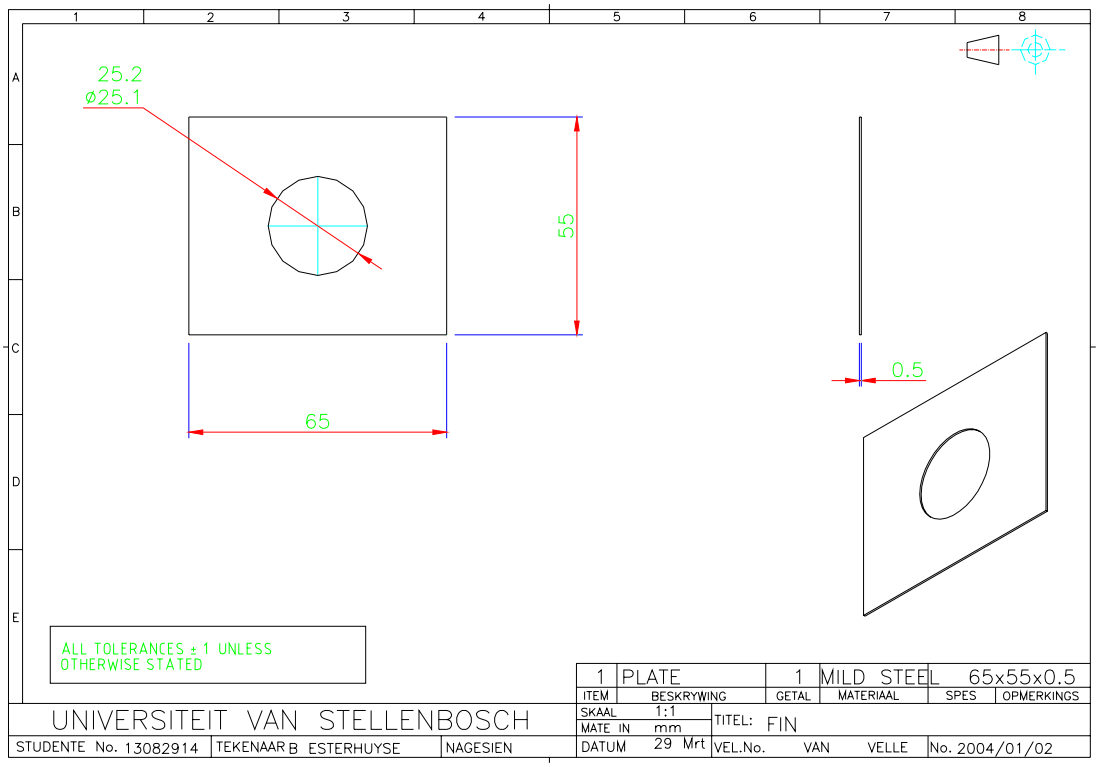

Figure D.6 Design drawing of fin

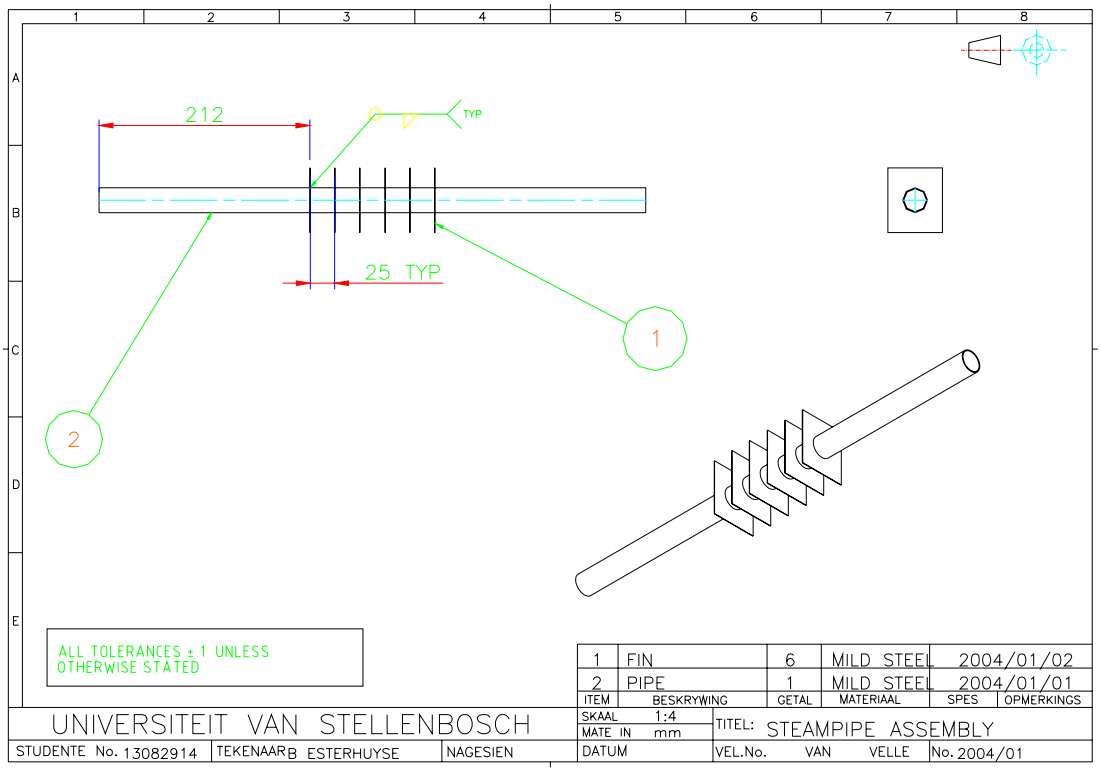

Figure D.7 Design drawing of steam pipe assembly